Modeling, Control and Experimental Testing of a Supercapacitor/Battery Hybrid System - Passive and Semi-Active Topologies

Lars Hagvaag Seim

Norwegian University of Life Sciences
Department of Mathematical Sciences and Technology
Master Thesis 30 credits 2011

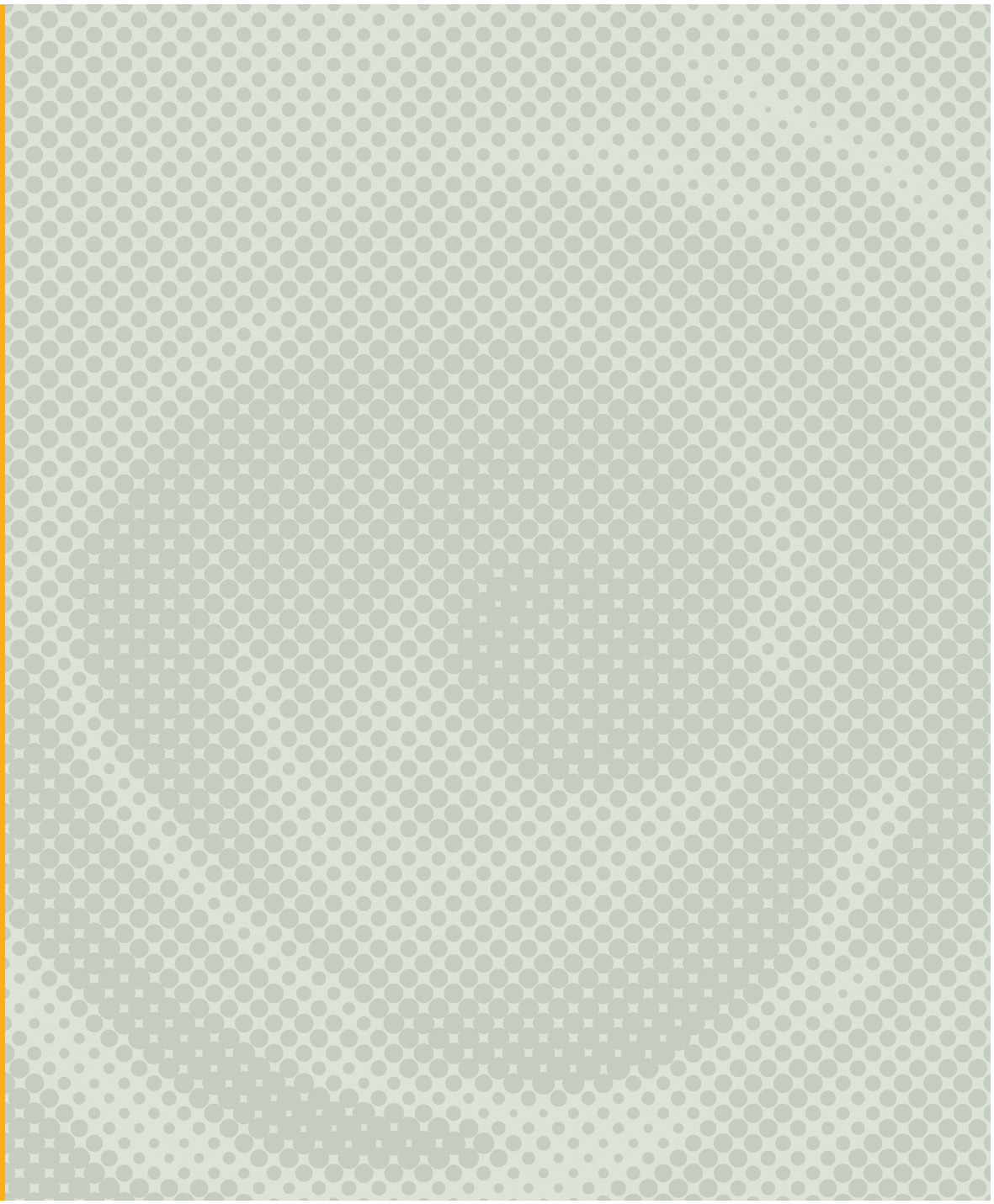

This page intentionally left blank

Abstract

Supercapacitors possess unique properties that can complement other energy storage technologies in hybrid electric energy systems. Due to its performance characteristics - such as fast charge and discharge capability, high power density and high recycleability - a supercapacitor can relieve the battery of narrow and repeated transient charging and discharging, ensuring longer battery life, enabling higher system peak power performance and improve system efficiency. An equivalent supercapacitor model is formalized based on electric characterization of two different supercapacitor modules(165 F and 130 F) manufactured by Maxwell Technologies. A passive hybrid topology of a lead acid battery/supercapacitor configuration is analyzed, modeled and simulated using Matlab/Simulink, and then tested in the REHYS-laboratory at the Norwegian Institute of Energy Technology under a transient load regime using a pulse train load at different frequencies and duty cycles. We find that the passive hybridization causes a significantly reduced battery current and voltage ripple, enhanced peak power performance and potentially increased system efficiency and system run time, though, it is essential to minimize the parasitic resistances and inductances for optimal system performance. Greatest benefits are seen when the load pulse rate is higher than the system eigen-frequency and at smaller duty cycles. A semi-active topology applying a half-bridge, current controlled DC/DC-converter between supercapacitor and battery/load-side, is also analyzed, modeled and simulated using Matlab/Simulink. Converter control design and control strategies is formulated using linear control theory and an average dynamic converter model. A moving average power smoothing control strategy is implemented, and simulations confirm that the supercapacitor operation range is expanded and that the peak power performance is further enhanced compared with the passive hybrid topology.

Sammendrag

Superkondensatorer har unike egenskaper som kan komplementere andre energilagringsteknologier i hybride, elektriske energisystemer. Grunnet superkondensatorens høye effekttetthet, hurtige responstid og robusthet ved mange lade/utladningssykluser, så kan den avlaste batteriet ved transiente lastprofiler, noe som kan forlenge batteriets levetid, forbedre ytelsen ved topplaster og øke systemets effektivitet. På bakgrunn av elektrisk karakterisering formuleres en ekvivalent superkondensatormodel av to ulike superkondensatormoduler(165F og 130F) produsert av Maxwell Technologies.

En passiv hybridtopologi bestående av blybatteri og superkondensator er analysert, modelert og simulert ved bruk av Matlab/Simulink. I REHYS-laboratoriet ved Institiutt for energiteknikk testes topologien under et transient lastregime ved å benytte en pulstoglast med forskjellige frekvenser og pulsbredder. Vi finner at den passive hybridiseringen gir en signifikant redusert spennings- og strømripple for batteriet, forbedrer systemets topplastytelse og at den potensielt kan øke systemets effektivitet og kjøretid. Det er imidlertid essensielt å minimere systemets parasittiske impedands for optimal ytelse. Størst forbedring observeres når pulsraten er høyere enn systemets egenfrekvens og ved smalere pulsbredder. En semi-aktiv topologi blir analysert, modelert og simulert ved bruk av en halvbro DC/DC-konverter med strømkontroll mellom superkondensator og batteri/last. Kontrolldesign og kontrollstrategier formuleres på basis av lineær kontrollteori og en midlet dynamisk konvertermodell. En kontrollstrategi basert på glidende gjennomsnitt benyttes for effektutjevning, og simuleringer bekrefter at operasjonsområdet til superkondensatoren utvides og at topplastytelsen forbedres sammenlignet med den passive hybride topologien.

Acknowledgments

I would like to thank my supervisors Preben J. S. Vie and Øystein Ulleberg at the Norwegian Institute of Energy Technology(IFE) for excellent support and guidance during my work with the thesis. A special thank to PhD-student Samson Gebre Tesfahunegn(IFE/NTNU) for sharing his knowledge and his patient and educational approach when explaining challenging concepts. I have learned a lot. I am very grateful for the advise and help from my supervisor at the University of Life Sciences, Petter H. Heyerdahl.

Finally, I would like to thank friends and family for their care and support during this last semester.

Kjeller, 22^{nd} of December, 2011

Lars Hagvaag Seim

List of Acronyms and Abbreviations

AC Alternating Current

BAS Battery-Alone System

CST Control System Toolbox

DC Direct Current

dB Decibel

DoD Depth of Discharge [%]

EC Electrochemical Capacitor

EDLC Electrochemical Double-Layer Capacitor

EIS Electrochemical Impedance Spectroscopy

ESR Equivalent Series Resistance

GUI Graphic User Interface

IFE Institute of Energy Technology

MOSFET Metaloxidesemiconductor Field-Effect Transistor

MPP Max Power Point

PEMFC Proton Exchange Membrane Fuel Cell

PHS Passive Hybrid System

PMW Pulse Width Modulation

PV Photovotalic

REHYS Renewable Energy/Hydrogen System

SAHS Semi-Active Hybrid System

SoC State of Charge

List of Symbols

A Area [m^2]

C Capacitance [F]

C_{diff} Differential Capacitance [F]

C_1 First Order Supercapacitor Capacitance [F]

Capacity [Ah]

C(s) Output Signal in Laplace Domain

D Duty cycle/Duty Ratio [-]

E Electric field strength [N/C]

$\mathbf{e}(\infty)$ Steady State Error in Time Domain [-]

E(s) Error in Laplace Domain [-]

$\mathbf{f_{eigen}}, \beta$ Eigen-frequency [Hz]

$\mathbf{f_c}$ Cross-over Frequency [Hz]

$\mathbf{f_s}$ Switching Frequency [Hz]

$\mathbf{G_p}$ Plant Transfer Functionss

$\mathbf{G_c}$ Controller Transfer Function

$\mathbf{G_{OL}}$ Open Loop Transfer Function

H(s) Transducer Transfer Function

I Current [A]

$\mathbf{I_{batt}}, \mathbf{I_b}$ Battery Current [A]

$\mathbf{I_{ch}}$ Charging Current [A]

$\mathbf{I_{in}}$ Converter Input Current [A]

$\mathbf{I_L}, \mathbf{i_L}$ Converter Inductor Current [A]

$\mathbf{I_{LB}}$ Converter Inductor Boundary Current [A]

$\mathbf{I_o}$ Converter Ouput Current [A]

$\mathbf{I_{ref}}, \mathbf{i_{ref}}$ Converter Reference Current [A]

$\mathbf{I_{sc}}, \mathbf{I_c}$ Supercapacitor Current [A]

$\mathbf{I_0}, \mathbf{I_{load}}$ Load Current [A]

L Inductance [H]

$\mathbf{K_i}$ Integral Gain

$\mathbf{K_p}$ Proportional Gain

$\mathbf{M}$ Voltage Control Parameter [-]

$\mathbf{m}$ Diffusion Parameter

$\mathbf{P}$ Power [W]

$\mathbf{P_{in}}$ Converter Input Power [W]

$\mathbf{P_m}$ Moving Averaged Power [W]

$\mathbf{P_o}$ Converter Output Power [W]

$\mathbf{Q}$ Charge [C]

$\mathbf{R_{leak}}$ Leakage Resistance [Ω]

$\mathbf{R_c}$ Internal Resistance Supercapacitor [Ω]

$\mathbf{R_1}$ First Order Supercapacitor Resistance [Ω]

$\mathbf{R_i}$ Internal Supercapacitor Resistance(ESR) [Ω]

$\mathbf{R(s)}$ Input Signal in Laplace Domain

$\mathbf{s}$ Laplace Complex Angular Frequency

$\mathbf{t}$ Time [sec]

$\mathbf{T_p}$ Peak Time [sec]

$\mathbf{T_r}$ Rise Time [sec]

$\mathbf{T_s}$ Switching Period [sec]

$\mathbf{T_{set}}$ Settling Time [sec]

$\mathbf{V}$ Voltage [Volt]

$\mathbf{V_{batt}}, \mathbf{V_b}$ Voltage Battery [V]

$\mathbf{V_{in}}$ Input Voltage Converter [V]

$\mathbf{\Delta V_{IR}}$ Effective Internal Resistance Voltage Drop [V]

$\mathbf{V_o}$ Output Voltage Converter [V]

$\mathbf{V_0}$ Open Circuit Voltage [V]

$\mathbf{\Delta V_P}$ Polarization Voltage Drop [V]

$\mathbf{V_r}$ Rated Voltage [V]

$\mathbf{\Delta V_R}$ Relaxation Voltage Gain [V]

$\mathbf{V_{sc}}, \mathbf{V_c}$ Voltage Supercapacitor [V]

$\mathbf{V_{Th}}$ Thevenin Voltage [V]

$\mathbf{W}$ Energy [J],[Wh]

$\mathbf{Z_{Th}}$ Impedance Thevenin [Ω]

%**OS** Percent Overshoot [%]

$\delta(t)$ Impulse Test Function

δ Fractional Voltage Drop across the Battery Internal Resistance [-]

ϵ Power Sharing Factor [-]

γ Power Enhancement Factor [-]

λ RMS-factor Battery

μ RMS-factor Supercapacitor

$\Phi(t)$ Unit Step Function

ϕ_{PM} Phase Margin [°]

ω_{BW} Bandwidth [Hz]

ω_n Natural Frequency [Hz]

τ Time Constant [sec]

$\tau_{\mathbf{b}}$ Run-time Battery-Alone System [sec]

$\tau_{\mathbf{hybrid}}$ Run-time Hybrid System [sec]

$\zeta_{\mathbf{c}}$ Current Sharing Factor [-]

ζ Damping ratio [-]

List of Figures

List of Tables

Table of Contents

1 Introduction

1.1 Background

Today, centralized power generation from large-scale power plants possess a vital position in industralized societies worldwide. However, the majority of the existing power generation technology is based on non-renewable energy resources, such as fossile and nuclear fuels. Facing depletion of these conventional energy sources and their undoubted negative effects on climate and environment, it is necessary to develop new renewable energy technologies and energy management strategies that is environmentally and economically sustainable on a long term basis. However, integrating the existing and realizable renewable energy technologies into the existing power systems, gives rise to a range of new challenges. Contrary to the conventional energy sources, many renewable technologies, such as wind power and solar power, is dependent on immediate weather conditions, making them less controllable and predictable. This complicate the management of the power system, since the supplied power at all times must match demand. Therefore, *hybridization* of renewable energy technologies together with energy storage technologies is an attractive alternative, making it possible to store surplus energy when the demand is low, and increase production when the demand is high.

The Institute of Energy Technology(IFE) has since 1997 developed an experimental laboratory facility(REHYS) for testing a hybrid energy system based on renewable energy. The systems main components are a Proton Exchange Membrane Fuel Cell, a lead acid battery module and a Photovoltaic(PV) array, which are connected to a centralized DC-bus architecture(46-58 V) directly or via power electronic interface. The DC-bus is connected to the utility AC-grid using an inverter.

Because a stand-alone PV-power-system has a limited controllability, the hybridization with battery and fuel cell, enable energy storage when the PV-power-output is larger than demand and ensures uninterruptable power supply when the PV-power-output is lower than demand. However, being directly connected to the DC-bus, the battery is immediately responding to sudden load changes, resulting in repeated transient charging and discharging. This could reduce the battery lifetime.

A solution to this, could be to integrate a *supercapacitor* into the system. Supercapacitors are characterized by their fast charge and discharge capability, highly reversible process functionality, high power density and relative low energy density compared to batteries. Hence, integrating a supercapacitor into the energy system in the REHYS-laboratory, can have a positive effect on the system operation stability. Due to its unique performance characteristics, a supercapacitor can relieve the battery of narrow and repeated transient charging and discharging, ensuring longer battery life.

1.2 Purpose, method and structure

The main purpose of this thesis is to examine the effects of integrating a supercapacitor into the existing system in the REHYS-laboratory. The scope is thus limited to two objectives. The first objective is to examine the physical and electric characteristics of the supercapacitor as an alternative energy storage technology. On the basis of a literature review and of an electric characterization of the avvailable supercapacitor in the REHYS-laboratory, an equivalent model of the supercapacitor is formalized. The second objective is to examine the hybridization of supercapacitor and battery in detail. Two hybridization topologies are of interest: a *passive hybrid system*(PHS) and an *semi-active hybrid system*(SAHS). The PHS-topology consists of a direct parallel connection of the battery and the supercapacitor, directly connected to a load. The SAHS-topology consists of an indirect parallel connection of the battery, the supercapacitor and the load, using a DC/DC-converter. Both these topologies will first be analyzed, then modeled and simulated using the formulated supercapacitor model in Matlab/Simulink numerical computation software[1]. The PHS-topology will be tested in the REHYS-laboratory.

The structure of the thesis is then as follows. In section 2 a brief overview of the REHYS-system is presented. The purpose of hybridization is discussed together with a presentation of the different possible hybrid topologies.

In section 3 the physics, design and electric properties of the supercapacitor are generally discussed based on a literature review. The electric characterization of a BMOD00165 supercapacitor from Maxwell Technologies, is then presented together with an equivalent capacitor-model that will be used in the simulations.

The PHS-topology is examined in section 4. First, a detailed "a priori" analysis of the topology is presented, together with a formulation of a simplified equivalent model. Important performance characteristics such as *current sharing factor*, *power enhancement factor* and *power saving factor* are derived. Based on the model, the PHS-topology is compared with a battery-alone system(BAS) under specific load conditions. A pulse train load with different duty cycles and frequencies is used to analyze the behavior of the system under transient conditions. Second, the model is implemented in Matlab/Simulink and the analytical approach is confirmed through simulations[2]. Third, the PHS-topology is tested in the REHYS-laboratory and the measurements are compared with the results from the simulations.

In section 5 the DC/DC-converter used in the semi-active topology is presented. First, the design, operation and efficiency aspects are briefly discussed. Second, the low-pass filter of the converter is optimized according to predefined operation conditions. Third, the control and modeling of the DC/DC-

[1]Developed by Mathworks Inc. Simulink is a platform in Matlab for modeling, simulating and analyzing multidomain dynamic systems.

[2]Because the BMOD00165 supercapacitor has a rated voltage(48 V) that is below the maximum operating voltage of the system, it was decided that a supercapacitor with a higher rated voltage was needed in the PHS-topology. A BMOD0130 P056 from Maxwell Technologies with a rated voltage of 56 V and rated capacitance of 130 F was found to be sufficient. The module is electrically characterized and modeled according to the same method described in section 3.4 and 3.5.

converter is discussed. The objective is to design a feedback controller for the converter which enables us to control the current flowing to and from the supercapacitor. In order to capture the performance under a dynamic regime, it is beneficial to represent the converter circuit as an *dynamic average model*. An adequate control design is then formulated based on linear control theory using a proportional-integral-controller.

In section 6 the formulated control design is implemented in the *semi-active topology*. Possible control strategies are here discussed, and a simple control strategy based on power smoothing with moving average technique and over/under voltage protection is applied. Using Matlab/Simulink the control strategy is simulated and compared with the PHS-topology. Economic cost optimization problems will not be covered in this thesis, since the focus will be on the technical aspects and physical performance of the hybrid system.

2 System Overview and Hybridization

2.1 The REHYS-system

The hybrid energy system in the REHYS-laboratory, shown in figure 2.1, is based upon a common DC-bus architecture(48V), on which all the the system components are directly or indirectly connected. The *hydrogen proton exchange membrane fuel cell* (PEMFC), manufactured by HTI Biel, has a nominal power rating of 1,2 kW and the terminal voltage varies between 12-20 V. Its maximum current output is 100 A. The PEMFC is connected to the DC-bus using a DC/DC-step-up-converter, which boost up the PEMFC voltage to the DC-bus voltage.

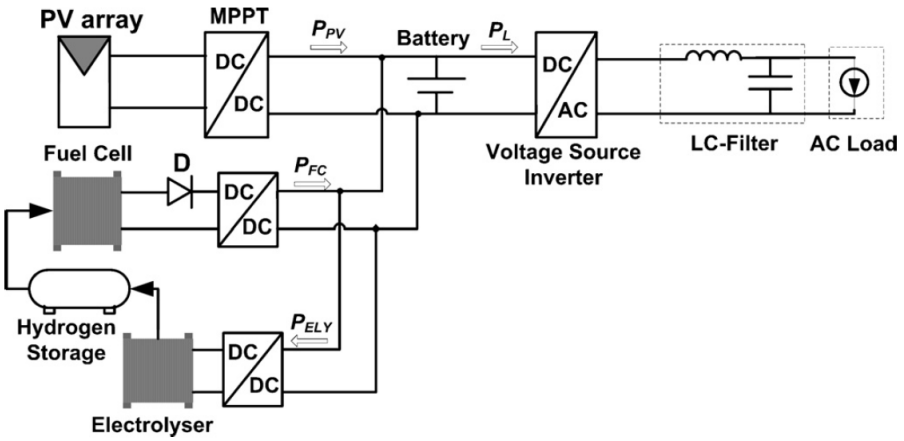

Figure 2.1: Schematic presentation of the hybrid power system in the REHYS-laboratory[1].

The photovoltaic array(PV) has a rated power output of about 4 kW, an open circuit voltage of 110 V, and a short circuit current of 49,8 A. At max power point(MPP) the voltage is 84,9 V and the current is 46,2 A. The PV is interfaced with the DC-bus through a DC/DC-step-down-converter with a MPP-tracking system. The MPP-tracking system continuously seeks the operating point at which the PV power output is maximized, regardless of irridiance and temperature[1].

The lead acid battery consists of four battery modules manufactured by Haze, each with a rated voltage of 12 V and capacity of 230 Ah. The modules are connected in series in order to produce a combined output voltage of 48 V and a total capacity of 230 Ah. Each module consists of 6 cells each with a nominal internal resistance of $2\,m\Omega$. That gives a total nominal internal resistance of $0,048\,m\Omega$. At 90 % state of charge the internal resistance has been measured to be $0,05\Omega$. It is connected directly to the DC-bus without any power electronic interface, and will thus be charged or discharged depending on the load profile.

It is also planned to integrate an electrolyzer into the system, that could produce hydrogen through electrolysis of water. The produced hydrogen could be stored in a metal hydrid storage tank during off-peak hours. In peak load hours,

the stored hydrogen can be re-electrified by the PEMFC. The rated terminal voltage of the electrolyzer would probably be below the DC-bus voltage, making it necessary to use a DC/DC-step-down converter between the electrolyzer and the DC-bus.

The DC-bus is connected with the AC-utility grid using a single phase voltage source inverter and a step up transformer, which inverts the DC-voltage into a single-phase AC-voltage of 230 V(rms) with frequency 50 Hz.

The system operation is regulated by a supervisory control unit in which a defined control strategy is implemented.

2.2 The purpose of hybridization

The hybrid energy system described above opens up a range of energy and power management possibilities, compared with a stand-alone PV-system. When there is a lack of solar irradiation or large fluctuations in the PV ouput, the PEMFC covers the base load ensuring uninterruptable power supplied to the load. But due to the fuel cell's relative slow dynamics, a hybridization with the faster responding battery enables the system to meet a step increase or decrease in power demand. Hence, using the battery together with the PEMFC, improves performance and the PEMFC life time since the battery absorbs faster load changes and prevents fuel starvation of the PEMFC[2].

To achieve an even faster respons, a supercapacitor could be integrated into the system. Supercapacitors are characterized by their fast charge and discharge capability, highly reversible process functionality, high power density and relative low energy density compared to batteries. Due to its unique performance characteristics, a supercapacitor can relieve the battery of narrow and repeated transient charging and discharging, ensuring longer battery life. The battery then takes on more extended peak loads, while the supercapacitor handles shorter bridge power tasks, as well as it can supply a power quality ride-through to compensate for momentary severe voltage sags, and operate as a power buffer for large momentary in-rush or power surges [3]. Since supercapacitors operate on a different principle than batteries, the supercapacitor is capable of sitting on a charge for extended periods without any loss of capacity. Batteries are notorious for loosing capacity when held on charge for extended periods.

The fundamental operation characteristics of the system components is therefore based on two properties: their *energy density* and *power density*. The gravimetric energy density of a system is generally defined as the amount of energy(Wh) that can be stored in the the system per unit mass(kg)[4]. The gravimetric power density of a system is defined as the amount of power(W) that the system can supply per unit mass(kg)[4].

Given a stable, constant power load with little transient behavior, the most important property of the system is its energy density. The system should be able to supply the load for as long as possible. However, when the load profile shows transient characteristics, meeting the instantaneous power demand becomes necessary, and the important property of the system is its power density. The Ragone diagram shown in figure 2.2 gives an overview of the energy storing properties of the different existing technologies.

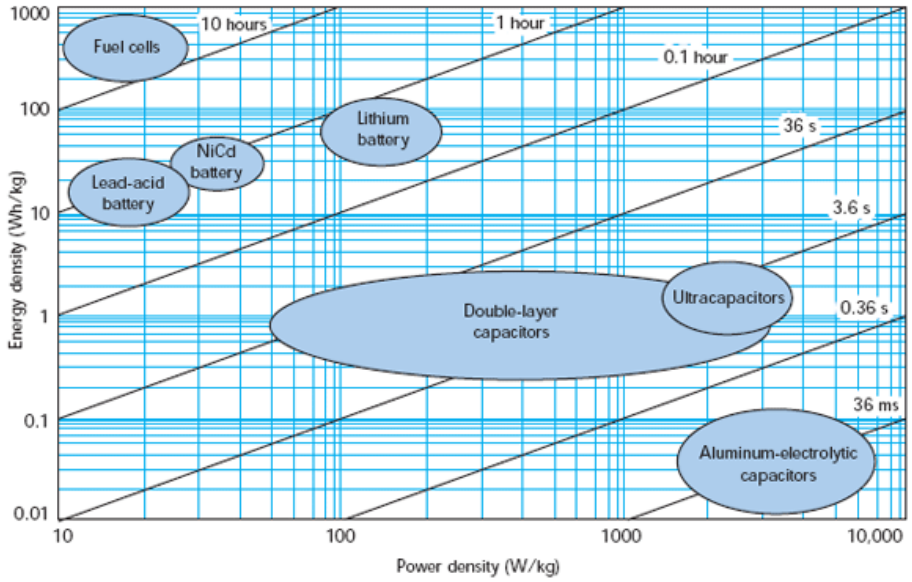

Figure 2.2: Ragone diagram with different energy storage technolgies. Vertical axis is the specific gravimetric energy density, horizontal axis is the specific gravimetric power density. The inclined lines specify the discharge time into a specific load[5].

One can see that fuel cells occupy the top-left posistion with energy densities up to 1 kWh/kg and a run time above 10 hours, but with a relatively small power density in the range of 10-20 W/kg. The conventional batteries has energy densities around 10 Wh/kg, a run time of 1 hour and power densities ranging from 10-200 W/kg, lead acid having the lowest power densities and lithium-ion batteries having the highest power densities. Supercapacitors and ultracapacitors bridge the space between batteries and conventional electrolytic capacitors. They have relatively low energy densities and considerably lower run time than batteries and fuel cells, but their power densities could reach as high as 5 kW/kg.

Hence, in order to increase the power density of an energy system and to protect batteries and fuel cells from high power surges, supercapacitors can be integrated into a range of different applications, from memory maintenance systems, telecom applications and uninterruptable power supply(UPS), via hybrid vehicles and traction systems in trains and metro systems, to larger power generation systems[5].

Hybrid vehicles Supercapacitors are extensively used in electric vehicles(EV) and hybrid-electric vehicles(HEV). Regenerative braking systems capture some of the kinetic energy stored in the vehicle's moving mass by operating the traction motor as a generator that provides braking torque to the wheels and recharge the batteries. The electric load profile consists of high peaks and steep valleys due to repetitive acceleration and deceleration. The resulting current surges in and out of the battery tend to generate extensive heat inside the battery, which lower the efficiency of the battery and in the long run reduces its lifetime. When hybridizing the battery with a supercapacitor, the supercapac-

itor can assist the battery when extra power is needed during acceleration and hill climbing, and additionally capture the regenerative braking energy. This allows for a smaller battery size and an increased battery lifetime[6][7].

2.3 Hybridization of battery and supercapacitor

2.3.1 Lead acid battery

The lead acid battery(LAB) is a cost effective, recyclable storage battery with good performance and life characteristics. The LAB consists of lead dioxide, PbO_2, as the active material of the positive electrode and metallic lead, Pb, as the active material of the negative electrode. The electrolyte is a sulfuric acid solution, H_2SO_4. As the battery discharges, the lead in the negative electrode oxidizes(Pb^{2+}) and forms lead sulfate, $PbSO_4$, when reacting with the electrolyte. Free electrons($2e^-$) can now flow through an external load circuit into the positive electrode, where fourvalent ions(Pb^{4+}) reduces to Pb^{2+}. When the battery is being charged, the process is reversed. The overall reaction can be formalized as[8]:

$$Pb + PbO_2 + 2H_2SO_4 \rightleftarrows 2PbSO_4 + H_2O \tag{2.1}$$

As we saw above, LABs are characterized by their relatively high energy density, but low power density. Given a stable load, a battery-alone system would meet the load efficiently. However, when the load profile shows transient characteristics, meeting the instantaneous power demand becomes important. This could be solved by dimensioning the battery accordingly, but the power/energy trade offs often results in a non-optimal battery configuration[9][8]. Additionally, PV-panels are not an ideal source for battery charging, since their output is highly stochastic and unpredictable.

For a lead acid battery, a number of different factors can influence the battery lifetime[3]:

- High temperature increases self-discharge and has thus a negative effect on the state of charge(SoC). Due to the internal resistance of the battery, the operating temperature will increase with increasing charge/discharge current[8].
- Fluctuations in the state of charge will in the long run result in a decrease in the state of health of the battery, due to irreversible sulfation($PbSO_4$) on the electrodes and degradation of the active material, thus reducing its lifetime[10]. A typical lead acid battery has a cycle-life ranging from 500-2000 charge/discharge cycles. The cycle life is reduced with increased depth of discharge(DoD) of each cycle[8].
- DoD affects the level of corrosion and sulfation, and hence the lifetime. DoD should be kept as low as possible[10].

[3]The lifetime prediction of lead acid batteries requires a detailed electrochemical understanding of ageing processes and their causes, which is outside the scope of this thesis. Here, the most important causes of battery degradation are briefly summarized in order to formulate the main motivation for hybridization.

- Overcharging of the battery could lead to gassing[10][11][4]. However, this can be mitigated using battery management systems with overvoltage protection.

2.3.2 Hybrid topologies

Integrating a supercapacitor with high power density into the system could solve the battery optimization problem and reduce the stresses on the battery under fluctuating load conditions. The relatively small internal resistance of the supercapacitor compared to a battery and the high number of possible charge/discharge cycles, results in a charge/discharge efficiency that is much higher than of any battery. Hence, a hybridization of battery and supercapacitor, can give reduced system losses and higher efficiency which contributes to prolonged system life time and lower operating temperature[9][11].

The desired operation of a hybrid system is as follows: the battery should supply a nearly constant(average) load current, reducing the internal ohmic losses and preventing terminal voltage dips, while the supercapacitor should match the battery to the load by supplying the dynamic current with zero average. During high load demand, both the battery and the supercapacitor supply charge to the load, while during low load demand, the battery supplies both the load and recharge the supercapacitor. This should reduce the voltage and current ripple of the battery.

In the following we will examine two different types of battery-supercapacitor hybrids: the *passive* and the *active* system topology. The PHS-topology consists of a direct, parallel connection of the battery and the supercapacitor, and a direct connection to the load. The obvious advantages of this topology are the simplicity and the absence of power electronics and control circuitries, reducing costs and increasing the system robustness and reliability[9]. The main drawback is the fact that the load current is shared between the battery and the supercapacitor in a nearly uncontrolled manner, determined predominantly by their internal impedances. Because of this, the terminal voltage of both components must be nearly equal at all times. If the supercapacitor voltage becomes significantly lower than the battery voltage, unacceptable high currents will flow from the battery to the supercapacitor, making it necessary to implement some kind of current protection. This limits the operation range of the supercapacitor and limits the amount of energy that can be extracted from it during discharge.

In the *active/semi-active topology*, one or more DC/DC-converters are used to control the flow of current to and from the system components. In a *fully active topology* two converters are applied, while in a*semi-active topology* only one converter is used. The alternatives for the semi-active topology are[9]:

- *Parallel semi-active hybrid*: the converter is between the load and the power sources
- *Battery semi-active hybrid*: the converter is between the battery and the load, connecting the supercapacitor directly to the load side

[4]Hydrogen evolves at the negative electrode and oxygen at the positive electrode.

- *Capacitor semi-active hybrid*: the converter is between the supercapacitor and the load, with the battery directly connected with the load

Here we will focus on the *capacitor semi-active hybrid*, shown in figure 2.3, which to date is the realizable topology for our system.

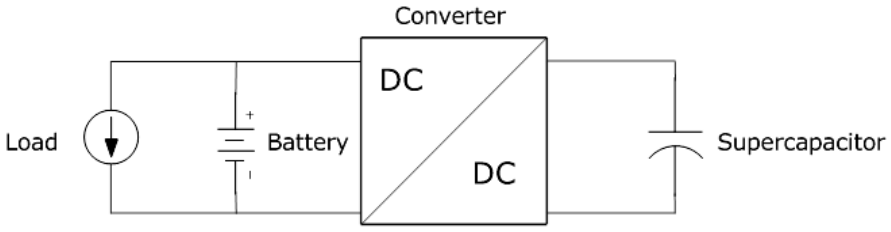

Figure 2.3: The capacitor semi-active hybrid topology.

Using a bi-directional DC/DC converter between the supercapacitor and the DC-bus, the battery is directly connected to the common DC-bus and hence directly coupled with the load. This enables us to control the current going to and from the supercapacitor and makes it possible to formulate a set of control strategies for optimizing the hybrid system performance. Contrary to the passive topology, voltage matching between the capacitor and the battery is no longer required. This expands the operation range of the supercapacitor and enable us to discharge the supercapacitor to about half of its rated voltage, extracting up to 75% of the stored energy.

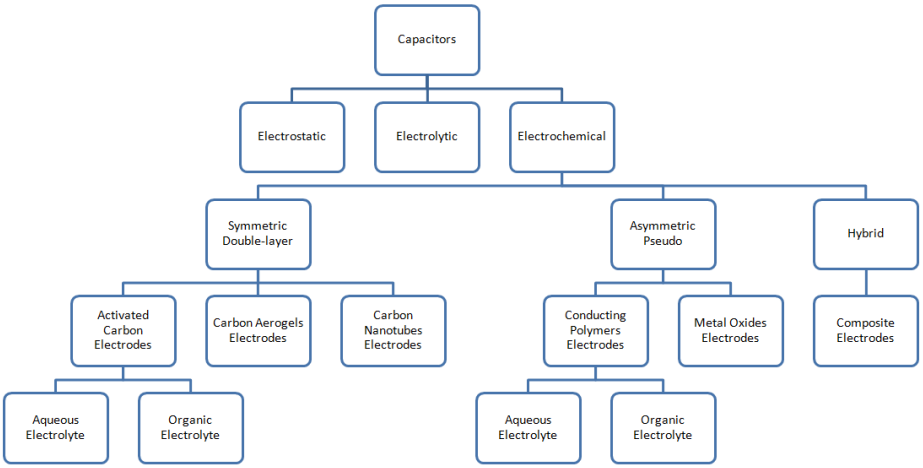

Figure 3.1: Hierarchical categorization of different capacitors

3 Supercapacitor

The capacitor is a fundamental electric component characterized by its ability to store energy in an electric field developed through the accumulation of electric charge. The capacitor's ability to accumulate electric charge and store electric energy, is defined by its *capacitance*.

Capacitors can in general be divided into three general categories: *electrostatic*, *electrolytic* and *electrochemical*. The electrostatic capacitor is the conventional capacitor, consisting of two conducting plates with an isolating *dielectric* between the plates. An electrolytic capacitor employs a conductive electrolytic salt in direct contact with the electrodes, instead of a dielectric. This reduces the effective plate separation and thereby increases the capacitance of the capacitor. As an advanced version of the former, the electrochemical capacitor employs sophisticated porous electrodes with an electrolyte in between, which increases the capacitance even more.

To date, there exists no consistent nomenclature in describing electrochemical capacitors(EC), and there are some confusion in the industry and the literature regarding the terminology. The most common names used are supercapacitor, ultracapacitor, pseudocapacitors and double-layer capacitors[12]. Though, ECs can be divided into three general categories depending on physical properties and different energy storing mechanisms: symmetric double-layer EC(EDLC), asymmetric pseudocapacitors and hybrid capacitors[13]. The main energy storing mechanism are respectively non-Faradaic electrostatic(EDLC), Faradaic (pseudo) and a combintaion of the two(hybrid).

Where the EDLC employs the same material for the positive and negative electrode, the asymmetric pseudocapacitor uses two different materials. EDLCs accumulate electrostatic charge through the accumulation and separation of

ions at the interface between the electrolyte and electrodes. On the other hand, the asymmetric pseudocapacitor accumulates charge mainly through Faradaic reduction and oxidation(redox)reactions that takes place at the electrode and electrolyte interface[13][12]. However, in an EDLC there's also the presence of unwanted secondary Faradaic processes which may play a role in the discharge profile of the capacitor[14]. In figure 3.1 an overview over the different categories of capacitors can be seen.

In the follwing the focus will be on EDLC, which to date is the most used supercapacitor technology. From now on the term supercapacitor will be used for EDLC.

3.1 Capacitor fundamentals

The basics of a supercapacitor are no different from those found in an conventional capacitor.

An electrical field develops between two electrically charged electrode-plates. One plate is positively charged, the other is negatively charged. The potential difference V is directly proportional to the distance between the plates d and to the strength of the electric field E, through the relationship: $V = E \cdot d$. The ratio of charge Q to the potential difference defines the *capacitance* of the capacitor[15]:

$$C = \frac{Q}{V}[Farad] \tag{3.1}$$

Differentiating this equation with respect to time and reformulating gives:

$$\frac{dV(t)}{dt} = \frac{1}{C} \cdot \frac{dQ}{dt} = \frac{1}{C} \cdot I \tag{3.2}$$

One can see that, provided a constant current, the voltage will rise linearly with a slope equal to the inverse of the capacitance.

There will be a maximum voltage limit for a capacitor defined by the so called *breakdown voltage*. At breakdown voltage a portion of the insulating material(dielectric, electrolyte, air) between the conductor plates becomes electrically conductive and a short circuit channel devolops[3].

If a higher operating voltage is needed for the capacitor, it is possible to connect more capacitors in series. However, this will lower the total equivalent capacitance of the module C_{eq} compared to the capacitance of n individual capacitors, given by the relation[15]:

$$V_{module} = V_1 + V_2 + ... + Vn = Q(\frac{1}{C_1} + \frac{1}{C_2} + ... + \frac{1}{C_n})[Volts] \tag{3.3}$$

$$\frac{1}{C_{eq}} = \frac{1}{C_1} + \frac{1}{C_2} + ... + \frac{1}{C_n}[1/F] \tag{3.4}$$

The state of charge becomes equal for all capacitors, independent of their capacitances: $Q_1 = Q_2 = Q_n$.

When capacitors are being connected in series, any mismatch between the individual units manifest itself as unevenly distributed voltage across the capacitors beacuse by definition, the charge on each will be the same. There is

therefore a danger of exceeding the rated voltage on one of the capacitors. A solution to this is to employ voltage balancing with either *passive* or *active* techniques[5].

If a higher capacitance is needed, one can deploy sevaral capacitors in parallel, whereby the potential drop V across each capacitor remains the same. The total state of charge on n capacitors is then given by[15]:

$$Q_{total} = Q_1 + Q2 + ... + Qn = (C_1 + C_2 + ... + C_n) \cdot V[Coulomb] \tag{3.5}$$

The total capacitance becomes the sum of the capacitances of the individual capacitors:

$$C_{eq} = \frac{Q_{total}}{V} = C_1 + C_2 + ... + C_n[F] \tag{3.6}$$

In general, the potential energy stored in the electric field is given by[15]:

$$W = \frac{1}{2}CV^2[Joules] \tag{3.7}$$

When the capacitor is discharged, the voltage drops from the initial voltage V_1 to the voltage V_2, and in the process it releases some of the stored potential energy according to:

$$\Delta W = \frac{1}{2}C(V_2 - V_1)^2 \tag{3.8}$$

The *state of charge* of the supercapacitor, SoC_{sc}, is defined as the ratio between the remaining energy and the maximum stored energy of the supercapacitor. Using $W = \frac{1}{2}CV^2$, the state of charge expressed in terms of terminal voltage becomes:

$$SoC_{sc} = \frac{W}{W_{max}} = \frac{V^2}{V_{max}^2} \cdot 100\% \tag{3.9}$$

where V is the terminal voltage of the supercapacitor and V_{max} is equivalent to the rated voltage of the supercapacitor.

For supercapacitors it is common to specify its effective power densisty. The volumetric density is power per volume and the gravimetric density is power per mass. The peak gravimetric power density is defined as the instantaneous power delivered at full rated voltage V_r with an internal resistance, ESR, specified at 1 kHz frequency[3][5]:

$$P_{max} = \frac{(V_r)^2}{4 \cdot ESR_{1kHz} \cdot mass}[W/kg] \tag{3.10}$$

The nominal gravimetric power density is defined between a 20% to 40% voltage drop from rated voltage with internal resistance, with ESR specified at DC[3]:

$$P_d = \frac{0.12 \cdot (V_r)^2}{ESR_{dc} \cdot mass}[W/kg] \tag{3.11}$$

The capacitance varies directly with the area A of the parallel plates and inversely with the distance between the plates through the relation[15]:

[5]ESR = Equivalent Series Resistance

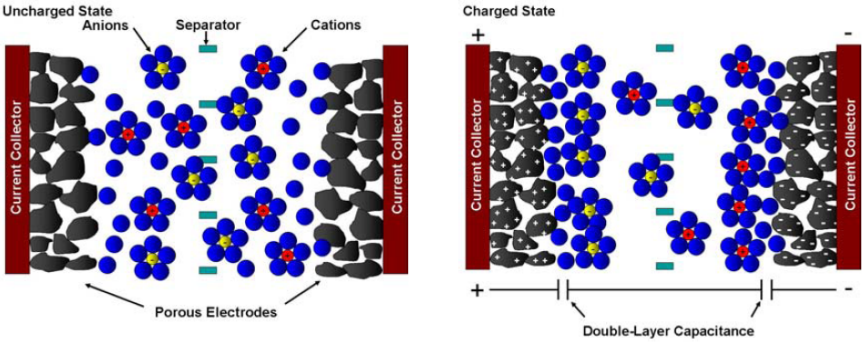

Figure 3.2: Principal sketch of a double layer supercapacitor, uncharged state at the left, charged state to the right[12]

$$C = \frac{\epsilon_0 \epsilon_r \cdot A}{d}[F] \tag{3.12}$$

where ϵ_0 is the permittivity constant of vacuum and ϵ_r is the relative dielectric constant of an eventual insulating dielectric between the plates.

3.2 Physics and design

One can easily see from (3.12) that the capacitance can be increased by maximizing the effective area and reducing the effective electrode separation. Supercapacitors achieve their high capacitance values in order of thousands of Farads by using sophisticated porous electrode materials with large effective surface area instead of homogeneous conductor plates, and an electrolyte with mobile ions instead of a dielectric, which reduces the charge separation to molecular dimensions.

When an electrical potential is applied across the electrodes, electrons accumulate on the negative electrode(cathode) and there's an vacancy of electrons on the positive electrode(anode). Ions in the form of cations and anions in the electrolyte migrate towards charges of opposite polarity accumulated on the electrodes. The phase boundary of only a few nanometers that develops between the electrode and the electrolyte, is the analog to the dielectric layer of a conventional capacitor. Across this boundary are two layers of excess and opposite charge created, called the electrochemical double layer[5]. Within this layer the capacitance is established and energy is stored in the electric field.

To separate anode and cathode, a thin isolation membrane, a *separator*, is located between the electrodes of the supercap, through which the mobile ions can diffuse. The porous electrodes are bonded to the current collectors, which are then connected to external metal leads that are the positive and negative terminals of the device. A principal picture of the design is shown in figure 3.2.

The assembly of the double layers vary from product to product. Typically the electrodes are wound into a roll configuration and assembled into a cylindrical cell package. The electrodes has foil extensions that are welded to the

cell terminals to enable a current path outside the capacitor [3]. Because the distance between the electrodes is small, the breakdown voltage is lower than that of conventional capacitors. Standard operating voltages for an individual capacitor cell is up to 3V[5].

3.2.1 Electrodes

Activated carbon is the most commonly used electrode material in supercapacitors. The developed surface area of carbon is essentially consisting of micropores($< 2nm$) mesopores($2 - 50nm$) and macropores($> 50nm$), which gives a specific area of around $1000m^2/g$[13]. However, in practice the real surface differs significantly from the electrochemical active surface that is accessible for the electrolyte ions.

Research has shown that the ions probably are too large to diffuse into smaller micropores, thus lowering the active surface area[13][16]. Research also suggests an empirical relationship between the distribution of pore sizes, energy density and power density. Larger pore sizes correlate with higher power densities, while smaller pore sizes correlate with higher energy densities[16]. Pore size distribution is therefore an important focus of attention in supercapacitor research.

Another alternative electrode material is *carbon aerogels*. It has a continuous structure and, contrary to activated carbon, it has an ability to bind chemically with the current collector, thus eliminating the need for an additional adhesive binding agent. Because of this, carbon aeorgels gives lower ESR values than activated carbon[16].

In more recent research there have been an interest in the use of *carbon nanotubes* as electrode material. Contrary to the materials mentioned above, the mesopores in carbon nanotubes are interconnected, allowing a continuous charge distribution that increases the available surface area. So even though carbon nanotubes have a modest surface area compared to activated carbon, the area is utilized more effectively because the ions can diffuse more easily into the mesoporous network. Like carbon aeorgels, carbon nanutubes can be grown directly onto the current collectors, thus achieving reduced ESR and higher power densities[13][16].

3.2.2 Electrolyte

Contarary to the conventional capacitor, a supercapacitor has an electrolyte which contains free space charges in the form of ions. The electrolyte is usually either aqueous or organic. Aqueous electrolytes, such as H_2SO_4 and KOH, generally have lower internal resistance(ESR) and lower minimum pore size requirements than organic electrolytes, such as *acetonitrile*. Aqueous electrolytes have however lower breakdown voltages, so one must consider the tradeoffs between capacitance, ESR and operating voltage. Although the electrolyte plays a crucial role in the characteristics of the supercapacitor, the subclasses of electrochemical double-layer supercapacitors is primarily distinguished by the type of electrode materials used[13].

3.2.3 Pseudocapacitance

Pseudocapacitance arises when the charge required for the progression of an electrode process is a continuously changing function of the terminal voltage. This enhances the overall value of the capacitance of the supercapacitor[16][17][13]. The term *pseudo* is used to describe the part of the double-layer capacitance that arises due to quick faradaic charge transfer reactions, as complementary to the pure electrostatic capacitance. As can be seen from the voltammetry characteristics in figure 3.3, the capacitive current is independent of the voltage in an ideal electrostatic capacitor. Introducing an ohmic resistive component results in a linear releationship. However, the pseudocapacitive characteristic deviate from the other, in that it shows distinctive peaks due to redox reactions in the capacitor. One can also observe a delay in the potential when reversing the potential sweep. This is due to the relative kinetically slow process involved during charging the pseudocapacitance[16].

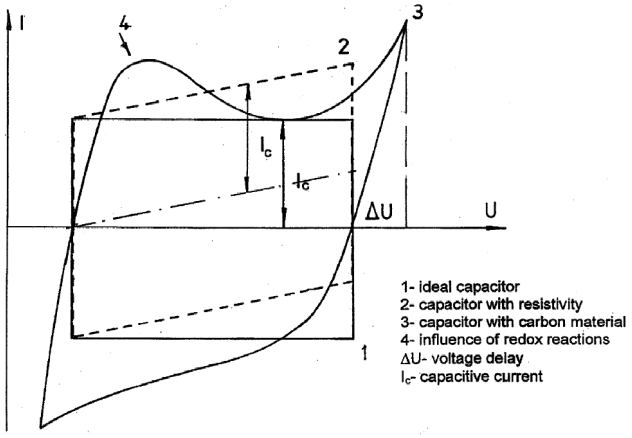

Figure 3.3: Comparison between ideal electrostatic voltammetry characteristics and voltammetry characteristics due to influence of pseudocapacitance[16]

Carbon materials can generally be modified to enhance the pseudocapacitance through the use of special oxidation of the carbon, formation of composites of carbon and polymers and/or insertion of electroactive particles of transition metals oxides into the carbon material[16][13]. Although pseudocapacitance effects enhances the capacitance value, it also increases the level of *self-discharge* resulting in a faster voltage decay when the capacitor is left with open terminals[17][16].

3.2.4 Frequency dependency

The internal ohmic resistances and the capacitance of the supercapacitor depends on the frequency of the applied voltage or current. Electrochemical impedance spectroscopy(EIS) is a general approach to characterization of electrochemical behaviour of energy storage devices. With EIS it is possible to analyze the influence of voltage and current frequency on the electrode series

resistance and on the capacitance of the supercapacitor[18][17][19][6]. By measuring the current amplitude and phase with respect on the injected voltage, the real and imaginary part of the impedance can be determined. Typical results from EIS experiments are shown in figure 3.4.

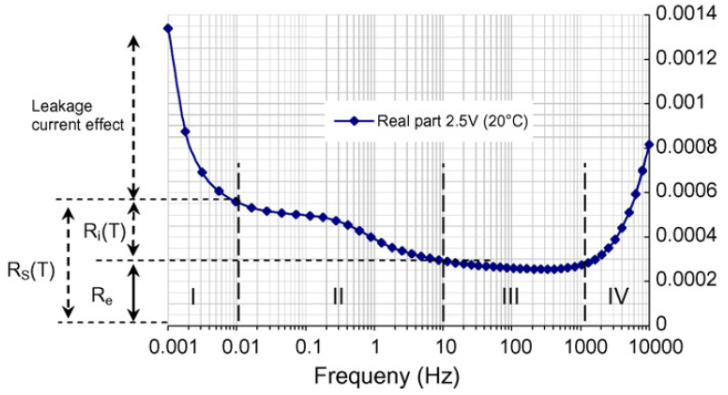

Figure 3.4: Impedance real part as a function of frequency [18]

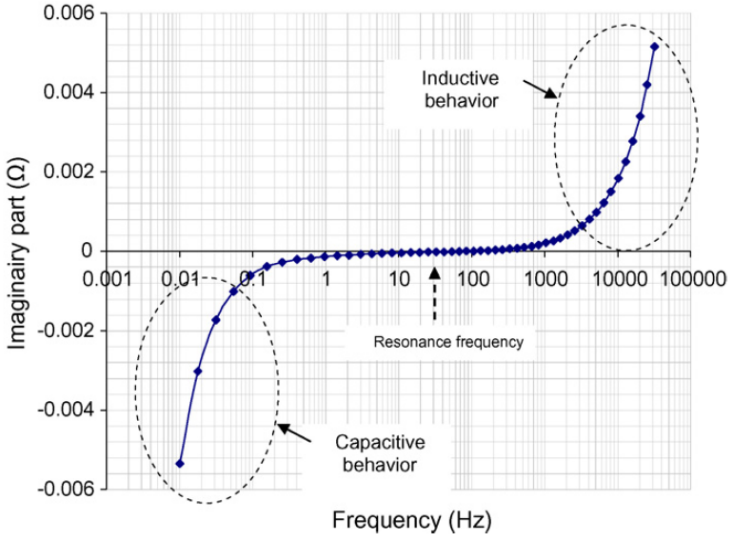

Figure 3.5: Impedance imaginary part as a function of frequency [18]

From the *real impedance profile* in figure 3.4 one can observe a steep rise in ohmic resistance as the frequency approaches zero(zone I). This is assumed

[6]EIS is implemented through the polarization of the supercapacitor with a DC-voltage. Then a small voltage ripple is superimposed on the DC-voltage. The ripple can typically be varied between 1 mHz and 10 kHz[18].

to be caused by an electronic leakage current through the separator, to the charge redistribution effects inside the electrode and to self-discharge. Zone II up to 10 Hz is dominated by the electronic resistance and the ionic resistance of the electrolyte. The sum of these resistances is recognized as the ESR of the capacitor. As the frequency increases, the ions are not able to reach as deep into the carbon pores, resulting in a smaller path and reduced ionic resistance. At around 1 kHz the only resistance left is the electronic resistance, composed of measurement connections, contact resistance between carbon electrodes and current collectors as well as the minimal resistance of the electrolyte[3][18]. [7]

The *imaginary impedance profile* in figure 3.5 shows that the capacitor behaves like an inductor at high frequencies. As the frequency approaches dc($f < 0.1Hz$), the impedance becomes more and more capacitive. The physical reasoning behind this, is that at low frequencies, close to dc, the ions in the electrolyte have time to reach the electrode surface which is hidden deep in the carbon pores. As the frequency increases, the ions are not able to follow the constantly changing applied electric field, and cannot reach the depth of the electrode pores[18]. A typical frequency dependent capacitance profile is shown in figure 3.6.

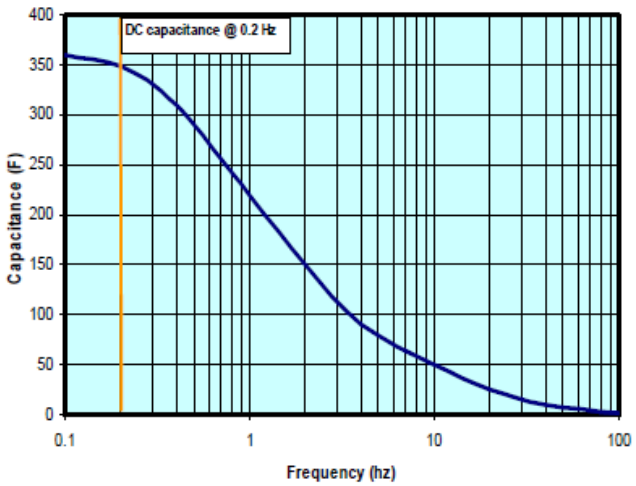

Figure 3.6: Capacitance as a function of applied frequency[3]

3.2.5 Temperature dependency

Many applications that utilizes a supercapacitor, for example hybrid vehicles, operate at different environment tempeartures. It is mainly the ionic resistance part of the ESR that is influenced by temperature due to changes in the viscosity at low tempeartures below 0 °C. The capacitance at the other hand shows little dependency on temperature at optimal frequency operation, but decreases some in the middle frequency range[18][17]. A typical profile of ESR and capacitance dependency on temperature can be seen in figure 3.7.

[7] Usually the supercapacitor manufacturers specify the ESR at DC and 1 kHz respectively.

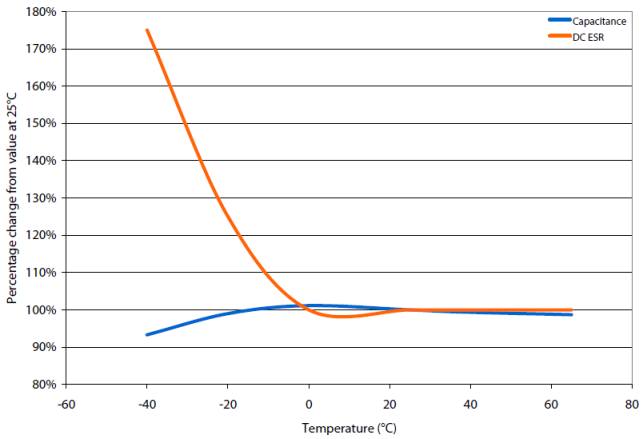

Figure 3.7: Typical profile of ESR and capacitance dependence at different tempeartures at optimal frequency operation[20]

Also the self-discharge rate of the capacitor depend on the temperature. This is due to the acceleration of ionic transport processes with increasing temperature, which results in excess ionic concentrations near the electrodes of the supercapacitor. This leads to higher diffusion and thereby a higher self-discharge rate[17].

3.2.6 Voltage dependency

Contrary to a conventional capacitor, the capacitance of supercapacitor varies with the terminal voltage. A typical voltage dependent capacitance profile can be seen in figure 3.8

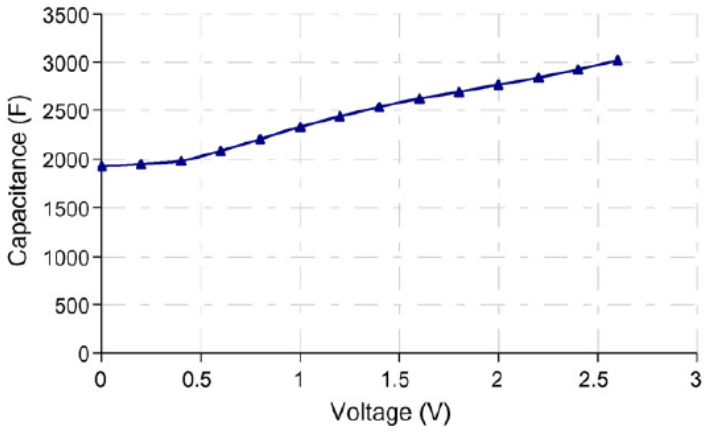

Figure 3.8: Capacitance as a function of voltage for a typical supercapacitor[18]

The physical interpretation of this phenomenon is not agreed upon in the literature, but could maybe be explained by a reduction of the distance sepa-

rating the charges at the phase boundary between electrode and electrolyte as the voltage increases[18]. In the formulation of adequate equivalent circuits, one should therefore take into account the *variable capacitance*.

The voltage dependent capacitance is expressed through the so called differential capacitance C_{diff} defined as the change in charge due to a change in voltage[21]:

$$C(V)_{diff} = \frac{dQ}{dV} \tag{3.13}$$

Dividing with the incremental time interval, dt, results in the following relationship:

$$\frac{dV(t)}{dt} = \frac{1}{C(V)_{diff}} \cdot i \tag{3.14}$$

One can utilize several different methods to derive $C(V)_{diff}$, where the most used method is a linear approximation resulting in an expression on the form: $C(V) = C_0 + K_v V$, where V is the applied voltage, C_0 is the capacitance close to zero voltage, and K_v is a constant slope(F/V)[22][21][17][8].

3.2.7 Self-discharge and charge redistribution

According to [23][17], the process of self-discharge in the capacitor can be ascribed to three mechanisms. The first mechanism is a consequence of overvoltage events and can be ignored under normal conditions, while the second is a diffusion-controlled Faradaic process that dominates the self-discharge in the first few hours. This is due to excess ionic concentration that can occur near the interface if the capacitor is charged to a threshold voltage. When the capacitor is disconnected from the charging power source, part of its charge will undergo a self-discharge redox process due to impurities such as water contamination in the interface. The mechanism can be modeled by the linear approximation[23]:

$$V(t) = V_0 - m\sqrt{t} \tag{3.15}$$

where $V(t)$ is the capacitor voltage during the first self-discharge period, V_0 is the initial voltage and t is the self-discharge time and m is a diffusion parameter. The third mechanism is a non-Faradaic electric process which dominates the self-discharge characteristic on the longer term. This mechanism is due to internal ohmic leakage pathways in the interface, resulting in a leakage current and capacitance reduction. It can be simply modeled by the well known exponential decay of capacitor voltage due to discharge through a resistor[23]:

$$V = V_0 \cdot e^{(-\frac{t}{R_{leak}C)}} \tag{3.16}$$

where R_{leak} is the constant long term leakage resistance and C is the capacitance of the supercapacitor.

However, in [24] it is argued that the observed voltage decay is not caused mainly by real self-discharge, i.e. leakage pathways or charge carriers going into faradic side reactions, but overall is due to the *redistribution* of charge carriers

[8] On the basis of a measurement with constant charge/discharge current, one can also derive a more accurate expression describing voltage as a function of time $V(t)$, for example by curve fitting using non linear least squares techniques. Differentiating $V(t)$ with respect to time, makes it possible to relate $C(V)_{diff}$ directly to the given voltage profile, given a constant current I.

inside and between the carbon pores that eventually can be discharged from the capacitor with sufficient discharge time. This argument is based on studies of the impact of charging duration and charging history of the supercapacitor. The impact of charging history can be observed in figure 3.9.

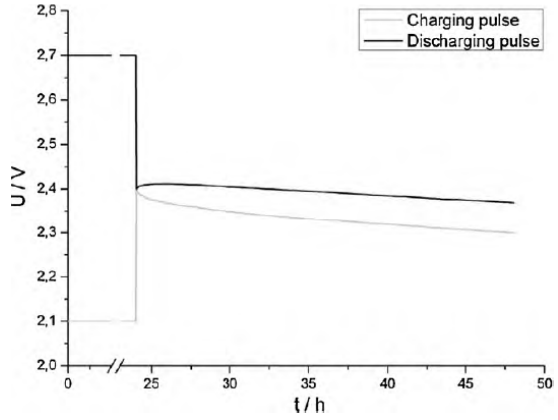

Figure 3.9: Open circuit voltage profile after charging pulse and discharging pulse[24]

As can be seen, there is a recovery effect of the open circuit voltage after a discharging pulse, while there is a decay effect after a charging pulse. The temporary increase of the voltage after the discharging pulse takes up to several hours, which indicates a redistribution of ions throughout the carbon pore system[24].

3.3 Equivalent circuits

The electric characteristics of a supercapacitor are more complex than that of a conventional capacitor. An ideal conventional capacitor will store and convert all energy without losses. For a real conventional capacitor there will be losses due to internal resistance and leakage currents. To model the beahavior of such a capacitor, it is usally sufficient to use the equivalent circuit shown in figure 3.10.

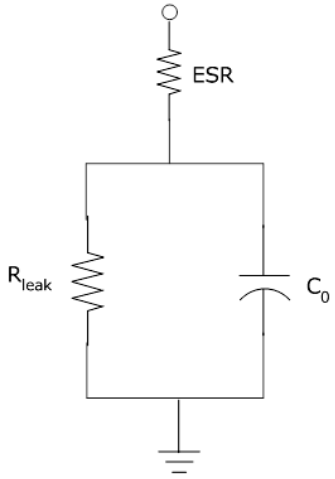

Figure 3.10: Equivalent circuit for conventional capacitor with dielectric.

Here is C_0 the capacitance, the ESR is a small series resistance($m\Omega$ - range) repesenting the ohmic losses in the current collectors and conductors, and R_l is a large resistance($k\Omega$ - range) representing losses due to a leakage current in the capacitor. R_s is also called the equivalent series resistance(ESR)[9].

Due to the physics and the material characteristics of a supercapacitor, it is necessary to expand the simple model in figure 3.10. Different models with varied complexity have been presented in the literature. The equivalent circuit models employ fundamental circuit components such as resistors, capacitors, and inductors to model the complex processes[10] that take place inside the supercapacitor.

3.3.1 Equivalent circuits for detailed physical characterization

There have been developed complex multi-branch equivalent circuit models to capcture the physical mechanisms in the supercapacitor. In the so called *transmisson line network model* the resistances and non-linear capacitances represents the distributed ESRs and electrostatic double-layer capacitance intrinsic to each pore in the electrode material. There is also addional resistances in the electrode material and a diffusion resistance in the membrane that the mobile ions experiences[25][13]. A principal circuit of this type can be seen in figure 3.11 a). However, the inconvience of these models is the complex determination of the different elements and the simulation time required, bounded to the large number of RC-branches[18].

[9] One could also include an inductance, L, in series with the ESR to capture the inductance of wires and circuitry, but this effect is small and usually ignored.

[10] Processes regarding porous electrode behavior, voltage, frequency and temperature dependencies, redistribution of elctrical charges, and leakage current.

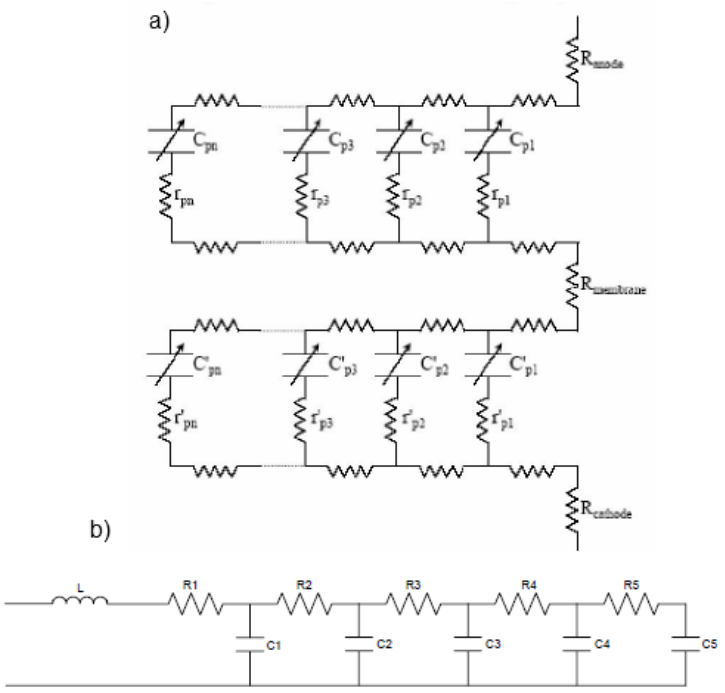

Figure 3.11: a) Transmission line network model[25] b) The ladder model[12].

The so called *ladder model* is a version of the transmission network model. Here it is assumed that the pores in the electrodes are cylindrical and are filled with homogeneous electrolyte solution. Each single cylindrical pore can be modeled by a uniformly distributed electrolyte solution resistance and double-layer capacitance. If the number of cylindrical pores on each electrode is assumed to be identical and grouped together, it can be simplified to a circuit simular to that shown in figure 3.11 b) [12].

3.3.2 Equivalent circuits for power electronic applications

The equivalent circuits used in the detailed modeling of supercapacitors mentioned above, are not convenient when the supercapacitor must be modeled as a part of a power electronic environment. Therefore, it has been presented simplified equivalent circuits that to a great degree manage to capture the characteristic behavior of supercapacitors under different operating conditions. Although the models show adequate correlations with experimental results, some have argued that these models have a weakness in that the circuit components lack a physical meaning. A physical interpretation is especially important for aging analysis and failure diagnosis[19].

In [21], Zubieta presented a basic equivalent circuit that has been used and developed futher in later research[18] [17] [19] [25]. The model can be seen in figure 3.12.

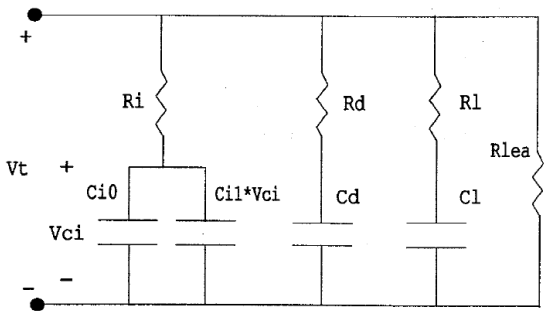

Figure 3.12: Equivalent circuit for supercapacitor after Zubieta[21].

The circuit in figure 3.12 is composed of three different RC-branches, which provide three different time constants to model charge transfer and redistribution within the capacitor as a function of time. The first branch consisting of R_i, C_{i0} and $C_{i1} * V_{ci}$ is called the immediate branch. With the shortest time constant, it dominates the immediate behavior of the capacitor in the time range of seconds in response to charge action. R_i represents in practice the ESR of the capacitor. The second intermediate branch with parameters R_d and C_d dominates the behavior in the range of minutes, while the third long term branch with parameters R_1 and C_1 determines the behavior for times longer than 10 minutes. R_{lea} is the leakage resistance($k\Omega$ range) that primarily governs the self discharge behavior of the capacitor at open circuit. A requirement for the circuit is that the proposed model parameters should be determined only using measurements at the capacitor terminals[21].

As a developed version of the Zubieta model, Rafik[18] has formulated the model shown in figure 3.13.

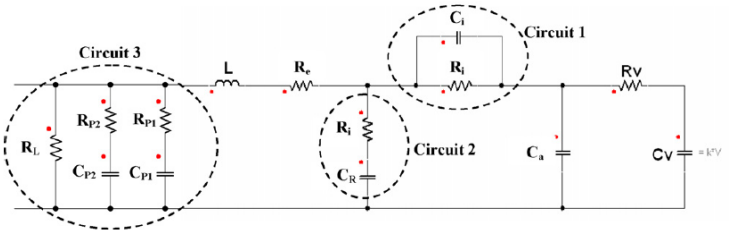

Figure 3.13: Equivalent circuit for supercapacitor after Rafik[18].

It takes also into account the frequency dependent parameters in the capacitor. Although additional components has been added, it carries many similarities to the Zubieta-model. Circuit 3 in the model, representing internal charge redistribution and leakage current, is identical to the intermediate and long term RC-branch of Zubieta's model. In addition, circuit 2 has been integrated to increase the accuracy at middle frequencies and circuit 1 has been introduced to model the electrolyte ionic frequency dependence in the low frequency range.

Because the ionic resistance is low at high frequencies, a capacitance C_i has been added in parallel to act as a short circuit at high frequencies. The right part of the circuit is similar to the immediate branch, with a voltage dependent capacitance C_V[18].

Faranda [22] proposes a simplified version of the Zubieta-model [21] with one RC-branch less, shown in figure 3.14. According to Faranda this simplifies the estimation of parameters and reduces the number and complexity of measurements, reducing the possibility of errors.

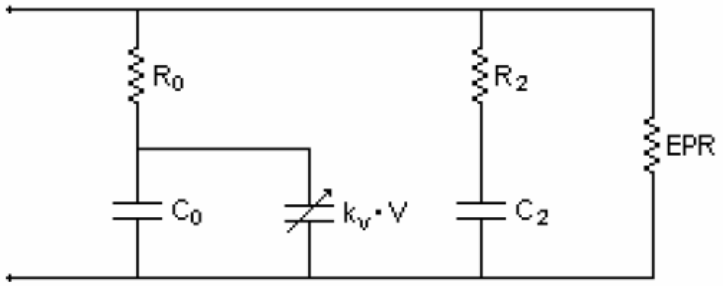

Figure 3.14: A simplified model for supercapacitor after Faranda[22].

Faranda proposes a method on determining the parameters in the model based on measurements.

Given two points $P_1(t_1, V_1)$ and $P_2(t_2, V_2)$ on the voltage-time curve during charging with constant current, C_0 and k_v can be determined by:

$$C_0 = \{\frac{t_1}{V_1} - \frac{V_1 \cdot t_2 - V_2 \cdot t_1}{V_2^2 - V_1 \cdot V_2}\} \cdot I_c \tag{3.17}$$

$$k_v = 2 \cdot \{\frac{V_1 \cdot t_2 - t_1 \cdot V_2}{V_1 \cdot V_2^2 - V_1^2 \cdot V_2}\} \cdot I_c \tag{3.18}$$

The parameters of the second RC-branch are determined by analyzing the intermediate behavior of the open circuit voltage after charging to a given voltage level. Analyzing the decay of the open circuit voltage in the intermediate term(up to 500 seconds), it would be possible to find the time constant of this approximately exponetial decay which should be approximately equal to the time constant of the intermediate branch: $\tau_2 = C_2 R_2$. After three time constants it is assumed that the voltage V_{2f} over both capacitances are the same, whereby one can use the total state of charge to calculate C_2, given by the equation:

$$Q_{tot} = I_c \cdot T_c = C_2 \cdot V_{2f} + (C_0 + \frac{k_v}{2} \cdot V_{2f}) \cdot V_{2f} \tag{3.19}$$

where I_c is the constant charging current before current interrupt, T_c is the charging time, and C_0 and k_v are describing the variable capacitance $C(V)$. R_2 is then given by $R_2 = \frac{\tau_2}{C_2}$[11].

[11]The proposed models above do not describe to great accuracy the long term self discharge behavior of the capacitor in open circuit mode. In [17] it is argued that an accurate model must

3.4 Measurements and results

In order to characterize the available supercapacitor, it has been conducted measurements on the supercapacitor in the REHYS-laboratory at IFE. In the following section these measurements will be presented together with a preliminary analysis.

3.4.1 Description of the supercapacitor

The supercapacitor available in the laboratory is a BMOD0165 manufactured by Maxwell Technologies, shown in figure 3.15.

Figure 3.15: The ultracapacitor BMOD0165 manufactured by Maxwell Technologies.

In Table 3.2 the product specifications can be seen. Maxwell Technologies uses the name ultracapacitor instead of supercapacitor. All capacitors produced by Maxwell Tech. utilizes an organic electrolyte, acetonitrile. This enables a higher operating voltage than with an aqueous electrolyte. Organic electrolyte has also a lower freezing point, which enables utilization over a wider range of temperatures. The model has activated carbon electrodes and uses a separator made of cellulose [26][3].

The capacitor should not be operated beyond the specified rated voltage. A failure with respect to the upper voltage limit will result in a shortening of the lifetime and in extreme cases, a failure resulting in venting of gasses that build up in the cell as a result of the overvoltage condition[3]. In order to secure optimal operation and longest possible life time, it is common in different applications to utilize the capacitor in a range between rated voltage and half the rated voltage. It follows from equation (3.8), that within this operating range, it is possible to utilize approximately 75% of the available energy.

---

incorporate a *variable leakage resistance* in order to characterize the self discharge processes. This model takes into account that the leakage resistance varies over a wide range, depending on the time after starting open circuit mode. After a steep rice in leakage resistance during the first 5 hours, it levels out and becomes approximately constant at a high level.

Rated capacitance	165 F	**Short circuit current(max)**	4 800 A
ESR(DC)	7,6 mΩ	**Energy density(max)**	3,81 Wh/kg
ESR(1kHz)	6,3 mΩ	**Power density(max)**	6 600 W/kg
Leakage Current(max)	5,2 mA	**Power density(DC)(max)**	2 600 W/kg
Thermal Resistance	0,25 °C /W	**Mass module**	14,2 kg
Rated Voltage	48 V	**Volume module**	12,6 L

Table 3.1: Product specifications for BMOD0165 [20]

3.4.2 Measurements and calculations

To perform tests on the supercapacitor, the test equipment available in the REHYS-laboratory was used. In order to verify the measurements done with the Digatron, a parallel test with an oscilloscope was conducted. The equipment used was:

- Battery Test System BTS-600
- Digatron Battery Tester - Model EVT 300-400 Thy, 150 kVA, 377 A
- Tektronix Oscilloscope - TDS 2012 B
- Boostcap Ultracapacitor from Maxwell Technologies - BMOD0165 - 165 F, 48 V

Parallel test with oscilloscope In order to verify the measurements conducted with the Digatron, a parallel test with an oscilloscope was conducted. The oscilloscope was connected directly to the terminal of the supercapacitor. There was an approximately 10 meter long cable going from the capacitor terminals to the Digatron measurement device. The oscilloscope has a measurement accuracy of 0.2 V, while the Digatron has an accuracy of 1 mV.

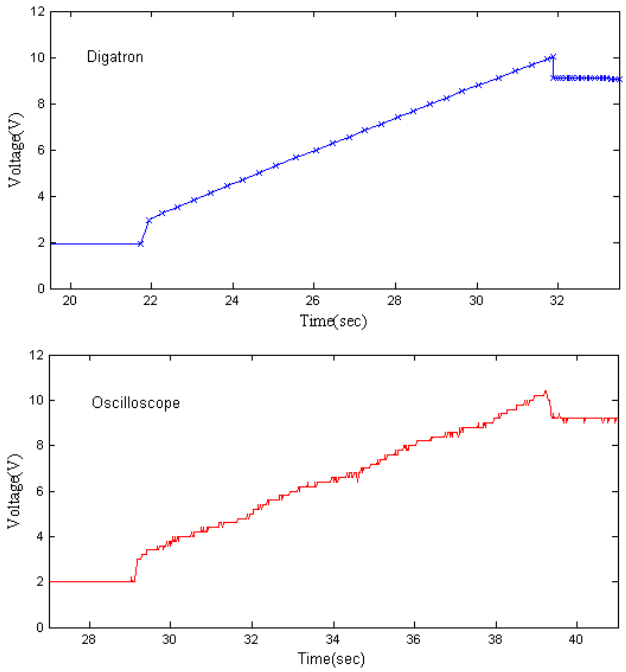

Figure 3.16: Comparison between Digatron measurement and measurement done with the oscilloscope.

The results from one parallel test is shown in figure 3.16. Using the first current interrupt as reference gives the following result:

$V_{1,digatron} = 1.931V$
$V_{2,digatron} = 2.962V$
$V_{2,digatron} - V_{1,digatron} = 1.031 \pm 0.001V$
$V_{1,osc} = 2.0V$
$V_{2,osc} = 3.0V$
$V_{2,osc} - V_{1,osc} = 1.0 \pm 0.2V$

Using the second current interrupt as reference gives:

$V_{1,digatron} = 10.020V$
$V_{2,digatron} = 9.122V$
$V_{1,digatron} - V_{2,digatron} = 0.898 \pm 0.001V$
$V_{1,osc} = 10.4V$
$V_{2,osc} = 9.2V$
$V_{1,osc} - V_{2,osc} = 1.2 \pm 0.2V$

Current interrupt At the moment the current is interrupted, there will be a sudden drop in the terminal voltage of the supercapacitor. The current supplied from the Digatron interrupts, e.g. goes from constant current to zero in the matter of ms. This step change in current results in an immediate reaction from the ohmic resistive components of the capacitor, but not from the capacitive elements, since there is a time delay defined by the specific time constant of the components. After this sudden potential drop, the capacitive components starts reacting and the voltage should ideally fall off exponentially. A principal sketch of this phenomenon can be seen in figure 3.17.

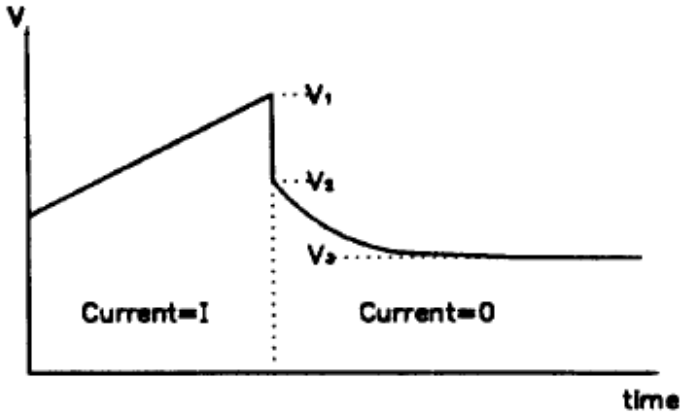

Figure 3.17: Principal sketch of a current interrupt situation with ohmic voltage drop, followed by an exponential decay[27]

Maxwell Technologies defines the ESR of the supercapacitor as the voltage drop measured over the terminals 5 time constants after current interrupt[3]. Maxwell's definition is shown in figure 3.19.

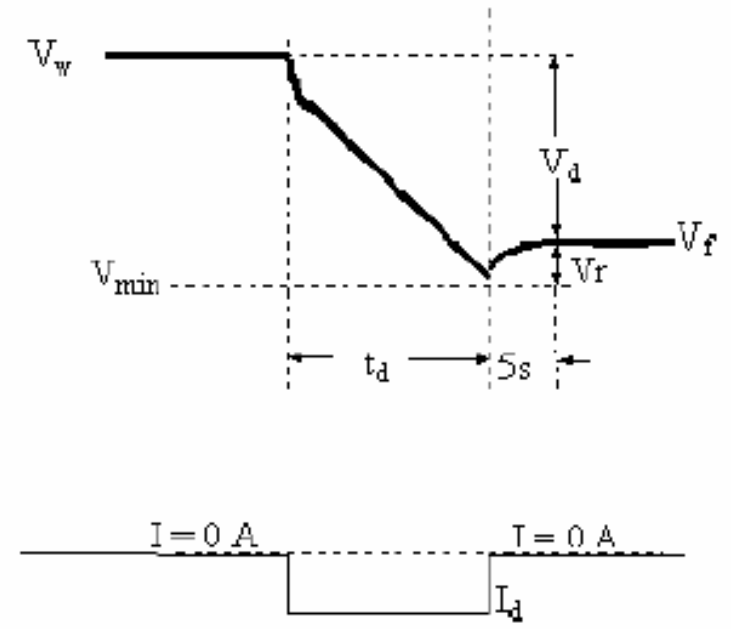

Figure 3.18: Maxwell Technologies' definition of ESR by current interrupt[3]

The ESR can thereby be calculated as follows:

$$ESR = \frac{V_f - V_{min}}{I_d} \tag{3.20}$$

Where I_d is the constant discharge current before interrupt. Zooming in on the time interval where the current interrupt happens, gives the results shown in figure 3.19 and 3.20, for 40 A and 60 A respectively.

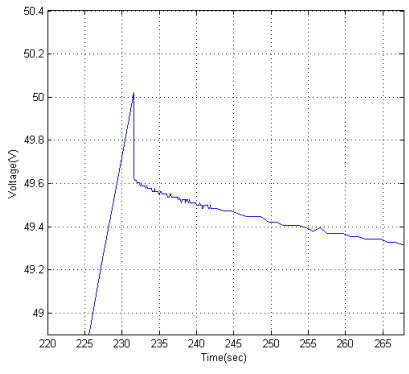

Figure 3.19: Current interrupt after charging with 40 A constant current

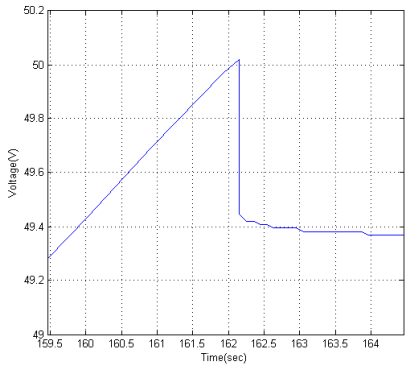

Figure 3.20: Current interrupt after charging with 60 A constant current

From the measurement data can respectively the maximum voltage and the immediate voltage drop(not Maxwell definition) be found. For 40 A current the experiment gave $V_{max} = 50,02V$ and $V_2 = 49,62V$. This gives an immediate ESR-value of:

$$ESR = \frac{50,02V - 49,62V}{40A} = 10\,m\Omega \tag{3.21}$$

For 60 A current the experiment gave $V_{max} = 50,02$ and $V_2 = 49,45V$, which gives an immediate ESR-value of:

$$ESR = \frac{50,02V - 49,45V}{60A} = 9,5\,m\Omega \tag{3.22}$$

Capacitance voltage dependency On the basis of the voltage measurements conducted at different charging currents described above, it is possible to calculate the differential capacitance $C(V)_{diff}$ for a given constant current. Using a non-linear least square method, results in an approximation of the voltage-time profie given by a cube polynomial. An example is given in figure 3.21.

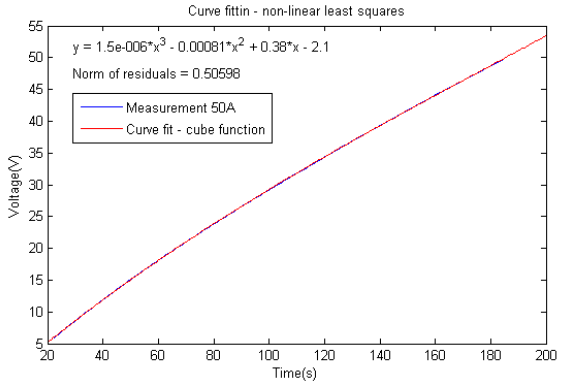

Figure 3.21: Using non-linear least squares, leads to an approximation of voltage as a function of time given by a cube function, at a specific constant charging current.

Given a constant charging current, differentiating $V(t)$ with respect to time produces $C(V)_{diff}$, according to (3.13). Conducting this procedure on all the measurements conducted at different charging currents, gives the result seen in figure 3.22 [12].

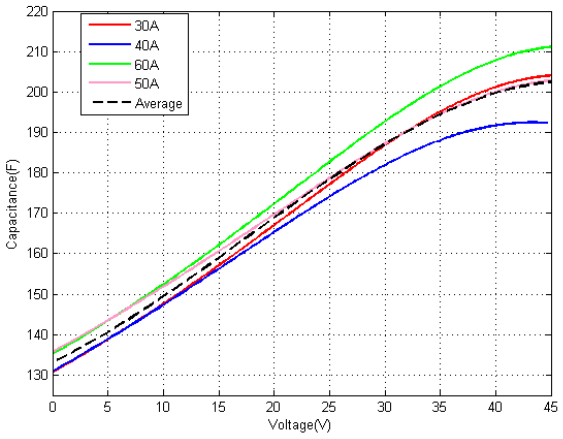

Figure 3.22: Calculated voltage dependent capacitances at different currents. The dashed black curve is the average.

[12]The method proposed by Faranda[22], that was outlined in section 3.3.2, did not produce adequate results when applied on these measurement results.

Long term open circuit voltage The supercapacitor was charged with a constant current $I_{ch} = 100A$ to approximately rated voltage. Then the open circuit voltage was measured over a wider time window of 12 hours. The results are graphically represented in figure 3.23.

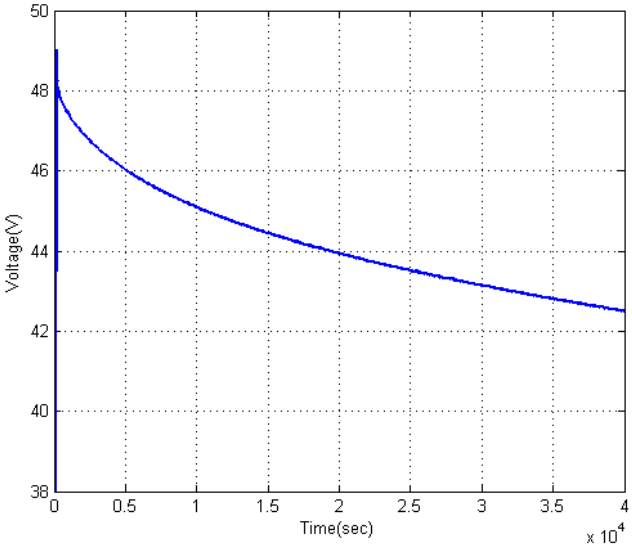

Figure 3.23: Self-discharge over a period of approximately 11 hours. Peak voltage is 49 V. After a characteristic ohmic voltage drop due to the ESR, the voltage deacays from 48,4 V.

Based on the theory on the long term behavior of open circuit voltage, [17] and [23], it is appropriate to look at characteristic behavior in specific time intervals. As suggested in [17] and [23] there is a self-discharge behavior in the first hours after established open circuit voltage approximated by equation (3.15). Conducting this analysis on the measurement data gives a result seen in figure 3.24.

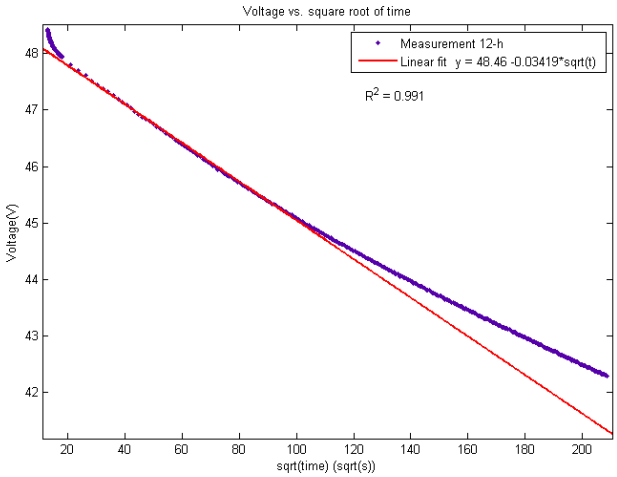

Figure 3.24: Measurement and linear fitting using least squares method from 400 seconds to 10 000 s. Open circuit voltage as a function of the square root of time.

Using a first order exponential fit on the time region from 10 000 seconds to the end of open circuit voltage around 43 500 seconds, gives a result shown in figure 3.25.

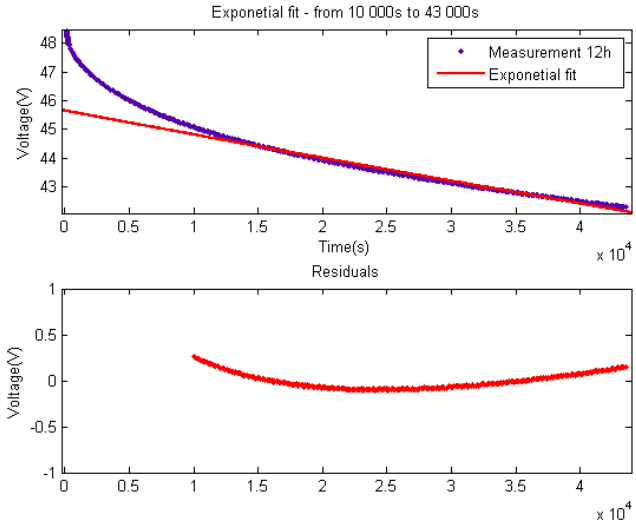

Figure 3.25: Measurement and first order exponential fitting using non-linear least squares method from 10 000 seconds to 43 500 seconds. Open circuit voltage as a function of of time.

The fitted exponential function becomes:

$$V(t) = 45.65 \cdot e^{-1.838 \cdot 10^{-6} \cdot t} \tag{3.23}$$

A closer inspection of the region from 0 to 400 seconds using second order exponetial fitting, produces the result shown in figure 3.26.

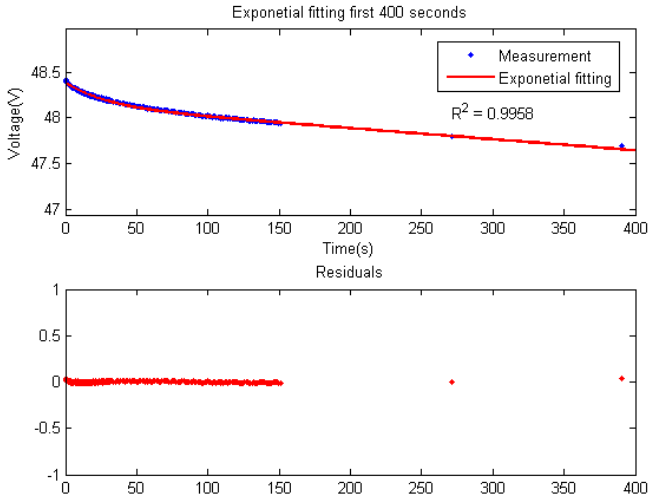

Figure 3.26: Measurement and second order exponential fitting using non-linear least squares method from 0 seconds to 400 s. Open circuit voltage as a function of of time.

The fitted second order exponential function is:

$$V(t) = 0.2528 \cdot e^{-0.03388t} + 48.13 \cdot e^{-2.529 \cdot 10^{-5} t}[V] \tag{3.24}$$

3.4.3 Discussion

Parallel test with ocilloscope Within the uncertainty limits there is a good agreement between the parallel measurements at the first current interrupt, while there is significant a higher voltage difference for the oscilloscope measurement than the Digatron at the second current interrupt. Based on the other parallel measurements conducted, it seems to be that the voltage measured with the oscilloscope deviates from the Digatron measurement with + 0.2 V. This is likely due to the long cable stretched to the Digatron, having a small ohmic resistance and inductance.

Current interrupt The value given in the data sheet from Maxwell is $7.6\,m\Omega$, but had one calculated the voltage drop after 5 time constants, would the potential drop been larger, resulting in an even higher calculated ESR-value. Based on all the measurements and accounting for the measurement deviation between Digatron and oscilloscope, the ESR-value is likely to be in the order of $10-11\,m\Omega$ which is significantly higher than the value given in the datasheet for the capacitor. This could be due to the ageing effects, since the supercapacitor is produced around year 2007.

Long term open circuit voltage From the linear approximation in figure 3.24 it can be seen that there is a adequate correspondence with the theory between 400 seconds and 10 000 seconds(2.7 h). Also in accordance with the theory one can see a deviation from this approximation after 10 000 seconds. According to the theory, this interval should be dominated by a self-discharge mechanism due to internal ohmic leakage pathways[23][17], which can be modeled as a large leakage resistance R_{leak} in parallel with the capacitor. In the time domain this mechanism can be seen as a exponential decay of capacitor voltage due to discharge through a resistor, described by equation (3.16). One can see that the time constant of the fitted exponential function in (3.23) is very large, $\tau = \frac{1}{1.838e{-}6\, s^{-1}} \approx 151 hours$.

However, there is the obvious deviation from 0 to 400 seconds, seen in figure 3.26, which is not in correspondence with the theory proposed by [17][23], but could maybe be ascribed to charge redistribution effects found in [24]. The focus of attention should be on the coefficients describing the time constants of the fitted curve. From (3.24) the first term describes the immediate behavior with a small time constant $\tau = \frac{1}{0.03388 s^{-1}} \approx 30 seconds$, while the second term describes the longer term behavior in this interval with a time constant $\tau = \frac{1}{2.529 \cdot 10^{-5} s^{-1}} \approx 11 hours$. Seeing the long term constant just as continuum of the second region from 400 seconds, the short term constant can be seen as the time constant of the immediate charge redistribution processes.

3.5 Modeling

On the basis of the measurements conducted, it is now possible to try to recreate the experimental results with simulations using an adequate equivalent circuit model. The equations and the dynamical behavior behind a more complex equivalent circuit is hard to derive by hand, which make a simulation program necessary to get fast and accurate simulations and results. In the following simulations Matlab/Simulink is used together with its additional graphic user interface(GUI) Simpower.

3.5.1 Modeling of the variable capacitance

Because Simpower does not contain a variable capacitor component, the variable capacitance in the model is created as a sub block build around a variable voltage source. The incoming current is measured, then multiplied by the inverse of the variable capacitance and then integrated over time to give the voltage output. The voltage output is fed back to a look up table where a function is defined describing the capacitance voltage dependence that was found in section 3.4.2. The output from the look up table is the capacitance at the instantaneous voltage level. The principal features of this model is recreated from [28]. The contents of the sub block can be seen in figure 3.27.

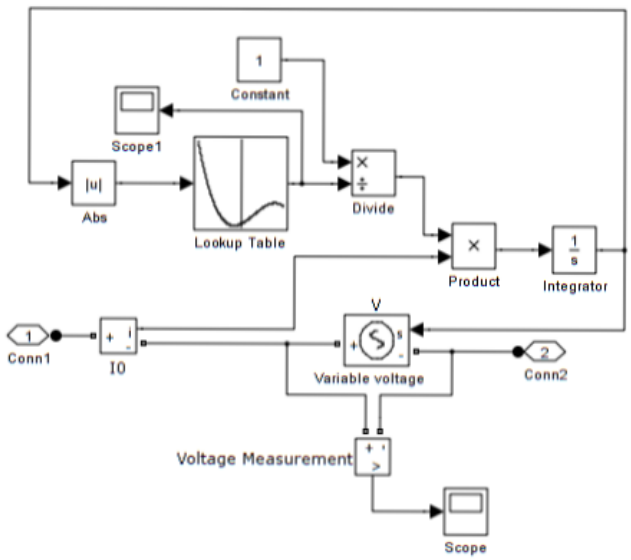

Figure 3.27: Simpower sub block defining the variable capacitance

3.5.2 The Faranda-model

The complex and rigid method of determining parameters in the Zubieta model, makes it difficult to connect the parameters to the actual measurements. Therefore, using the simplified Faranda-model gives, besides good accuracy, a satisfying correspondence with the measurements.

Parameters in the first RC-branch R_i in the branch is equivalent to the ESR-value measured at the current interrupt. On the basis of the measurements a good approximation is to set $R_i = 10\,m\Omega$. The variable capacitance is approximated using the method described in section 3.2.6. Having a obtained the function describing the capacitance as dependent on voltage at every current level, the average function can be added in the look-up table in the variable capacitance sub-block. However, the constant capacitance varies between 130 F and 140 F at different current levels, as can be seen in figure 3.22. Doing the simulations it was found that setting $C_0 = 138\,F$ at all current levels gave the best approximation.

Leakage resistance Based on the analysis of the long term open circuit voltage in section 3.4.2, it was found that the current leakage effect first begin to dominate the behavior of the voltage profile after roughly 3 hours. It was found through exponential fitting that the time constant was $\tau = \frac{1}{1.838e-6} \approx 151\,hours$. At this time the charge redistribution has ended and the two capacitances $C(V)$ and C_1 are in parallel with respect to R_{leak}.

A rough estimate of the total capacitance value of the two RC-branches at around 43 V is $C_{eff} = C(V) + C_1 \approx 200\,F + 10\,F = 210\,F$. This gives

Constant capacitance C_0	138 F
Variable capacitance	Look-up table
$\mathbf{R_i}$	$10m\Omega$
$\mathbf{C_1}$	10 F
$\mathbf{R_1}$	100Ω
$\mathbf{R_{leak}}$	$3k\Omega$

Table 3.2: Estimated parameters for the two-branch model.

$R_{leak} = \frac{\tau_{leak}}{C_{eff}} \approx 3\,k\Omega.$

Parameters in the second RC-branch One of the challenges is to find the parameters of the second RC-branch. The branch should capture the process of charge redistribution in the supercapacitor, and would first come into play when the capacitor is left at open circuit for a period of time. This is because R_1 is relatively much larger then R_i. Faranda [22] proposes a method of finding the parameters described in section 3.3.2. This method is however not robust, since it is challenging to find the time constant τ_2 for the second branch based on this method.

In theory, by using a large number of RC-branches and through detailed analysis of the open circuit voltage decay, one could estimate a large number of time constants and thus capture the charge redistribution, diffusion processes and leakage current in great detail in the model. Limiting the task to finding one time constant, must therefore be based on qualified guessing, seeking to find the parameters fitting best to the proposed model. The task is not to capture the behavior of the supercapacitor when left open circuit for a long time, but to be able to describe the immediate and intermediate transient behavior caused by charge redistribution after current interrupt.

Based on the measurements conducted at different charging current levels and using parameter estimation tools in Simulink, it was found that the most adequate values for the second branch is: $R_1 = 100\,\Omega$ and $C_1 = 10\,F$.

In the Faranda model formulated in Simpower shown in figure A.11 in Appendix A.4, the constant capacitance value C_0 has been integrated into the variable capacitance's look-up table.

3.5.3 Comparing the proposed model with measurements

In the following figures the results of the simulations with 40 A, 50 A and 100 A are presented.

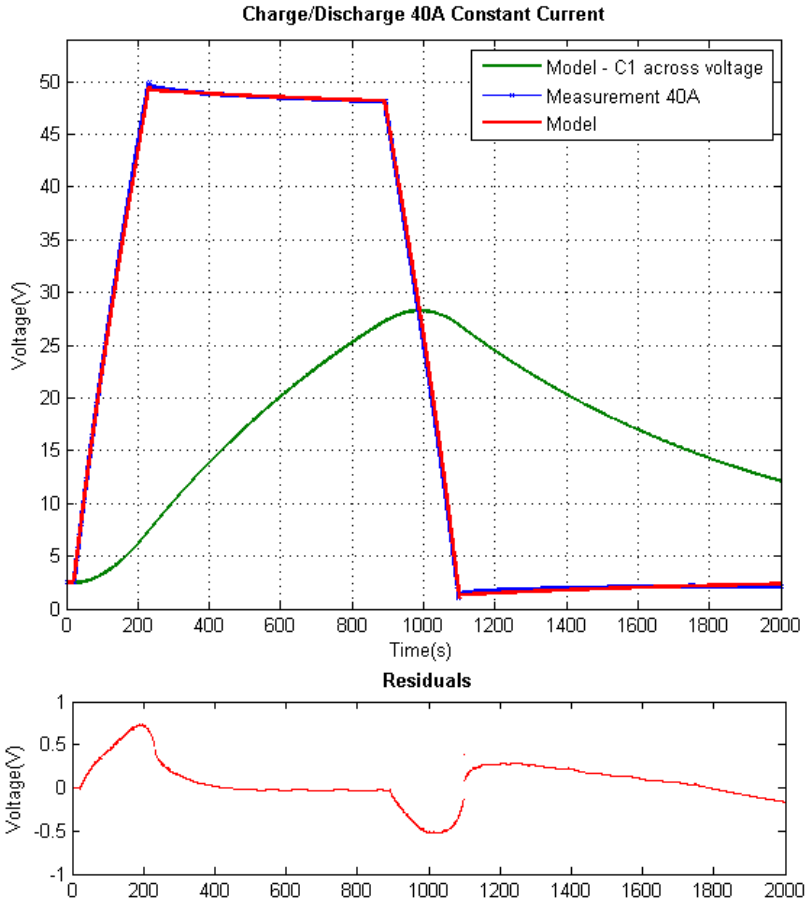

Figure 3.28: Simulation and measurements with 40A charging/discharging current. The green curve shows the profile of the voltage across C1.

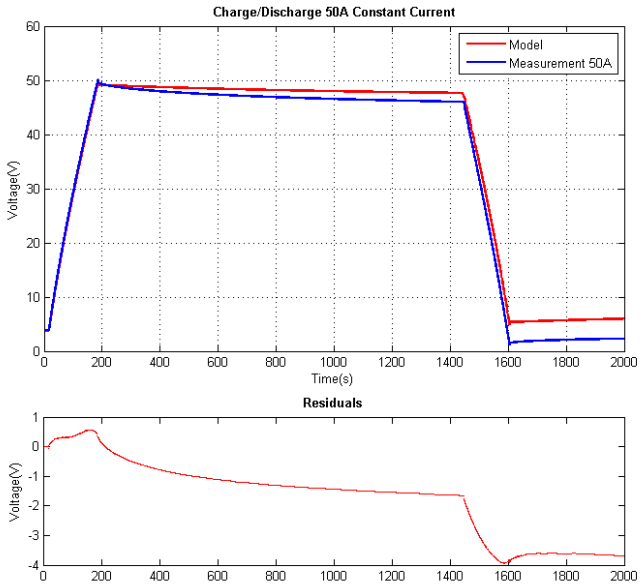

Figure 3.29: Simulation and measurements with 50A charging/discharging current

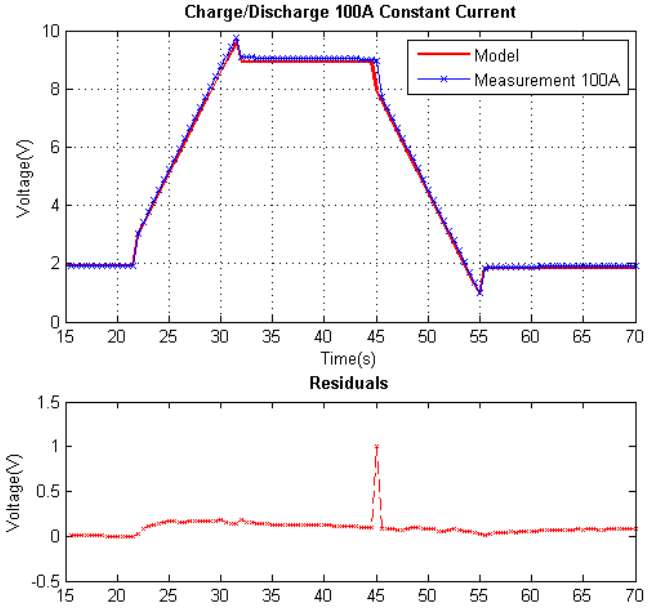

Figure 3.30: Simulation and measurements with 100A charging/discharging current up to 10 V

A closer inspection of the current interrupt and transient behavior at 60A charging current can be seen in figure 3.31.

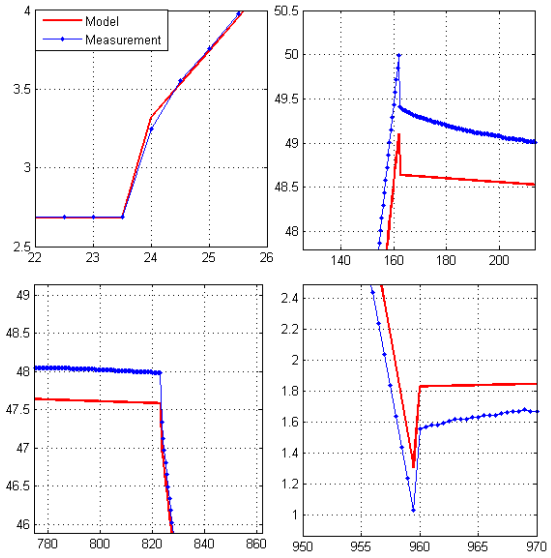

Figure 3.31: Zooming in on the transients at current interrupt

The sensitivity of the model when changing the parameters R_1 and C_1 respectfully, are presented in figure 3.32 and figure 3.33.

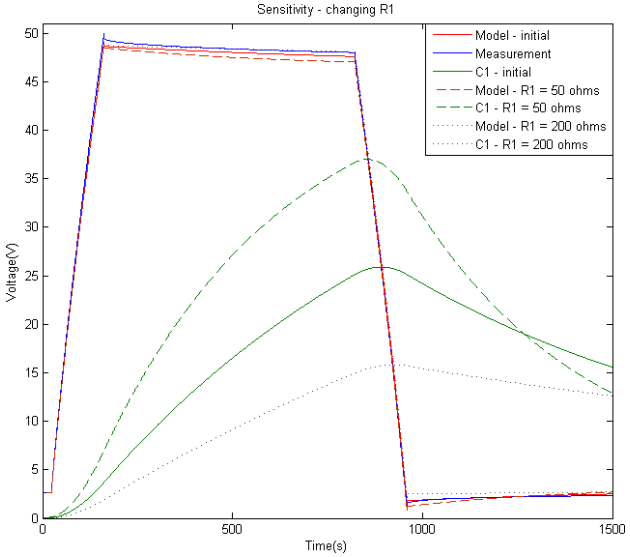

Figure 3.32: Simulation and measurements(60A) with different values of R1, holding the other parameters constant

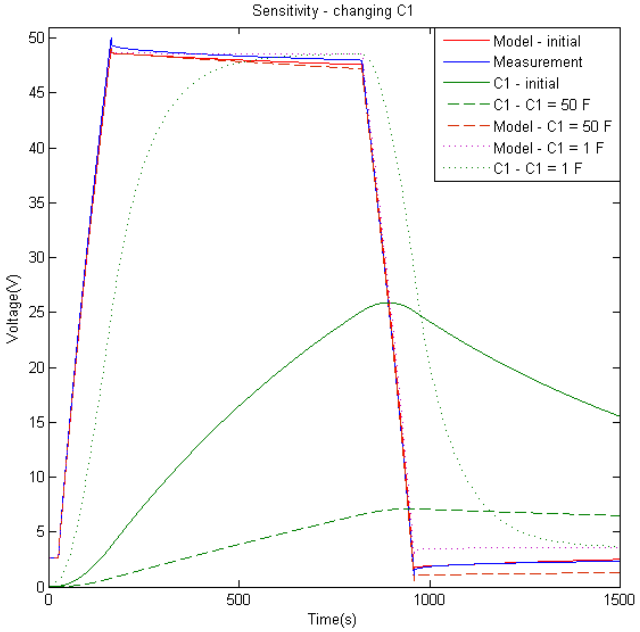

Figure 3.33: Simulation and measurements(60A) with different values of C1, holding the other parameters constant

3.5.4 Discussion

The results of the simulations conducted shows a good correspondence between the proposed model and the measurements. However, at 50 A charging/discharging current one can see larger deviation between the model and the measurement. Especially the transient behavior after the second current interrupt is overestimated by the model, which accumulates into larger errors as the time goes by. This region is dominated by the behavior of the second branch, and tuning in the parameters $R_1 = 70\,\Omega$ and $C_1 = 75\,F$, give near to optimal fit. The large deviation could be explained by the fact that the open circuit time is twice as long for the 50A-measurement as for the other, beacuse the same deviation can be seen in the case of 30 A.

But using the same second branch values on the other current levels, results in a even larger deviation. Nothing in the literature on the models points towards a current dependency, but as one saw in section 3.2.3 the current is non-linear dependent on the voltage, when pseudocapacitance effects are present. This may be a part of the explanation for the deviations observed.

The closer inspection in figure 3.31 shows the difficulty in capturing the transient behavior of the capacitor voltage after current interrupt. The obvious decrease in the voltage at current interrupt after charging, points towards an immediate charge redistribution effect which is impossible to capture with only two RC-branches. The same effect can be seen at current interrupt after discharging, but here is the charge redistribution reversed and the voltage increases

Rated capacitance	130 F
ESR(DC)	8,1 mΩ
Rated Voltage	56 V
Energy density(max)	3,1 Wh/kg
Stored Energy	56,6 Wh
Power density(dc)(max)	2 600 W/kg
Maximum peak current(1 sec)	1 800 A
Leakage Current(max)	N/A
Thermal Resistance	0,50 °C /W
Cycle life	1 000 000 cycles
Mass module	18 kg

Table 3.3: Product specifications for BMOD0130 P056 [30].

for a period of time. This is in accordance with the theory described in section 3.2.7.

3.5.5 New supercapacitor

The REHYS-system has a DC-bus voltage that varies with the state of charge of the battery. When the battery is fully charged, the DC-bus voltage could reach 54-55 V. The supercapacitor(BMOD00165) available in the laboratory, has a rated voltage(48V) that is below the maximum operating voltage of the system. Hence, connecting this supercapacitor directly to the DC-bus without a converter interface, imply that the supercapacitor would have to operate above its rated voltage, which could severely damage it.

Therefore, it was decided that a supercapacitor with a higher rated voltage was needed. A BMOD0130 P056 from Maxwell Technologies with a rated voltage of 56 V and rated capacitance of 130 F was found to be sufficient. The physical design is similar to that of BMOD00165. However, BMOD0130 is specially designed for UPS-applications[13] providing short term backup power for graceful shutdown of systems, for ride through of power transients and for transitions to a permanent backup power supply. The power rating of the module is for discharge up to 15 seconds[29]. BMOD00165 has a broader operation range and could be used in hybrid vehicle and telecommunication applications with more frequently charge and discharge operation[20]. Since Maxwell Tech. does not have Bootscap-modules with rated voltages above 48 V, the BMOD0130 was the only realizable alternative.

The BMOD0130 consists twenty-three individual cells[14] connected in series with passive voltage management circuitry. The product specifications of the module can be seen in table 3.3.

The module has been electrically characterized and modeled according to the method described in section 3.4 and 3.5. The estimated parameters of the two-branch Faranda-model can be seen in table 3.4.

The variable capacitance used in the look-up table can be found in Appendix A.3. We observe that this model has a lower internal resistance R_i(ESR) than

[13] Uninterpretable Power Supply
[14] BCAP3000P270(3000 F, 2,7 VDC).

Constant capacitance C_0	100 F
Variable capacitance	Look-up table
$\mathbf{R_i}$	$5,8m\Omega$
$\mathbf{C_1}$	12 F
$\mathbf{R_1}$	80Ω
$\mathbf{R_{leak}}$	$2k\Omega$

Table 3.4: Estimated parameters for the two-branch model.

the former, which probably is due to the fact that it is a newer model with updated technological improvements and that it has had a significant shorter shelf time than BMOD00165. This is a significant improvement when hybridizing it with the battery. As we shall see in the following section, the internal resistance plays an important role in the load sharing between battery and supercapacitor. We also observe that BMOD0130 has a lower leakage resistance than BMOD00165, which means that this supercapacitor experiences a higher self-discharge-rate then BMOD00165.

4 Passive Hybrid System

In this section we will consider the *passive hybrid topology*, connecting the supercapacitor in parallel with the battery and the load. In order to get a hold of the behavior of the PHS and to quantify the performance characteristics, it is necessary to conduct a detailed analysis of the system's electrical properties. Beginning with a simplified equivalent circuit, it is possible to derive the important electrical quantities, and from this derive useful performance factors. This enable us to compare the PHS with a battery-alone system [15][16].

4.1 Analytic approach

4.1.1 Equivalent circuit and system equations

For the sake of simplicity, the supercapacitor is only represented by a single lumped constant capacitance, C, and an internal lumped resistance, R_c(ESR). Similarly, the battery is represented by as a constant voltage source, V_b, together with an internal resistance, R_b. The equivalent circuit of the direct connection can be seen to the left in figure 4.1.

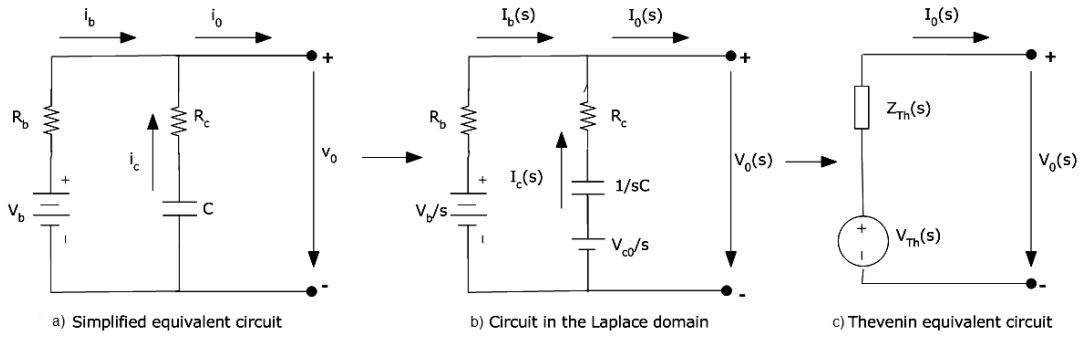

Figure 4.1: a) Equivalent circuit of direct parallel connection. b) Circuit transformed into the frequency domain. c) Thevenin equivalent circuit.

In the analysis it is convenient to transform the circuit into the frequency domain using the Laplace transform. The transformed circuit is shown in figure 4.1b). Generally, the current i_c flowing through a capacitor, can be transformed into the Laplace domain given an intial capacitor voltage V_{c0}:

$$i_c = C\frac{dv_c}{dt} \rightarrow I_c(s) = sCV_s - CV_{c0} \rightarrow V(s) = \frac{I(s)}{sC} + \frac{V_{s0}}{s} \tag{4.1}$$

That is, a charged capacitor with non-zero initial conditions can in the Laplace domain be replaced by an uncharged capacitor in series with a step-function voltage source with amplitude V_{c0}.

In the Laplace domain the currents and voltages of the battery and the supercapacitor can be found using Kirchoff's voltage and current rules:

[15]The following is based upon an analysis conducted in [31] and in [32].
[16]In the following, BMOD0130 P056 will be used.

$$I_c(s) + I_b(s) = I_0(s) \tag{4.2}$$

$$V_0(s) = \frac{V_{c0}}{s} + I_c(s)R_c + I_c(s)\frac{1}{sC} = \frac{V_b}{s} + I_b(s)R_b \tag{4.3}$$

In order to describe the output load voltage, v_0, in terms of the circuit elements, the Thevenin-equivalent circuit should be derived. The output circuit voltage in the Laplace domain, $V_0(s)$, can be found by analyzing the circuit in open circuit condition. Then the current $I(s) = I_c(s) = I_b(s)$ circulates in a closed loop so that according to figure 4.1b):

$$\frac{V_b(s)}{s} - I(s)R_b - I(s)R_c - I\frac{1}{sC} - \frac{V_{c0}}{s} = 0$$

$$I(s) = \frac{V_b - V_{c0}}{(R_b + R_c + \frac{1}{sC})s} \tag{4.4}$$

Then, the Thevenin equivalent voltage, $V_{Th}(s)$, can be obtain:

$$V_{Th}(s) = \frac{V_{c0}}{s} + I(s)R_c + I(s)\frac{1}{sC} \tag{4.5}$$

Substituting (4.4) into (4.5) gives:

$$V_{Th}(s) = \frac{V_b - V_{c0}}{(R_b + R_c + \frac{1}{sC})s}(R_c + \frac{1}{sC}) + \frac{V_{c0}}{s} \tag{4.6}$$

which can be simplified to:

$$V_{Th}(s) = V_b\frac{R_c}{R_b + R_c}\frac{s+\alpha}{s(s+\beta)} + V_{c0}\frac{R_b}{R_b + R_c}\frac{1}{s+\beta} \tag{4.7}$$

where $\alpha = \frac{1}{R_cC}$ and $\beta = \frac{1}{(R_b+R_c)C}$. The Thevenin equivalent impedance can be found by short-circuiting the voltage sources:

$$Z_{Th}(s) = (R_c + \frac{1}{sC}) \parallel R_b = \frac{(R_c + \frac{1}{sC})R_b}{R_c + R_b + \frac{1}{sC}} = \frac{R_cR_b}{R_b + R_c}\frac{s+\alpha}{s+\beta} \tag{4.8}$$

Now it is possible to transform $V_{Th}(s)$ back into the time domain, $v_{Th}(t) = \mathscr{L}^{-1}\{V_{Th}(s)\}$. Using partial fraction expansion, the first term of (4.7) yields:

$$V_b\frac{R_c}{R_b + R_c}\frac{s+\alpha}{s(s+\beta)} = \frac{A}{s} + \frac{B}{s+\beta}$$

where

$$A = V_b \; and \; B = \frac{R_c}{R_b + R_c}V_b - V_b$$

which in the time domain becomes:

$$V_b + \frac{R_c}{R_b + R_c}V_be^{-\beta t} - V_be^{-\beta t}$$

The second term in the time domain is simply given by:

$$\frac{R_b}{R_b + R_c}V_{c0}e^{-\beta t}$$

This leads to:

$$v_{Th}(t) = V_b + [\frac{R_c}{R_b + R_c} V_b - V_b + \frac{R_b}{R_b + R_c} V_{c0}] e^{-\beta t} = V_b + \frac{R_b}{R_b + R_c} [V_{c0} - V_b] e^{-\beta t} \tag{4.9}$$

Having obtained the Thevenin equivalent circuit, it is now possible to connect a load to the circuit as shown in figure 4.2.

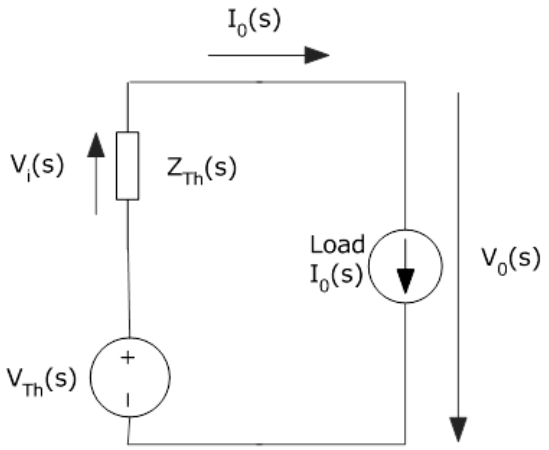

Figure 4.2: Thevenin equivalent circuit with connected load $I_0(s)$.

A real load $I_0(s)$ could be of any form. However, many power systems possess common load profile characteristics, described by relatively peak-to-average power requirements. Such loads can be represented by pulse train profiles, where the load suddenly changes from one level to the other with a given frequency and duty cycle[9]. As an analytical approach, an ideal pulsed square load is convenient, since this simplifies the analysis and enable us to capture the fundamental characteristics and behavior of a power system. The pulsed load current with period T and pulse duty ratio D can for the first N pulses be expressed as:

$$i_0(t) = I_0 \cdot \sum_{k=0}^{N-1} [\Phi(t - kT) - \Phi(t - (k + D)T)] \tag{4.10}$$

Here is I_0 the amplitude of the current and $\Phi(t)$ the unshifted unit step function. In the Laplace domain this becomes:

$$I_0(s) = I_0 \cdot \sum_{k=0}^{N-1} [\frac{e^{-kT \cdot s}}{s} - \frac{e^{-(k+D)T \cdot s}}{s}] \tag{4.11}$$

The average value of the load current is simply the amplitude of the load current multiplied with the duty ratio, $I_L = DI_0$.

For the given load form, the internal voltage drop $V_i(s)$ is given by:

$$V_i(s) = Z_{Th} I_0(s)$$

After preforming an inverse Laplace transform[17] we obtain:

$$v_i(t) = R_b I_0 \sum_{k=0}^{N-1} \{(1 - \frac{R_b}{R_b + R_c}(e^{-\beta(t-kT)}) \cdot \Phi(t - kT) \\ -(1 - \frac{R_b}{R_b + R_c} e^{-\beta(t-(k+D)T)}) \cdot \Phi(t - (k + D)T)\} \tag{4.12}$$

From figure 4.2 we can see that the output voltage is given by: $V_0(s) = V_{Th}(s) - V_i(s)$, which in the time domain becomes:

$$v_0(t) = v_{Th}(t) - v_i(t) \tag{4.13}$$

Further, the currents of the battery and the supercapacitor are obtained using $v_0(t)$:

$$i_b(t) = \frac{1}{R_b}[V_b - v_0(t)] \tag{4.14}$$

$$i_c(t) = i_0(t) - i_b(t) \tag{4.15}$$

4.1.2 Performance in steady-state

The hybrid system reaches steady state when the supercapacitor voltage is equal to the battery voltage, $V_{0c} = V_b$. Combining (4.13) with (4.14) and setting $V_{0c} = V_b$, gives the battery current under steady state condition:

$$i_{b,ss}(t) = I_0 \sum_{k=0}^{N-1} \{(1 - \frac{R_b}{R_b + R_c}(e^{-\beta(t-kT)}) \cdot \Phi(t - kT) \\ -(1 - \frac{R_b}{R_b + R_c} e^{-\beta(t-(k+D)T)}) \cdot \Phi(t - (k + D)T)\} \tag{4.16}$$

Combining (4.15) with (4.10) and (4.16) we obtain:

$$i_{c,ss}(t) = \frac{R_b I_0}{R_b + R_c} \sum_{k=0}^{N-1} \{e^{-\beta(t-kT)} \cdot \Phi(t - kT) - e^{-\beta(t-(k+D)T)} \cdot \Phi(t - (k + D)T)\} \tag{4.17}$$

Looking at the first applied load pulse when $k = 0$, one can see from equation (4.16) that at the time the pulse load is applied at $t = 0$, the battery current jumps to a value $i_{b,ss}(0) = I_0 - \frac{R_b I_0}{R_b + R_c}$. When the pulse load current has a constant non-zero value, $i_{b,ss}(t)$ increases with a rate determined by the time-constant $\tau = 1/\beta = (R_b + R_c)C$. The battery is being discharged. When the load current suddenly drops to zero again at time $t = DT$, $i_{b,ss}$ falls back from it's final load value to a value equal to $i_{b,ss}(DT) = I_0 - \frac{R_b I_0}{R_b + R_c} e^{-\beta(DT)} - (I_0 - \frac{R_b I_0}{R_b + R_c})$. From this initial value the current falls off exponentially, again with a rate determined by the time-constant $\tau = 1/\beta$.

For the capacitor current it is the other way around. From (4.17) we see that at the time the first pulse load is applied, $i_{c,ss}$ jumps to an initial value equal to $i_{c,ss}(0) = \frac{R_b I_0}{R_b + R_c}$. Thereafter it falls off exponentially. The supercapacitor

[17] For a detailed derivation, see Appendix A.2

is being discharged. When the load suddenly drops to zero, $i_{c,ss}$ fall off to a value $i_{c,ss}(DT) = \frac{R_b I_0}{R_b+R_c} e^{-\beta(DT)} - \frac{R_b I_0}{R_b}$. The polarity of $i_{c,ss}$ changes and the supercapacitor is being charged by the decaying battery current.

Plotting these analytical expressions over two square pulses with duty ratio $D = 0,1$ and period $T = 10\,s$, results in the plot shown in 4.3. The electrical parameters are chosen close to those found in the real system in the laboratory: $R_b = 0,05\,\Omega$, $R_c = 5,8\,m\Omega$, $C = 130\,F$. The load current is normalized.

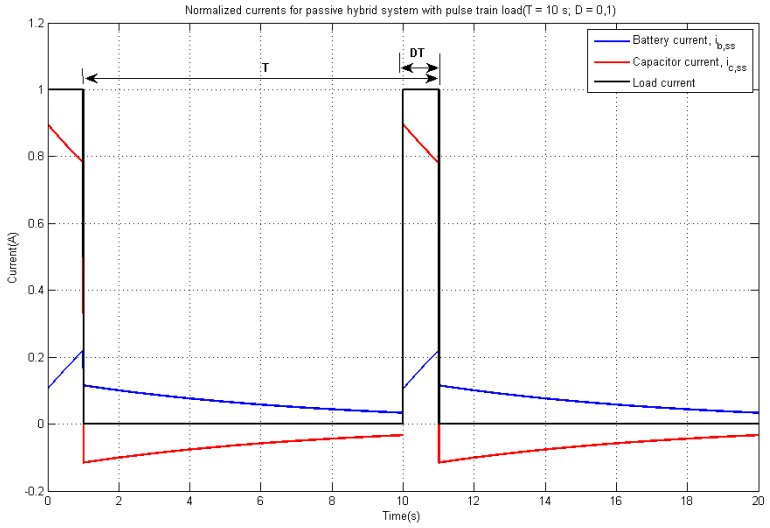

Figure 4.3: Plot of the steady state battery current $i_{b,ss}$ and capacitor current $i_{c,ss}$ in reaction to a pulsed load with amplitude $I_0 = 1A$, duty ratio $D = 0,1$ and period $T = 10s$.

We see that the initial load sharing is solely determined by the relationship between the internal resistances of the battery, R_b, and the supercapacitor, R_c. The smaller the capacitor resistance compared with the battery resistance, the more of the immediate power demand is covered by the supercapacitor. The larger the capacitance, C, of the supercapacitor, the longer time it can supply the load close to it's initial share, but also the longer time it takes to recharge it. The supercapacitor is relieving the battery of large fluctuations in the current. Without the supercapacitor, the battery would have to meet the load by itself.

4.1.3 System eigen-frequency

The system has a *nominal eigen-frequency* defined by $f_{eigen} = 1/\tau = \beta$. Using electrical parameters close to those found in our system, the system nominal eigen-frequency is defined as:

$$f_{eigen} = \frac{1}{C(R_b + R_c)} = \frac{1}{C(R_b + R_c)} = \frac{1}{130F(0.05\Omega + 5,8m\Omega}) = 0,138Hz \tag{4.18}$$

which is equal to a nominal time period of $T_{eigen} = 1/f_{eigen} = 7,3\,seconds$, which is the *time constant* of the system.

Because of the variable capacitance of the supercapacitor[18], the eigen-frequency will vary with the terminal voltage of the supercapacitor.

4.1.4 Power enhancement factor

From (4.16) it is obvious that the maximum battery current occurs at the end of the pulse load, i.e. at $t = (k + D)T$. However, the peak battery current at the $n'te$ pulse depends on all the proceeding terms. When $n \to \infty$, it can be shown that the peak battery current becomes:

$$I_{b,peak} = I_0\{1 - \frac{R_b}{R_b + R_c}\frac{e^{-\beta DT}(1 - e^{-\beta(1-D)T})}{1 - e^{-\beta T}}\} = I_0(1 - \zeta_c) = \frac{I_0}{\gamma} \quad (4.19)$$

Here is ζ_c the capacitor *current sharing factor* at the peak value:

$$\zeta_c = \frac{R_b}{R_b + R_c}\frac{e^{-\beta DT}(1 - e^{-\beta(1-D)T})}{1 - e^{-\beta T}} \quad (4.20)$$

γ is here defined as the *power enhancement factor*. That is, without a supercapacitor, $\zeta_c = 0$, $\gamma = 1$ and $I_{b,peak} = I_0$; the battery would have to meet the load by itself. The hybrid system can thus supply a higher load current than the battery-alone system. If I_{rated} is the rated current for the battery, reformulating (4.19), the new possible load current of the hybrid system can be expressed as:

$$I_0 = \gamma \cdot I_{rated} \quad (4.21)$$

and the instantaneous peak power at rated power of the battery becomes:

$$P_{peak} = I_0 V_b = \gamma \cdot I_{rated} V_b = \gamma \cdot P_{rated} \quad (4.22)$$

The power enhancement factor is larger than one when the supercapacitor is connected to the system. Thus, the factor descibes the extra power that can be supplied by the hybrid system compared to a battery-alone system. From (4.19) it can also be seen that γ depends on the frequency, $f = 1/T$, and the duty cycle of the pulsed load profile. Computing γ as a function of the duty cycle at different frequencies as multiples of f_{eigen} for our system, results in the plot shown in figure 4.4.

[18] See appendix A.3.

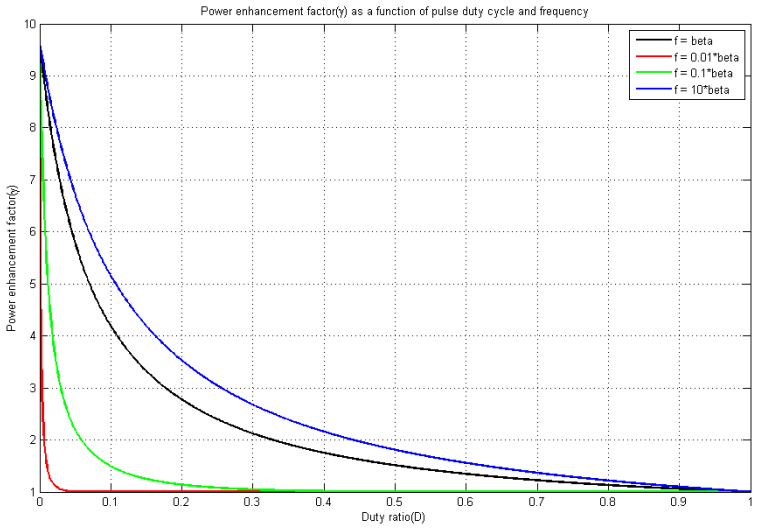

Figure 4.4: The power enhancement factor γ as a function of pulse duty ratio and frequency.

From figure 4.4 it can be seen that as the frequency of the pulse load becomes very low and approaches DC, the power enhancement factor decreases towards unity for all duty ratios. As the frequency becomes much higher than the eigen-frequency, the power enhancement factor cannot be increased further and reaches a limit close to that of $f = 10 \cdot f_{eigen}$. For all frequencies the power enhancement factor is at its maximum in the limit when $D \to 0$. From (4.19) the limit for our system becomes: $\lim_{D\to 0} \gamma = \frac{R_b+R_c}{R_c} = 9,6$. That is, the maximum theoretical possible enhancement of output power could be increased 9,6 times the output power of the battery-alone system. Given the same load conditions, decreasing the system eigen-frequency by increasing the capacitance of the supercapacitor, gives a higher ζ_c and γ - hence, the supercapacitor covers a larger share of the load current. Again, it is obvious that the smaller the internal resistance of the supercapacitor, the better the hybrid system performance. Therefore, connecting supercapacitor cells in parallel reduces the internal resistance and is advantageous in optimizing the system's power performance, but, this again reduces the operating voltage of the supercapacitor bank and thus its operation range.

4.1.5 Losses and power saving

Because the supercapacitor has a much smaller internal resistance than the battery, the power losses are reduced, since a significant share of the output current is covered by the supercapacitor. Considering the battery system, the average power of the load pulse train with amplitude, V_0, and duty cycle, D, applied over a load resistance, R, is equal to:

$$P_{0,average} = \frac{V_0^2}{R} \cdot D = \frac{V_{0,rms}^2}{R} \tag{4.23}$$

Accordingly, the root mean square load current, $I_{0,rms}$, becomes:

$$I_{0,rms} = I_0\sqrt{D} \tag{4.24}$$

Here the battery would meet the load by itself, thus $I_{0,rms} = I_{b,rms}$. The total instantaneous power drawn from the battery and transferred to the load is then the active power, $P_{0,b}$, minus the internal power losses, P_i, due to the internal resistance of the battery:

$$P_b = V_b I_{0,rms} - R_b I_{0,rms}^2 = V_b\sqrt{D}I_0 - R_b D I_0^2 = V_b\sqrt{D}I_0(1 - \frac{R_b\sqrt{D}I_0}{V_b}) \tag{4.25}$$

The output voltage of the battery $V_{b,out}$ is the internal voltage, V_b, minus the voltage drop across the resistance, R_b; thus $V_{b,out} = V_b(1 - \frac{R_b\sqrt{D}I_0}{V_b})$ and (4.25) becomes:

$$P_b = V_{b,out} I_{0,rms} \tag{4.26}$$

and the internal power loss is given as:

$$P_{i,b} = R_b I_{0,rms}^2 \tag{4.27}$$

In order to calculate the internal power losses in the hybrid system, it is necessary to derive the root mean square values for the battery and supercapacitor currents when connected together. This is a lengthy exercise and will not be conducted here[19]. It can be shown that the root mean square value of the battery current is equal to:

$$I_{b,rms} = \sqrt{\frac{1}{T}\int_{nT}^{(n+1)T} [i_{b,ss,nth}]^2\, dt} = \sqrt{D}I_0\lambda(D,T) \tag{4.28}$$

where $\lambda(D,T)$ is a factor depending on the duty cycle and the period of the pulsed load. [20]

The root mean value of the supercapacitor current can be expressed as:

$$I_{c,rms} = \sqrt{\frac{1}{T}\int_{nT}^{(n+1)T} [i_{c,ss,nth}]^2\, dt} = \sqrt{D}I_0\mu(D,T) \tag{4.29}$$

where $\mu(D,T)$ is a factor depending on the duty cycle and the period of the pulsed load. [21]

The total internal power loss of the hybrid system can then be expressed as:

$$P_{i,hybrid} = R_b I_{b,rms}^2 + R_c I_{c,rms}^2 = R_b D I_0^2(\lambda^2 + \frac{R_c}{R_b}\mu^2) = R_b D I_0^2(1-\varepsilon) \tag{4.30}$$

ε can take on values between zero and 1, and is called the *power saving factor*. It is defined as $\varepsilon = 1 - (\lambda^2 + \frac{R_c}{R_b}\mu^2)$.

[19] For details see Dougal et.al. [31]

[20] $\lambda = \sqrt{1 + \frac{R_b}{R_b+R_c}\frac{2(1-e^{-\beta DT})}{\beta DT}(\frac{1-e^{\beta DT}}{1-e^{\beta T}} - 1) + (\frac{R_b}{R_b+R_c})^2\frac{(e^{\beta DT}-1)(1-e^{\beta(1-D)T})}{\beta DT(1-e^{\beta T})}}$

[21] $\mu = \sqrt{(\frac{R_b}{R_b+R_c})^2[\frac{1}{\beta DT}\frac{e^{\beta DT}-e^{\beta T}-1+e^{\beta(1-D)T}}{1-e^{\beta T}}]}$

Computing ε as a function of the duty cycle at different frequencies as multiples of f_{eigen} for our system, results in the plot shown in figure 4.5.

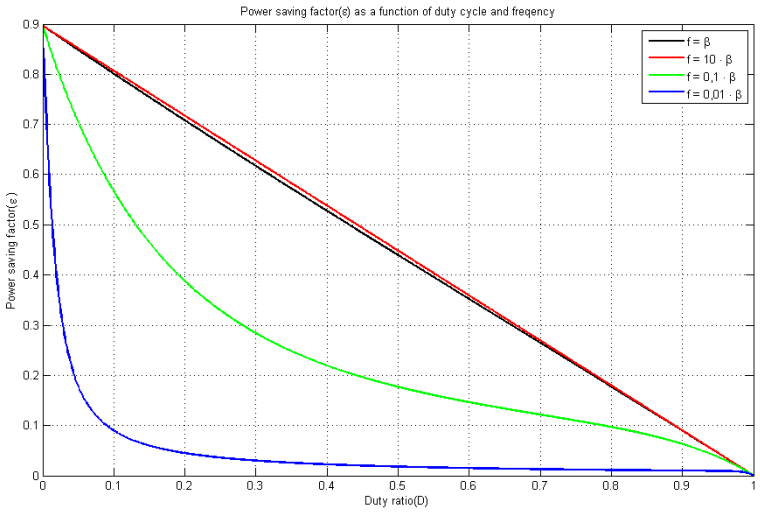

Figure 4.5: Power saving factor ε as a function of pulse duty ratio and frequency.

From figure 4.5 we see that the power saving factor at all frequencies approaches the same limit as $D \to 0$. It can be shown, through a limit analysis of $\lambda(D,T)$ and $\mu(D,T)$, that: $\lim_{D\to 0} \varepsilon = \frac{R_b}{R_c+R_b}$. This is the optimal theoretical power saving that could be achieved.

Substituting (4.27) into (4.30) yields:

$$\varepsilon = \frac{P_{i,b} - P_{i,hybrid}}{P_{i,b}} \tag{4.31}$$

Thus, it is clear that ε is the fraction of the power normally lost in a battery system that is saved by hybridizing the system. The ideal, though unrealizable, state is when ε is unity and no power is dissipated in the hybrid system.

4.1.6 Run time extension

If τ_b is the total run time of a battery-alone system [22] and τ_{hybrid} is the total run time of the hybrid system, then the total energy saved with the hybrid system is equal to:

$$\Delta W = W_{i,b} - W_{i,hybrid} = R_b D I_0^2 \tau_b - R_b D I_0^2 (1-\varepsilon)\tau_{hybrid} \tag{4.32}$$

The saved energy can also be formulated as:

$$\Delta W = P_0 \Delta\tau \tag{4.33}$$

[22] It is here assumed that the battery can be run to 100% depth of discharge.

where P_0 is the output power from the system and $\Delta\tau = \tau_{hybrid} - \tau_b$ is the extended run time of the system due to the reduced losses. The output energy of the hybrid system can also be expressed as:

$$W_0 = P_0\tau_{hybrid} = W_{total} - W_{i,hybrid} = V_b\sqrt{D}I_0\tau_b - R_bDI_0^2(1-\varepsilon)\tau_{hybrid} \quad (4.34)$$

Combining (4.32) and (4.34) in (4.33) yields finally:

$$\frac{\Delta\tau}{\tau_b} = \frac{\varepsilon\delta\sqrt{D}}{1-\varepsilon\delta\sqrt{D}} \quad (4.35)$$

(4.35) is the fractional increase of the run time for the hybrid system compared to the battery-alone system. We see that there is three variables that influence the discharge time of the battery: the power saving factor, the duty ratio of the pulse load, and the fractional voltage drop across the internal resistance to the battery internal voltage, $\delta = \frac{R_bI_0}{V_b}$. When the fractional voltage drop is zero, i.e. $R_b = 0$, the time extended becomes zero, because there is no dissipation in the battery and thus no power to be saved. The larger the load current, the larger is the dissipation and δ. The fractional run time increase has then two independent variables, δ and D, since ε is dependent on D and T. For our system a load current amplitude equal to $I_0 = 40\,A$, gives a peak power output $P_0 = V_bI_0 = 48\,V \cdot 40\,A = 1,92\,kW$. That is close the rated power for the system, namely $2kW$. This gives $\delta = \frac{40A \cdot 0{,}05\Omega}{48V} = 0,04$. However, the power peaks could reach five times the rated level, which yields $\delta = \frac{200\,A \cdot 0{,}05\Omega}{48\,V} = 0,21$. Computing $\frac{\Delta\tau}{\tau_b}$ as a function of pulse duty cycle and frequency with the two different values of δ, results in the plot shown in figure 4.6.

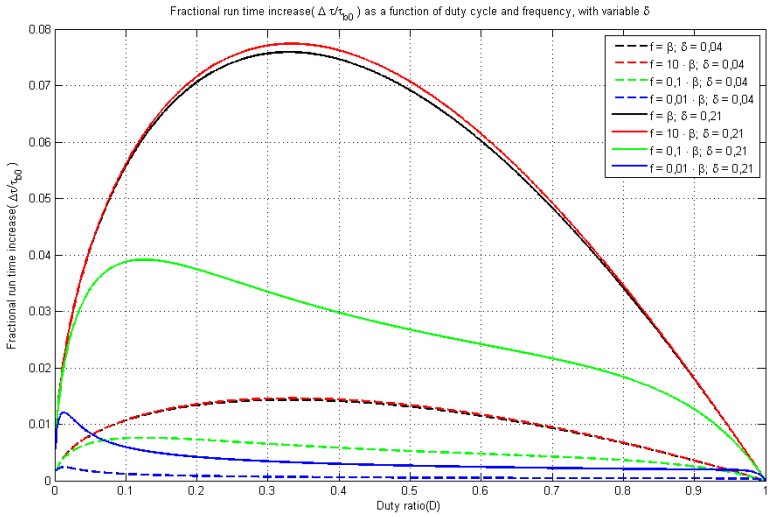

Figure 4.6: Fractional run time extention as a function of pulse duty ratio and frequency, with $\delta = 0,04$ and $\delta = 0,2$ respectively.

We observe that the higher the fractional fractional voltage drop across the internal resistance to the battery internal voltage, δ, the higher is the fractional

run time increase. For all frequencies the *run time increase* becomes zero when $D \to 0$. However, the *power saving factor* and the *power enhancement factor* had a maximum when $D \to 0$. The obvious physical reason for this is that the system is not utilized when the load current is zero. Although the *power sharing* reaches its optimum, no *energy* is supplied to the load and, thus, the run time cannot be increased. The *run time increase* also becomes zero when $D \to 1$. This is close to DC and the supercapacitor will not be utilized at all. We see that the value of D for *maximum run time increase* is depending on the frequency of the pulse load. As the frequency becomes lower, the value of D_{max} is reduced.

It is not possible to control the power flow in and out of the supercapacitor since its terminal voltage is forced to be equal to the battery voltage at all time. Current division between the battery and the supercapacitor is determined solely by the two branch internal impedances, R_b and R_c.

In the succeeding experiment of the passive hybrid, we are going to use a load current amplitude of $I_0 = 12A$. This gives $\delta = 0,0125$. The fractional run time increase with this load current can be seen in figure 4.7.

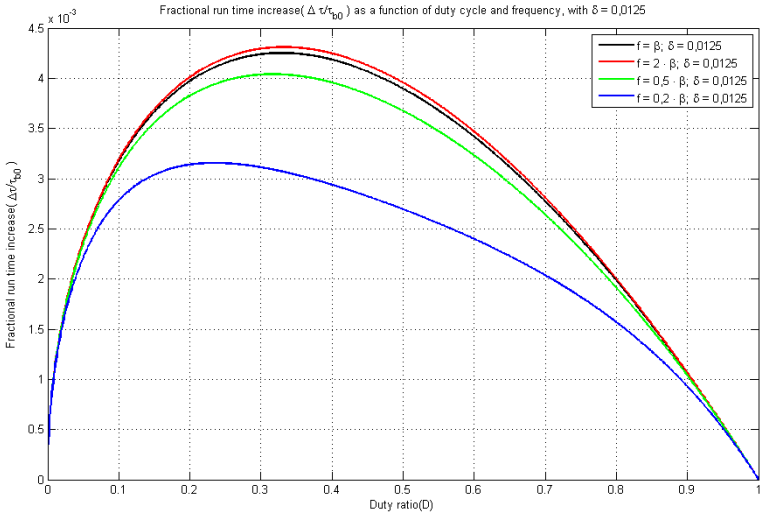

Figure 4.7: Fractional run time extention as a function of pulse duty ratio and frequency, with $I_0 = 12A$ and $\delta = 0,0125$.

We can observe that at this load current amplitude, it is little to be gained in run time increase by hybridization. At optimal frequency and optimal duty ratio the fractional run time increase is only about 4,5 per mil: an insignificant increase.

4.1.7 System voltage profile

When applying a pulse train load, the system voltage of the passive hybrid shows a characteristic behavior that can be divided into four different types of voltage drops and gains, shown in figure 4.8.

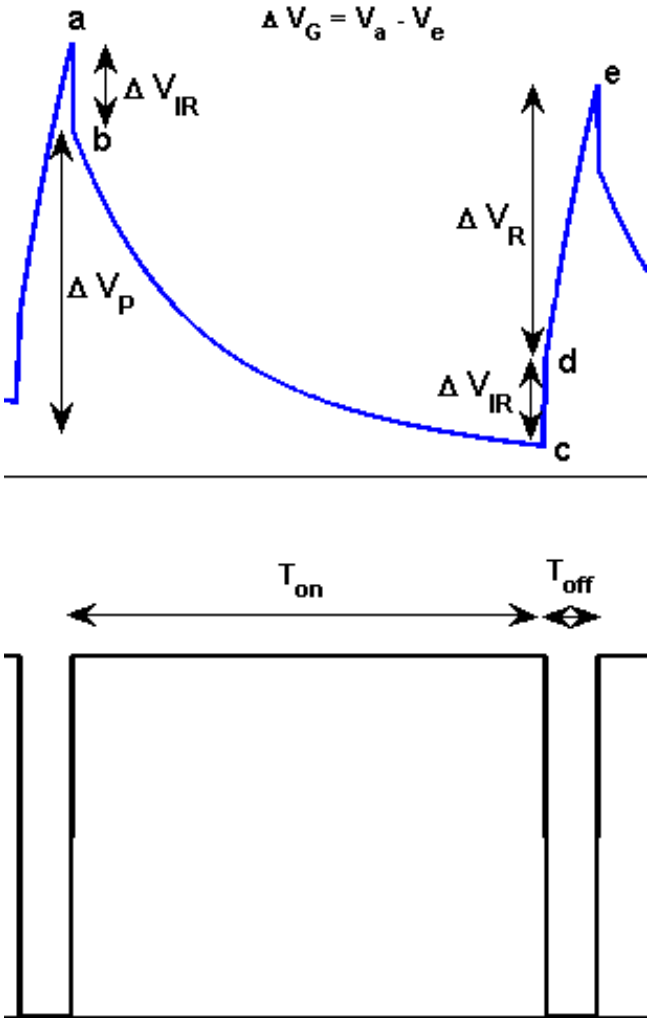

Figure 4.8: A typical voltage profile for a passive hybrid system responding to a pulse train load.

The initial voltage drop, ΔV_{IR}, that can be observed in the moment the pulse is applied, is similar to the characteristics of current interrupt discussed in section 3.4.2. The voltage drop originates from the internal resistances of the system, which immediately respond to the step change in current. This is followed by a so called polarization drop, ΔV_p, which occurs in both the battery and supercapacitor[33]. The polarization voltage drop in the supercapacitor is mainly due to charge redistribution effects discussed in section 3.2.7.

In the moment the current is interrupted and drops to zero, the ΔV_{IR} is yet again observed as a voltage gain, followed by a relaxation gain, ΔV_R, when the load current is zero. For both the PHS and the BAS, the polarization voltage drop as well as the relaxation gain shows an exponential behavior.

The difference between the initial potential at the moment the voltage was

Nominal Voltage	48 V
Rated Capacity	230 Ah
Maximum Capacity	239,6 Ah
Fully Charged Voltage	52,3 V
Nominal Discharge Current	46 A
Internal Resistance	0,05 Ω
Capacity at Nominal Voltage	71,4 Ah

Table 4.1: Electric characteristics of the lead acid battery model

applied, V_a, and the regained potential, V_e, at the end of the relaxation period, T_{off}, can be defined as the regain potential drop ΔV_g[33]. This drop is due to the fact that as the system discharges, the state of charge of the battery and supercapacitor is decreasing, leading to an overall deacay in the system voltage.

4.2 Modeling and simulations

4.2.1 Modeling

In order to study the performance of the passive hybrid system and to verify the analytical approach above, simulations in Matlab/Simulink is conducted using Simpower GUI. The supercapacitor model formulated in section 3.5 is used together with a ready-made generic dynamic battery model in Simpower. The battery model is parameterized to represent most popular types of rechargeable batteries. Implementing the block in our model and choosing the lead acid battery, we predefine the internal resistance to $R_b = 0,05\,\Omega$, rated capacity to $Q = 230\,Ah$ and nominal voltage to $V_{nom} = 48\,V$. This gives the electrical properties listed in table 4.1.

A constant variable current source is used as load. Connecting a pulse train signal to its control input, produces a pulse train current with predefined duty-ratio and frequency[23].

4.2.2 Simulations: Comparison of battery-alone system and passive hybrid system

First, we want to verify that the analytical approach presented above indeed is adequate. We apply the standardized pulse train load and simulate the system performance under varying load conditions. The load variables are the amplitude I_0, the period, T, and the duty ratio, D.

The PHS was simulated with a pulse train load over 200 seconds, and in figure 4.9 a plot of the system currents can be seen, covering a time window of $20\,seconds$.

[23]In order to simulate the system over longer time periods, the capacity of the system is downscaled with a factor K. That is, both the battery $Ah-capacity$ and the capacitance of the supercapacitor is divided through the factor K. If, for example, the real simulation time is $40s$, and we want to simulate the system performance over 10 minutes(modified simulation time), the capacity of the system is divided by $K = 600s/40s = 15$. All other system parameters are left unchanged.

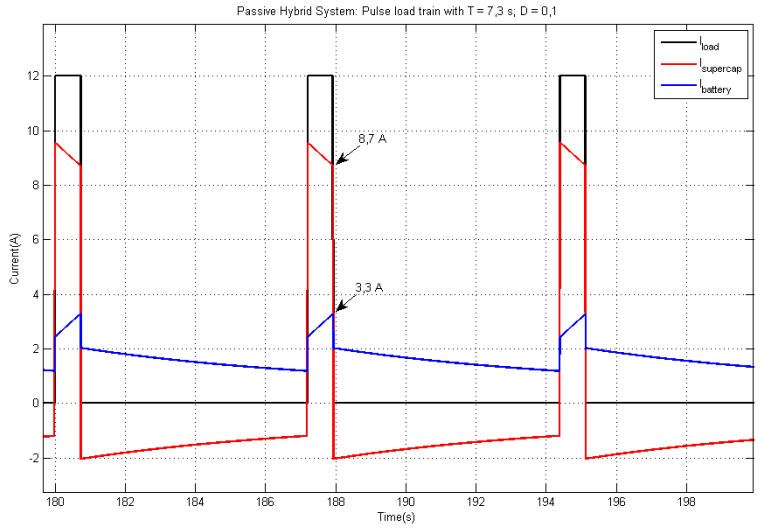

Figure 4.9: Simulation of the PHS with pulse train load; $I_0 = 12A$, $T = 7,3s$, $D = 0,1$. System currents as a function of time.

In figure 4.10 a plot of the system voltages over a period with steady state operation mode can be seen.

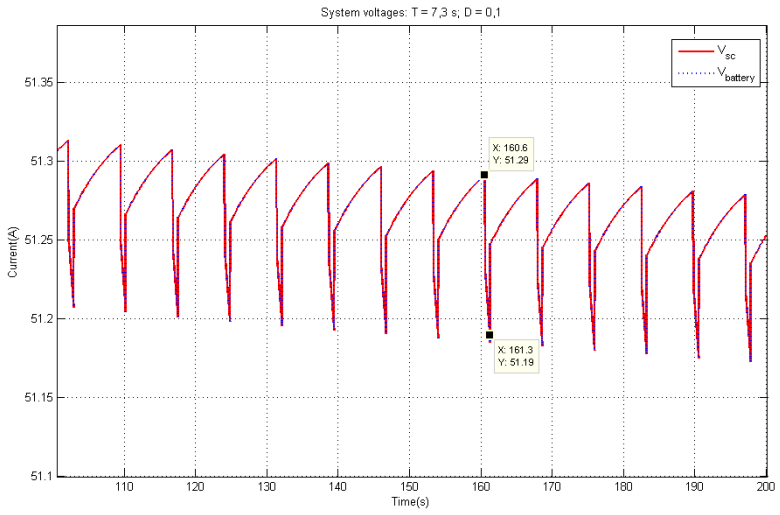

Figure 4.10: Simulation of the PHS with pulse train load; $I_0 = 12A$, $T = 10s$, $D = 0,1$. System voltages as a function of time.

As expected, the supercapacitor voltage follows the same trajectory as the battery voltage during the whole simulation period. By detailed inspection we

observe the characteristic profile discussed in section 4.1.7. After the pulse is applied, the voltage drops with ΔV_{IR}, followed by a polarization drop, ΔV_P. During the pulse off time, the ΔV_{IR}-drop is succeeded by the relaxation gain, ΔV_G.

In figure 4.11 we see the result of a simulation over the same time window with a battery-alone system.

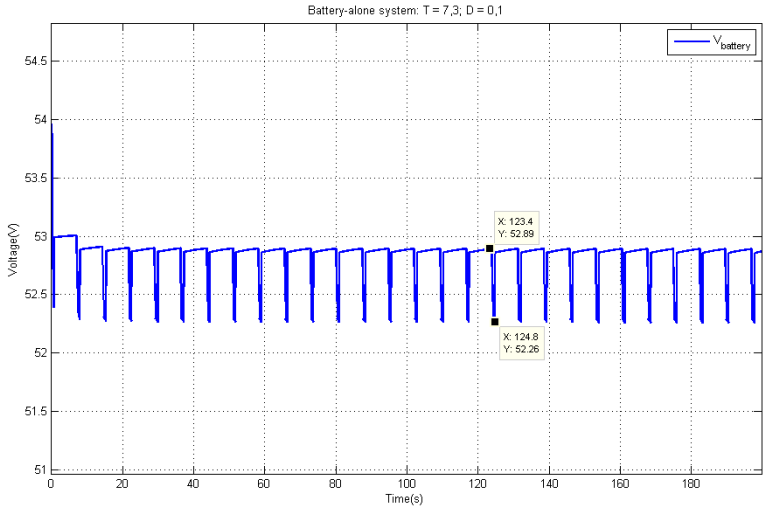

Figure 4.11: Simulation of the BAS with pulse train load; $I_0 = 12A$, $T = 10s$, $D = 0,1$. Battery terminal voltage as a function of time.

Also for the BAS we see a polarization voltage drop and gain, but this is much smaller due to the relatively much larger time-constant of the battery polarization mechanism. Comparing figures 4.10 and 4.11, we clearly see that the voltage ripple is significantly higher for the BAS than for the PHS. The BAS produces a ripple in the order of $\Delta V = 0,63\,V$, while the PHS reduces the voltage ripple to approximately $\Delta V = 0,10\,V$ in steady state operation - a reduction of over 80%. This clearly shows one of the main advantages of hybridization, namely, reducing fast and large transients in the battery terminal voltage.

Because the operating voltage of the battery is higher than the nominal voltage of the supercapacitor, the modeled variable capacitance of the supercapacitor produces a significant higher capacitance value than its rated capacitance. The result is a reduction of the system eigen-frequency, which means that the supercapacitor covers a larger share of the load current. From figure 3.22 we see that the capacitance is around $C = 143F$ at this voltage level[24]. The new eigen-frequency of the system at this voltage level now becomes:

$$\beta = \frac{1}{C(R_b + R_c)} = \frac{1}{143F(0,05\Omega + 5,8m\Omega)} = 0,125Hz(\rightarrow T \approx 8,0s)$$

[24]See Appendix A.3

Using (4.20) this gives analytically a *capacitor current sharing factor* in the order of:

$$\zeta_c = \frac{0,05\Omega}{0,05\Omega + 5,8m\Omega} \frac{e^{-0,125Hz \cdot 0,1 \cdot 7,3s}(1 - e^{-0,125Hz(1-0,1)7,3s})}{1 - e^{-0,125Hz \cdot 10s}} = 0,765$$

According to the theory, the battery current should satisfy (4.19) at the end of one pulse in steady state. Calculating $I_{b,peak}$, using the sharing factor, yields:

$$I_{b,peak} = I_0(1 - \zeta_c) = 12A(1 - 0,765) = 2.8A \tag{4.36}$$

and

$$I_c = \zeta_c \cdot I_0 = 0,765 \cdot 12A = 9,2A \tag{4.37}$$

From figure 4.9 we graphically find the values $I_{b,peak} = 3,7A$ and $I_c = 8,7A$. The simulated current sharing factor is thus $\zeta_c = 0,725$, which is a deviation of about 5 % from the calculated current sharing factor. This deviation could be explained by the fact that the two-branch supercapacitor model used, is more complex than the simplified equivalent circuit used applied in the analytical approach, which is also the case for the generic Simpower-battery model used in the simulation. On that basis, there is in this case a satisfying correspondence between the simulation results and the analytical approach.

Reducing the period to half of the eigen-frequency, $T = 3,7\,s$, all other parameters left unchanged, results in the plot shown in figure 4.12, covering a time window of 20 seconds.

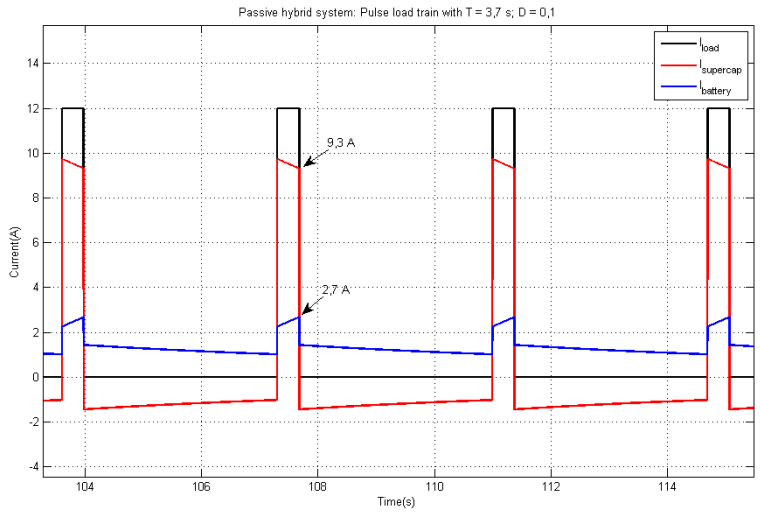

Figure 4.12: Simulation of the PHS with pulse train load; $I_0 = 12A$, $T = 3,7s$, $D = 0,1$. System currents as a function of time.

Graphically we see that the *capacitor current sharing factor* has increased to $\zeta_c = \frac{9,7A}{12A} = 0,81$. The capacitor is thus more utilized when increasing the pulse

frequency. Using the same procedure as above we find analytically $\zeta_c = 0,79$. The simulation current sharing factor is now only deviating about 3 % from the analytically calculated value.

The voltage ripple of the PHS is now $\Delta V = 0,09V$, which is a reduction of 10 % compared with a pulse period of 7,3 seconds. The voltage profile in steady state operation mode can be seen in figure 4.13.

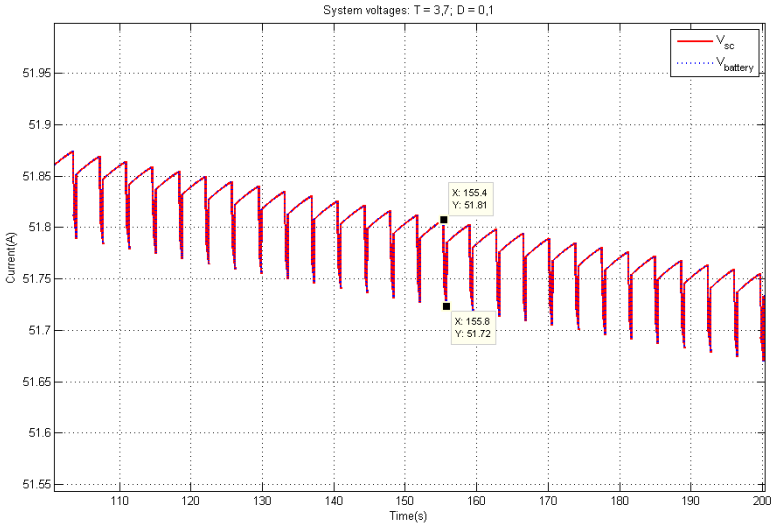

Figure 4.13: Simulation of the BAS and the PHS with pulse train load; $I_0 = 12A$, $T = 3,7s$, $D = 0,1$. Voltage as a function of time.

The voltage ripple of the battery-alone system is the same as that for T = 7,3 seconds.

By increasing the load current amplitude, the reduction in the voltage ripple of the PHS when increasing the pulse frequency becomes more significant. In accordance with the analytical approach above, it is clear that the larger the frequency of the pulse load train, and the smaller the pulse width, the more the supercapacitor is utilized, relieving the battery of large voltage fluctuations and reducing the maximum battery current.

4.3 Experiments

In order to verify the analysis above and validate our established model, experiments with the passive hybrid topology and a battery-alone system was conducted in the REHYS-laboratory. The equipment used was as follows:

- Hall current sensors: HAL200-S LEM
- LabView system design platform from National Instruments with CompactRIO real time controller.
- DC Electronic Load: PLZ 603W, Kikusui Electronics Corp.

- 4 Lead Acid battery-modules connected in series, each with a rated capacity of 230 Ah and a nominal voltage of 12 V.

The measurement data obtained through the LabView interface was stored on the CompactRIO with a measurement frequency of 10 Hz. That is one measurement point each 0,1 second.

The supercapacitor was first connected to the DC-bus through a longer cobber cable(10 meters). It became apparent that the length of the cable had a significant influence on the system behavior, manifested in severe inductance effects and a considerable ohmic voltage drop across the cable.

Additionally, the supercap was first connected to the DC-bus via a smaller contactor(25 A rated). After switching to shorter cables, a significant inductance effect and additional ohmic resistance could still be observed. Thereafter, using the same cables, the supercap was reconnected via a larger contactor with a higher current rating containing additional connection cables having almost twice the cross-sectional area as the former set-up. The result was a considerable improvement in system performance as the resistance and the inductance of the cables and contactors was significantly smaller in the new set-up.

In the following we will first discuss the challenges in regard to the experimental set up, with emphasis on additional system ohmic resistances and inductance effects. Thereafter, the experimental results when applying a pulse load train at different frequencies and duty cycles will be presented. Both the PHS and the BAS are tested under the same load conditions and compared by primarily examining the voltage profile of the two systems. In order to validate and calibrate the established model, the real passive hybrid system is compared with system simulations. Finally, the obtained results are analyzed and discussed.

4.3.1 System parasitic resistance and inductance effects

System parasitic resistance The cables and circuitry between the DC-bus connection and the point of measurement of the battery voltage and the supercapacitor voltage leads to a deviation between the system voltages. This is due to small additional ohmic resistances between the measurement points.

It can be observed a voltage difference between the battery voltage, the DC-bus voltage and the supercapacitor voltage, where the supercapacitor voltage generally is lower than the battery voltage and the DC-bus voltage is lower than both the branch voltages. The explanation for this, is that the voltage measurement is conducted at the input of the contactors, prior to the common DC-bus. In the direct parallel connection the branch voltages should be equal at all times when applying the pulsed load. A simplified equivalent circuit of the set-up, including the parasitic resistances, is shown in figure 4.14.

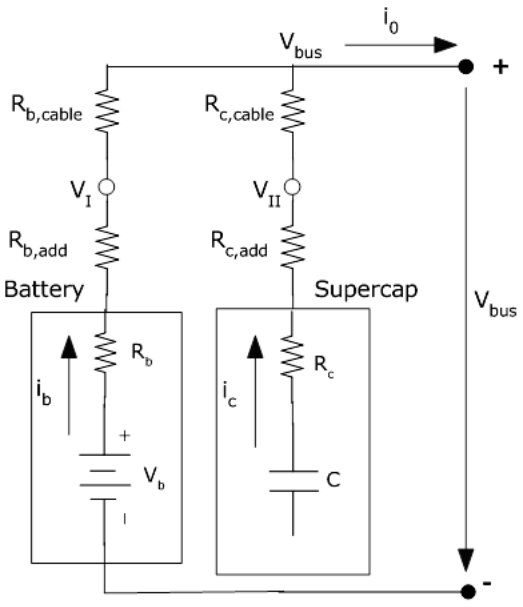

Figure 4.14: A simplified equivalent circuit showing the location of the voltage measurements.

Here is $V_I = V_{batt}$ the point of measurement of the terminal battery voltage, and $V_{II} = V_{sc}$ the point of measurement of the supercapacitor voltage. The resistances of the cables and contactors between the devices and the measurement point is represented as the lumped resistances $R_{b,add}$ and $R_{c,add}$, respectively. The relative small resistance of the cables between the measurement point and the measurement point of the DC-bus voltage, are represented as the lumped resistances $R_{b,cable}$ and $R_{c,cable}$. The measured battery potential V_I is thus equal to: $V_I = i_b R_{b,cable} + V_{bus}$; and the measured supercapacitor potential is given by: $V_{II} = i_c R_{b,cable} + V_{bus}$.

The difference between the measured battery and supercapacitor voltage is therefore a consequence of the currents flowing through each branch and of the unknown ohmic resistances of the cables and circuitry: the sum of the voltages in one branch will at all times add up to be equal to the common DC-bus voltage, V_{bus}.

Hence, the ohmic voltage drop ΔV_{IR} of the DC-bus voltage, contains information about the resistances in the two branches. By measuring ΔV_{IR}, the Thevenin equivalent resistance is equal to:

$$R_{eq} = \frac{\Delta V_{IR}}{I_0} = \frac{(R_b + R_{b,add} + R_{b,cable})(R_c + R_{c,add} + R_{c,cable})}{R_b + R_{b,add} + R_{b,cable} + R_c + R_{c,add} + R_{c,cable}} \tag{4.38}$$

when both the battery and supercapacitor is connected to the DC-bus. I_0 is the load current. When only one branch is connected to the load, the equivalent resistance is the sum of the resistances of the connected branch.

When attempting to reproduce the measurement results through simulations, there is challenges in finding the correct total ohmic resistances in each branch of the real system. First of all, the internal resistance of the battery

varies with the state of charge of the battery. The internal resistance used in the calculations above, $R_b = 0,05\Omega$, is thus the internal ohmic resistance at 90 % state of charge, and it increases as the state of charge is reduced. The internal resistance of the supercapacitor is nevertheless independent of the state of charge of the supercapacitor and can be assumed constant: $R_c = 5,8\,m\Omega$.

Disconnecting the supercapacitor from the system and running the battery alone against a known load, I_0, we can estimate the total ohmic resistance of the battery branch by inspecting the profile of the DC-bus voltage. The current interrupt technique described in section 3.4.2, can be used to find the immediate ohmic voltage drop ΔV_{IR} where the total ohmic resistance of the battery branch is equal to:

$$R_{battery,total} = \frac{\Delta V_{IR}}{I_0} \tag{4.39}$$

The state of charge of the battery at the moment of measurement is around 80 %. Taking the average value of ΔV_{IR} of several measurements at current interrupt gives:

$$R_{battery,total} \approx \frac{0,43V}{12A} = 0,036\Omega \tag{4.40}$$

To our surprise the total ohmic resistance in the battery branch is lower than the previous measured internal resistance at 90% state of charge. When calibrating the model according to the measurement, it becomes obvious that this value is to low and that an additional resistance is needed in order to achieve a satisfying match between the experimental results and the simulations. By analyzing the time constant of the system it is possible to estimate the combined additional resistance R_{add} through the relation $\tau = C(R_b + R_c + R_{add})$, if we take R_c and C as given, and using $R_b = 0,036\,m\Omega$ estimated above. The time constant can thus be used as a guide line for estimating the total additional resistance of the real system. Once we have the total additional resistance, we can distribute it in the branches of the model until it matches the measurements adequately.

Inductance effect The supercapacitor was first connected to the DC-bus using a longer cobber cable(10 meters). It became apparent that the length of the cable had a significant influence on the system behavior, manifested through inductance effects and an ohmic voltage drop across the cable. A result from one of the tests with load amplitude $I_0 = 6A$, pulse period $T = 20s$ and duty cycle $D = 25\%$ can be seen in figure 4.15.

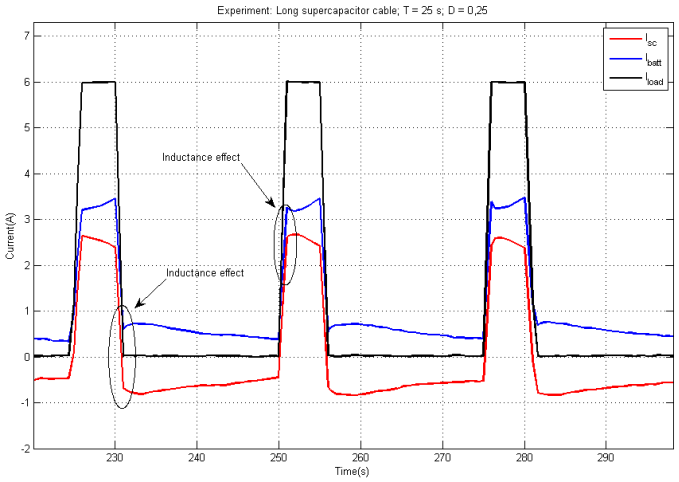

Figure 4.15: Experiment with long connection cable between supercapacitor and DC-bus. T = 25 s, D = 0,2, $I_0 = 6A$.

It is clear that the unexpected shapes of the battery and supercapacitor current profiles, is caused by an inductance and additional resistance somewhere in the system. This can be confirmed through simulations. The combined results of simulations of the ideal passive hybrid and an inductive/resistive hybrid system can be seen in figure 4.16. In the inductive/resistive system, a cable with an additional inductance and an ohmic resistance has been added in series with the supercapacitor branch.

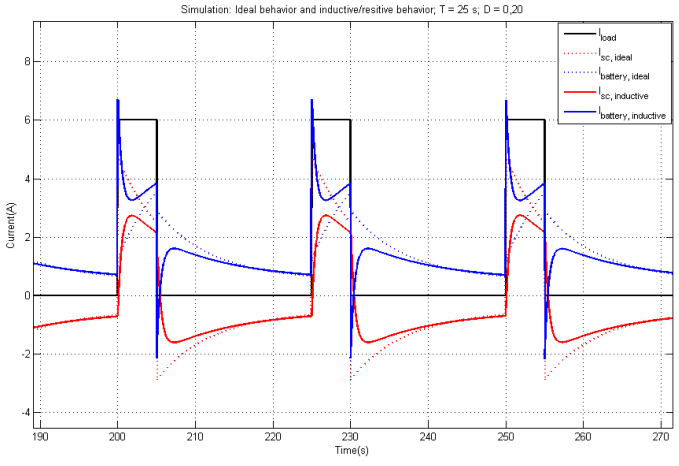

Figure 4.16: Results of simulations with the ideal system and a system with an inductive/resisitve cable connection between the supercapacitor and the DC-bus. T = 25 s, D = 0,2, $I_0 = 6A$.

In the simulation the inductive effect results in a large transient in the battery current at the moment the pulse is applied. This can not be observed in the measurements, but this could be due to the measurement time step of 0,1 seconds. Reducing the time step could maybe have revealed the transient. We also observe that the discharging current of the battery and the charging current of supercapacitor during the off-period, is smaller in the experiment than in the simulation. However, the shape and trajectories of the curves are similar. The inductive effect causes a delay in the supercapacitor reaction to the step change in load, which means that the remaining load current must be covered by the battery. For shorter duty cycles at smaller frequencies of the pulse train load, this results in a convex trajectory for the battery current and a concave trajectory for the supercapacitor current, which is the opposite of what is expected from an ideal system. The inductive effect is caused by the step change in current which results in an instantaneous opposing voltage according to Faraday's law: $V_{ind} = -L\frac{dI}{dt}$. Where the inductance, L, influence the immediate current sharing after the applied pulse, the resistance of the cable simply is added to the internal resistance of the supercapacitor, resulting in a reduced *current sharing factor*, ζ_c. Combined, these effects significantly reduce the contribution from the supercapacitor, thus reducing the efficiency of the hybrid system.

We clearly see the importance of reducing the length of the connection cables and of reducing the inductance and resistance of contactors and conductors. It is especially important regarding the supercapacitor, which function is to relieve the battery for immediate transients by a step change in the load.

4.3.2 Measurements and results

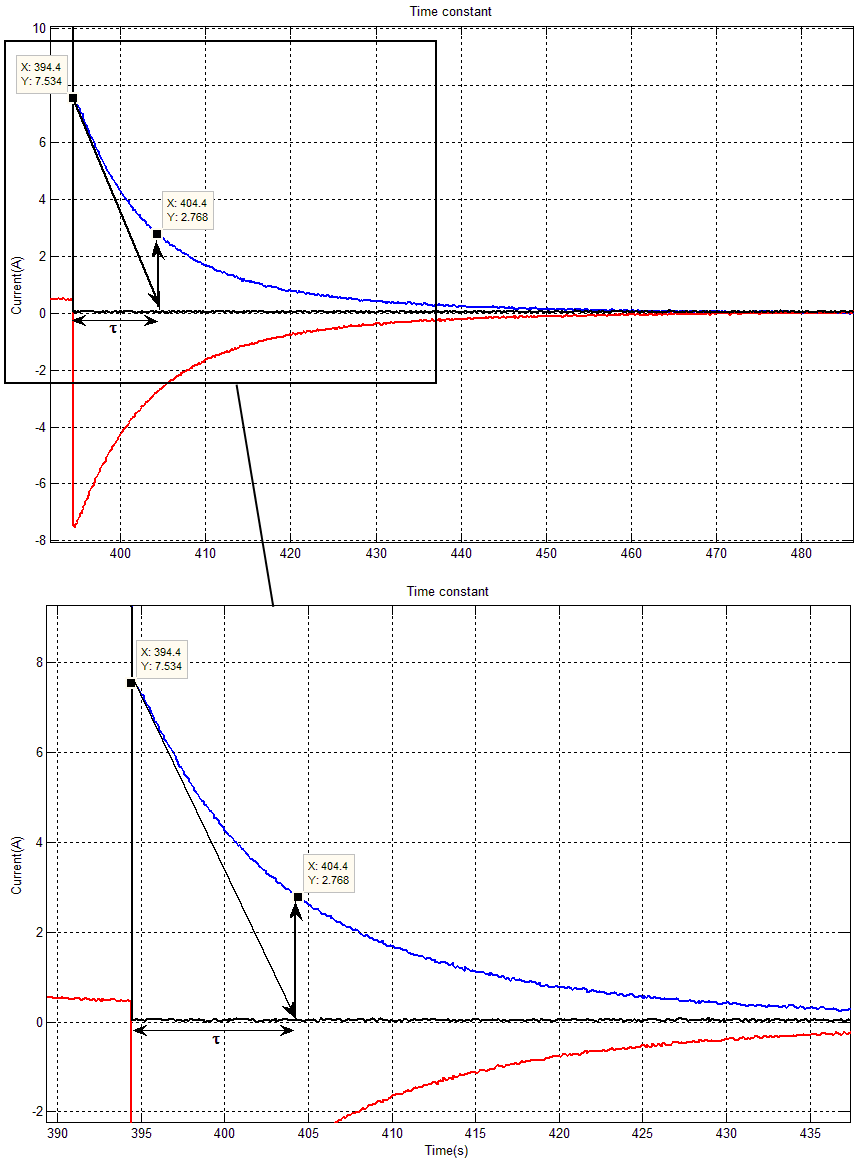

Figure 4.17: Estimation of the time constant of the PHS.

Time constant When the load is turned off, the system currents decay/increase exponentially to zero, as can be seen in figure 4.17.

Using the initial value of the battery current $7,53\,A$, the value at which the current has decayed to 36,8 % of the initial value is $2,77A$. From this we can approximate the time constant graphically, finding the tangent of the initial slope of the exponential curve. This leads to the difference $\tau = \Delta t \approx 404\,s - 394\,s = 10,0\,s$, which is equal to the system time constant.

The voltage is around 48 - 49 V at the moment of measurement in figure 4.17. From the calculated variable capacitance of the supercapacitor shown in figure A.3, we see that the capacitance is around 143 F at this voltage level[25]. Assuming that the capacitance is fixed at this level, and using the total resistance of the battery branch estimated above, $R_{battery,total}$, we can estimate the unknown additional resistance in the supercapacitor branch. Assuming that:

$$\tau = C(R_{battery,total} + R_c + R_{c,add}) \tag{4.41}$$

the unknown additional resistance is:

$$R_{c,add} \approx \frac{\tau}{C} - R_{battery,total} - R_c = \frac{10s}{143F} - 0,036\Omega - 5,8\,m\Omega = 0,028\Omega \tag{4.42}$$

Although there are many uncertainties here, we know that for a fixed capacitance at the given voltage level, the sum of the resistances of the system must be equal to approximately $0,070\,\Omega$ in order to achieve a time constant of approximately 10 seconds.

A simulation of the ideal system results in the exponential profile seen in figure 4.18.

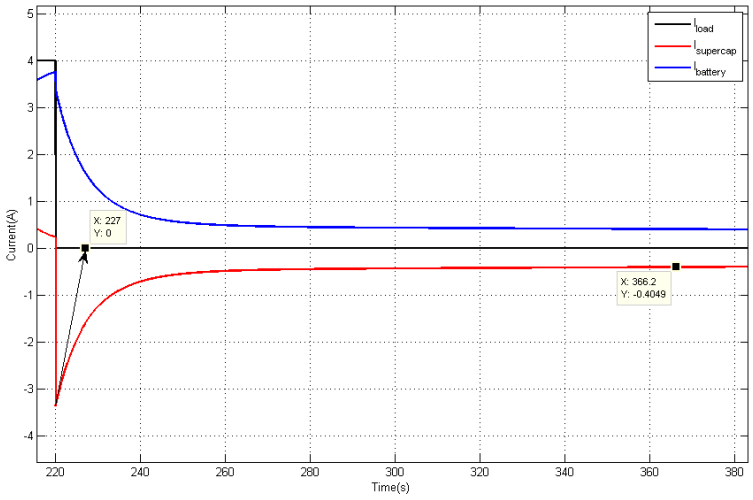

Figure 4.18: Time constant of the passive hybrid system.

As can be seen by graphical inspection, the time constant of the ideal system is approximately $\tau \approx 7 seconds$, which is according to our calculations in section 4.1.3, namely $T_{eigen} = 7,3\,seconds$.

Voltage profile Both the passive hybrid and the battery-alone system was exposed to a pulse train load at different frequencies and duty cycles. In figure

[25] Using the average value of the variable capacitance.

4.19 the measured voltage of the battery-alone system at T = 7,3 seconds and D = 0,5 is shown.

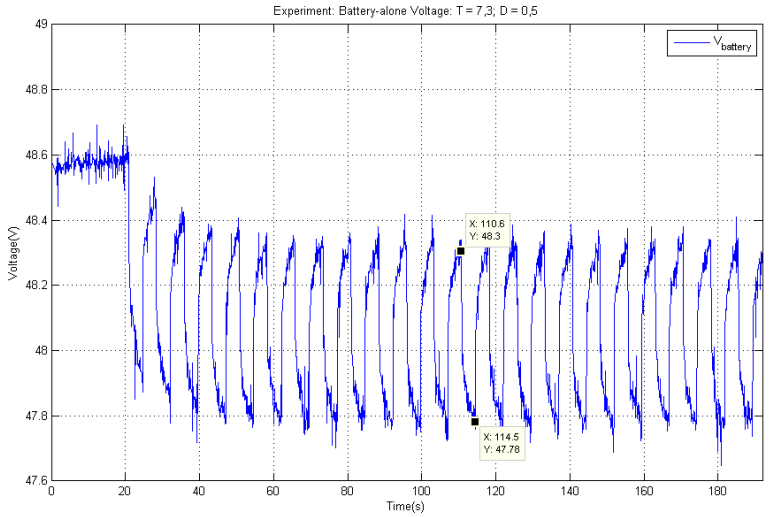

Figure 4.19: Battery voltage for the BAS with T = 7,3 s, D = 0,5 and $I_0 = 12A$.

The measured system voltages of the PHS at T = 7,3 seconds and D = 0,5 can be seen in figure 4.20.

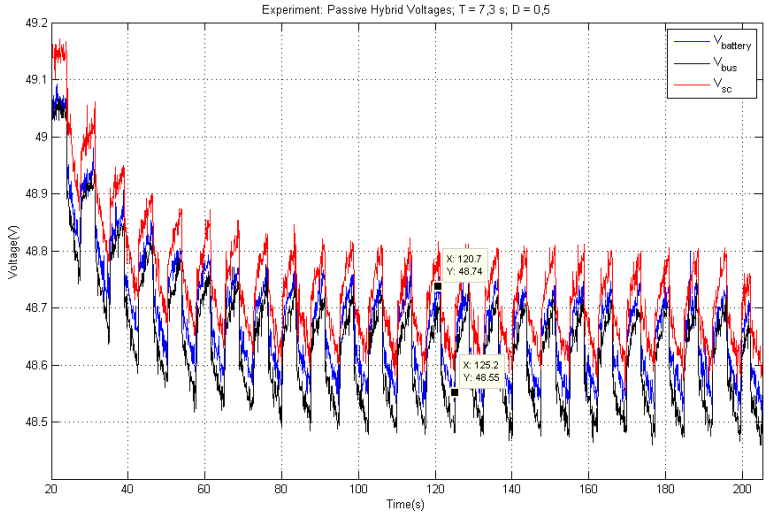

Figure 4.20: System voltages for the PHS with T = 7,3 s, D = 0,5 and $I_0 = 12A$.

A closer inspection of the DC-bus voltage profile can be seen in figure 4.21.

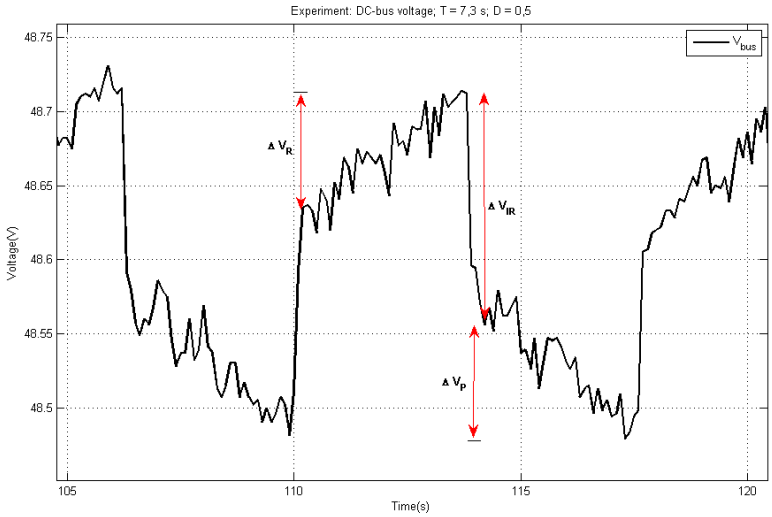

Figure 4.21: A closer inspection of the DC-bus voltage for the PHS with T = 7,3 s, D = 0,5 and $I_0 = 12A$.

Comparing the voltage ripple of the battery-alone and the passive hybrid system at T = 7,3 seconds over different duty cycles gives the result shown in figure 4.22.

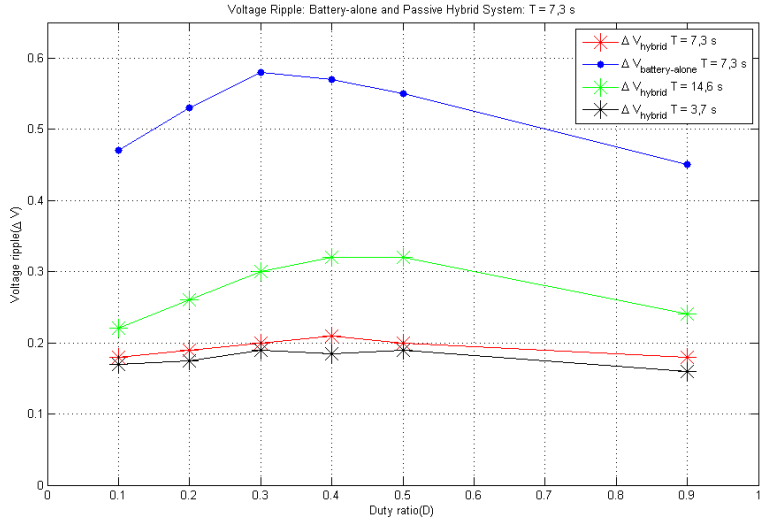

Figure 4.22: Comparison of the voltage ripple of the PHS and the BAS respectively, at different duty cycles. T = 7,3 s, , $I_0 = 12A$.

There is noise effects in the voltage measurement which typically varies with $\pm 0,05V$ at T = 7,3 seconds.

Taking the mean value and the standard deviation of the voltage ripple produced by the PHS at pulse period T = 7,3 s over all duty cycles gives:

$$\Delta\bar{V}_{hybrid} \approx 0,20 \pm 0,01\,V \tag{4.43}$$

and the mean value of the voltage ripple produced by the BAS under the same conditions is:

$$\Delta\bar{V}_{battery-alone} \approx 0,53 \pm 0,05\,V \tag{4.44}$$

That is, the voltage ripple of the PHS is on average reduced by 62 % compared with the BAS when applying a pulse train load with T = 7,3 seconds.

Pulse train loading In figure 4.23 the result of an experiment with pulse train loading with pulse period T = 7,3 s and D = 0,5 can be seen.

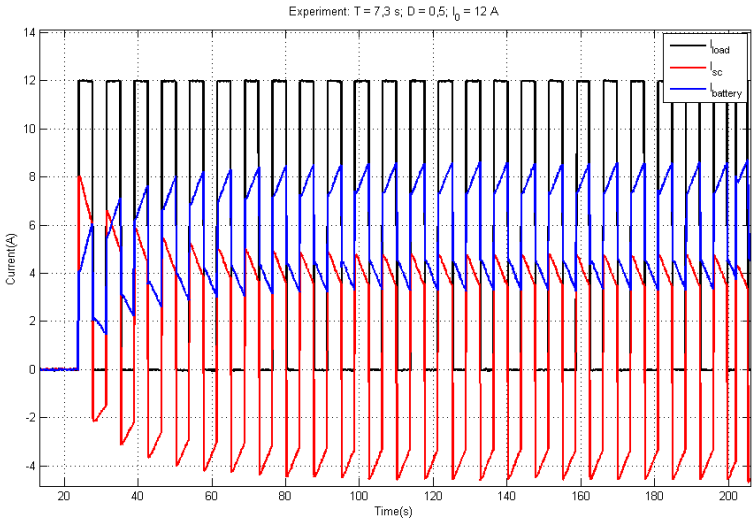

Figure 4.23: Result from experiment with pulse train load. T = 7,3 s, D = 0,5 and $I_0 = 12A$.

Calibrating the Simpower-model based on the estimated additional resistances of the system estimated above, $R_{add} = 0,070\,\Omega$, and running the simulation with the same load parameters in a time window of 400 seconds, gives the result shown in figure 4.24.

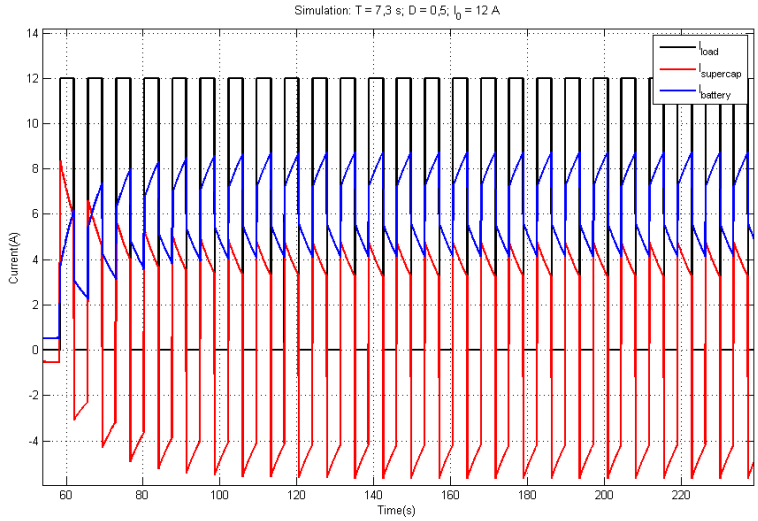

Figure 4.24: Result from simulation with pulse train load. $R_{c,add} = 0,012\,\Omega$ and $R_{b,add} = 0,016\,\Omega$. T = 7,3 s, D = 0,5 and $I_0 = 12A$.

In order to obtain an adequate match in the simulation, it was necessary to add the resistance, $R_{b,add} = 0,016\,\Omega$, in series with the battery branch in addition to the measured internal resistance of the battery: $R_{b,add} = 0,036\,\Omega$.

In figure 4.25 the result of reducing the duty cycle to D = 0,1 can be seen.

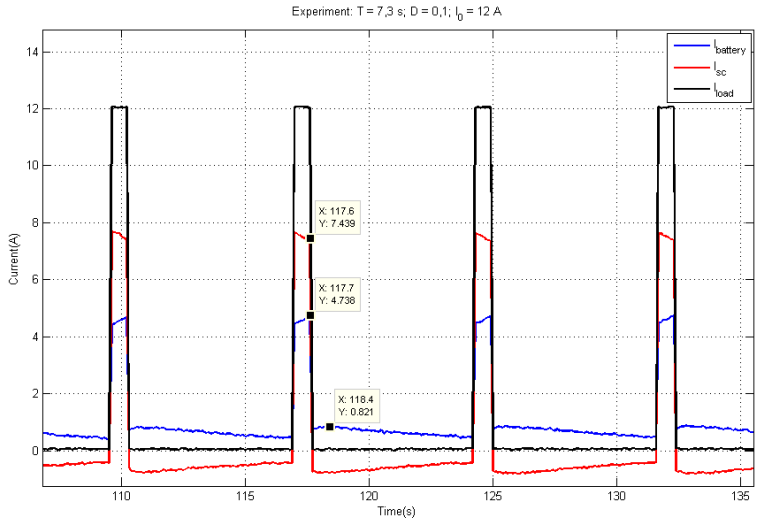

Figure 4.25: Result from experiment with pulse train load as the PHS has reached steady state operation. T = 7,3 s, D = 0,1 and $I_0 = 12A$.

Running the simulation gives with the same load parameters, gives the result

shown in figure 4.26.

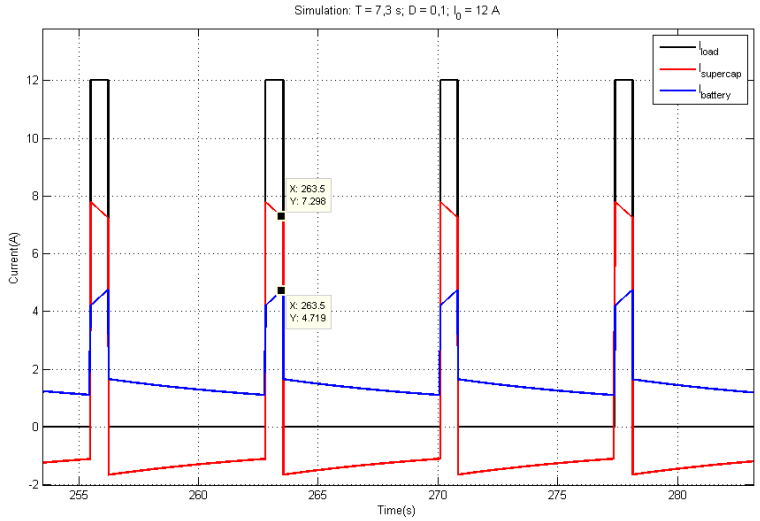

Figure 4.26: Result from simulation with pulse train load as the PHS has reached steady state operation. $R_{c,add} = 0,012\,\Omega$ and $R_{b,add} = 0,016\,\Omega$. T = 7,3 s, D = 0,1 and $I_0 = 12A$.

Increasing the frequency to twice the nominal eigen-frequency, i.e. T = 3,7 seconds, the real system produces the result shown in figure 4.27.

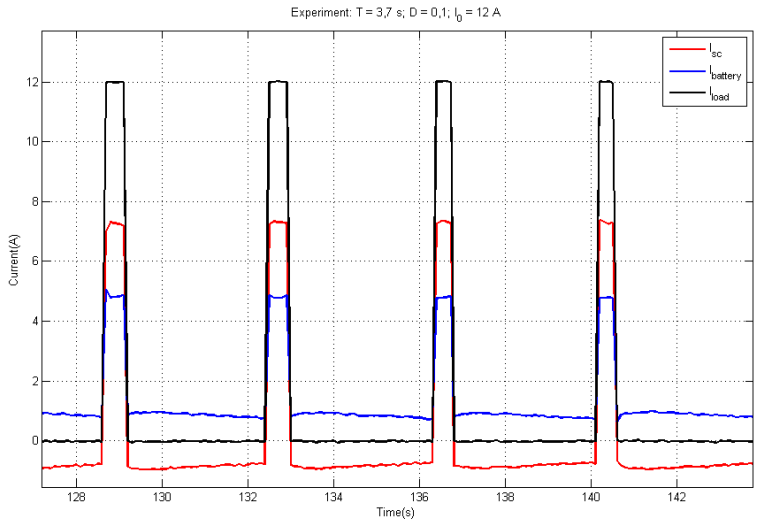

Figure 4.27: Result from experiment with pulse train load as the PHS has reached steady state operation. T = 3,7 s, D = 0,1 and $I_0 = 12A$.

As we increase the duty cycle, we would expect that the supercapacitor takes

a smaller and smaller share of the current. This can be seen in figure 4.28.

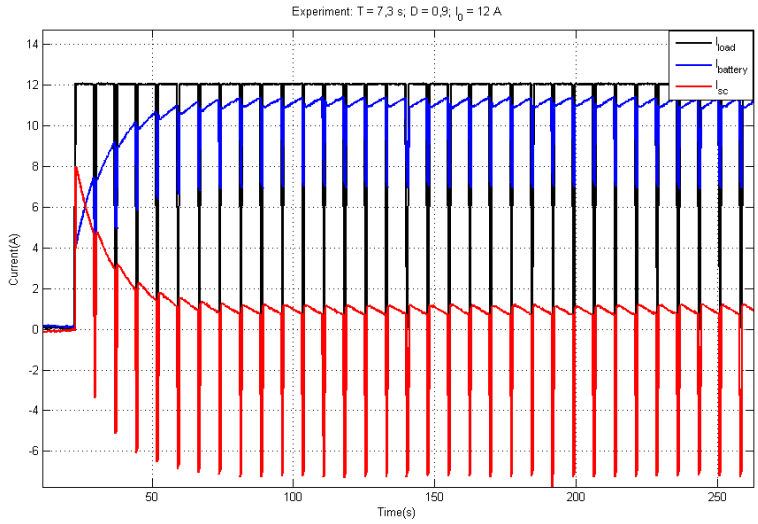

Figure 4.28: Result from experiment with pulse train load. T = 7,3 s, D = 0,9 and $I_0 = 12A$.

Using the same load profile, gives the simulation result shown in figure 4.29.

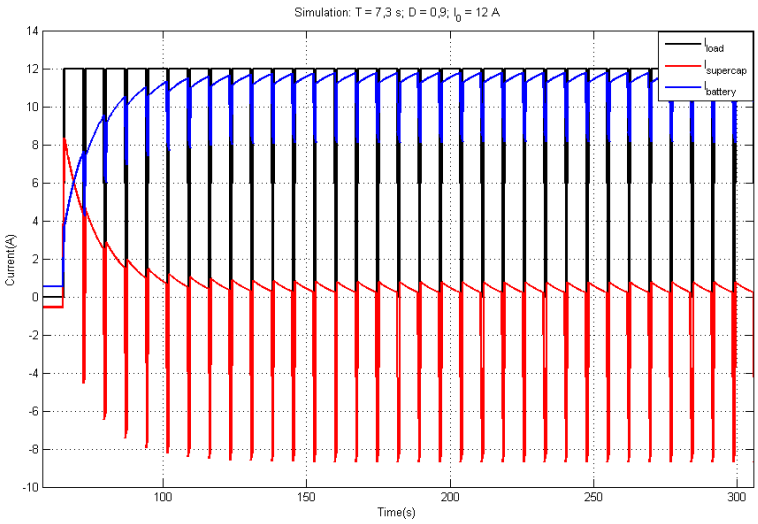

Figure 4.29: Result from simulation with pulse train load. $R_{c,add} = 0,012\,\Omega$ and $R_{b,add} = 0,016\,\Omega$. T = 7,3 s, D = 0,9 and $I_0 = 12A$.

In figure 4.30 the *current sharing factor* for a pulse train load at varying frequencies and duty cycles can be seen. The solid lines represent the current

sharing factor for the new supercapacitor connection through the PV-contactor, while the dotted lines represent the current sharing factor using the former contactor.

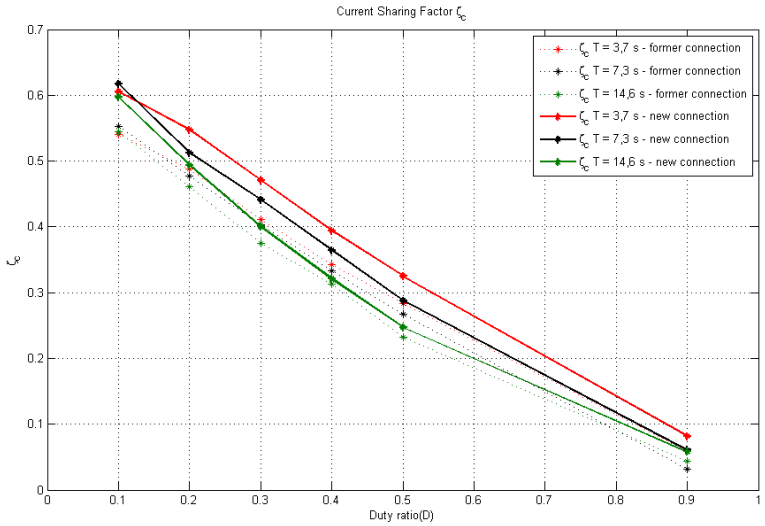

Figure 4.30: Calculated current sharing factor based on measurements with pulse train load at different frequencies and duty cycles. Former connection is the FC-contactor, while the new connection is the PV-contactor. $I_0 = 12A$.

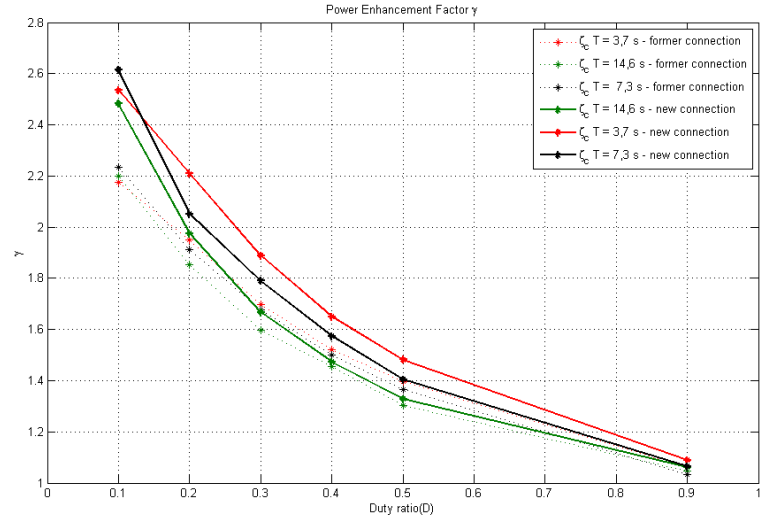

Figure 4.31: Calculated *power enhancement factor* based on measurements with pulse train load at different frequencies and duty cycles. $I_0 = 12A$.

4.3.3 Examination of mismatch between experiments and simulations

We observe that the main difference between the experiment and the simulation is the ampere-hours discharged during the pulse off-time. Using *trapezoidal numerical integration* in Matlab, the area under the curve of the supercapacitor current when D = 0,1 and T = 7,3 seconds at steady state during pulse on-time is approximately 4,5 Ampere-seconds, while in the same region the simulation gives 5,4 Ampere-seconds. During the pulse off-time, the supercapacitor is being charged by the battery. In the experiment the supercapacitor is being charged with approximately 4,0 Ampere-seconds in steady-state operation mode, while the simulation results in 9,2 Ampere-seconds. Thus, in the simulation the supercapacitor is being net charged in steady state operation, i.e. its state of charge increases during loading. On the other hand, in the experiment the supercapacitor is being net discharged at steady-state: more Ampere-seconds is discharged during the pulse than the Ampere-seconds accumulated during pulse off-time. Hence, the state of charge of the supercapacitor decreases during loading.

This individual case is symptomatic of the real system behavior at all duty cycles and frequencies: the supercapacitor is being net discharged by a small amount at each pulse cycle in steady state. The simulated model produces the opposite result under the same conditions: the supercapacitor is being net charged at each pulse cycle in steady state.

However, disconnecting the second branch(intermediate branch) and the leakage resistance in the supercapacitor model produces a result more in accordance with experiment. Now the charging current during pulse off-time is reduced, and the supercapacitor is being net discharged during one pulse cycle in steady state. Given D = 0,1 in steady state with pulse period T = 7,3 seconds, the supercapacitor discharges 5,8 Ampere-seconds and accumulates 5,7 Ampere-seconds during one pulse cycle.

4.3.4 Discussion and summary

It is a challenge to estimate the relative resisitive sharing between the two system branches. The time constant is dependent on the capacitance of the supercapacitor and the combined ohmic resistances of the system. The time constant of the ideal system $T_{eigen} = 7,3\,seconds$ was derived taking only the given internal resistance of the battery, R_b, and the internal resistance of the supercapacitor, R_c, into account. We easily see from equation (4.18), that the eigen-frequency decreases and thus the eigen-period(time constant) increases when additional resistances are added in series with either the battery or the supercapacitor. Using the estimation of the real system time constant, $\tau \approx 10\,seconds$, we find that there exist an additional resistance in the order of $0,028\,\Omega$ somewhere in the system. Using current interrupt technique we found, to our surprise, that the total ohmic resistance in the battery branch, $R_{b,total} = 0,036\,\Omega$, is lower than the previous measured ESR-value of the battery at 90 % state of charge, $R_b = 0,05\Omega$. The state of charge of the battery at the time the measurements were conducted was around 80 %. This may imply that the ESR of the battery is significantly reduced when the state of charge is reduced, which is the opposite of what we would expect. However, in the simulations we had to use an additional resistance in the battery branch in

order to produce a result that resembles the experiments. This was done by calibrating the model by redistributing the total additional system resistance that was estimated using the time constant. Here we used $R_{b,add} = 0,016\,\Omega$ in addition to $R_{b,total} = 0,036\,\Omega$, which combined adds up to $0,052\,\Omega$, not far from the previous measured value at 90% state of charge. This deviation may be due to the fact that the ESR-value was not constant during the experiments, and that its value is sensitive to smaller fluctuations in the battery state of charge.

In accordance with the simulations we observe that the supercapacitor initially takes a greater share of the current. Thereafter, the supercapactior current share decays and stabilizes after approximately 50 seconds, that is approximately five time constants. We see that during the first pulses, the supercapacitor constantly discharges more Ampere-seconds than it accumulates during pulse off-time. Thus the state of charge of the supercapacitor drops drastically during the initial phase. The effect is confirmed when examining the system voltages in figure 4.20. At D = 0,5 and T = 7,3 s the system voltages decreases during the initial pulses, and stabilizes after approximately 50 seconds at around 0,45 V below the initial voltage level. Still, the overall voltage drop is lower than that of the battery-alone system, seen in figure 4.19, which drops approximately 0,5 V during the first 20 seconds.

The system reaches steady state operation mode at the moment the discharged Ampere-seconds are approximately equal to the accumulated Ampere-seconds. Hence, when the system experiences randomly distributed transient peak power demand in time intervals longer then five time constants, the supercapacitor is fully recharged between each power transient and is able to cover a significant larger share of the demand than it can manage under a constant pulse train load.

As can be seen in the simulation result in figure 4.18, the currents does not decay to zero after five time constants. This phenomenon can also be observed before the pulse is applied in figures 4.24 and 4.29. This is mainly due to the intermediate first order branch of the supercapacitor model which have a time constant in the order of $960\,seconds$. It takes therefore a relatively long time before the capacitor C_1 is fully charged and the current through this branch decays to zero. This branch also influence the behavior of the system during the pulse train load, as the supercapacitor model accumulates more ampere-seconds during pulse off-time than it discharges during pulse on-time. Removing this branch gave a more adequate result in accordance with the experimental result. When examining and simulating the immediate transient behavior of the passive hybrid system, the intermediate branch is simply not necessary and can be removed, leaving only the variable capacitance in series with the internal resistance and in parallel with the leakage resistance.

As confirmed through the simulations, the voltage ripple of the BAS is significantly larger than the PHS at all pulse frequencies and duty cycles. At a pulse frequency equal to the nominal eigen-frequency, the voltage ripple is on average reduced by 62% by hybridizing the system. Because of noise effects in the voltage measurement($\pm 0,05V$), the voltage ripple shows no significant duty-cycle dependency at T = 7,3 s and T = 3,7 s. However we see a clear tendency of a ripple increase at T = 14,6 s as the duty cycle approaches D = 0,5. This dependency can also be seen in the battery-alone voltage ripple, but here the peak is reached at D = 0,3. The reason for this is probably the polarization voltage drop and relaxation voltage gain observed in figure 4.21. For the

PHS there is enough time at D = 0,5 for both the polarization drop effect and the relaxation gain effect to influence the ripple at lower frequencies and middle range duty cycles. In regard to the battery-alone system, it is more difficult to explain why the ripple peaks at around D = 0,3. More measurements is needed to confirm that this actually is the case.

The *current sharing factors* of the system at different duty cycles and frequencies, is to a certain degree in accordance with the results obtained through the analytical approach. When calculating the current sharing factor at T = 7,3 seconds and D = 0,1, we saw in section 4.2.2 that the analytical approach produced $\zeta_c = 0,765$, while the simulation of the ideal system in Matlab/Simulink produced $\zeta_c = 0,725$. In the experiment the current sharing factor was reduced to an estimated $\zeta_c \approx 0,62$. When comparing the new connection via the PV-contactor with the former connection via the FC-contactor(lower current rating), we see a significant improvement in the supercapacitor performance. This is due to the reduced additional parasitic resistance and inductance effect when changing to the PV-contactor with higher current rating. Thus, the deviation between the analytical result and the experimental result may be ascribed to the additional ohmic resistances of the system and minor inductance effects.

Being solely dependent on the current sharing factor, the *power enhancement factor* of the system lower at all duty cycles and frequencies when compared to the analytical result shown in figure 4.4. At D = 0,1 and T = 7,3 seconds the analytical calculated factor is around $\gamma = 4,0$, while the experiment produced $\gamma \approx 2,6$, that is 35 % lower than the ideal factor. Hence, for an ideal system it would have been possible for to meet a peak load four times the rated power of the battery at this duty cycle and frequency, while the real system could handle a load that is 2,6 times the rated power of the battery. However, as the duty cycle is increased, the deviation between the ideal case and the real case becomes smaller and smaller. At T = 7,3 seconds and D = 0,5 the real system achieves $\gamma \approx 1,4$ while in the ideal case $\gamma = 1,5$. As expected, both the current sharing factor and the power enhancement factor decreases at frequencies lower than the eigen-frequency and increases by some amount at frequencies higher than the eigen-frequency at middle range duty cycles.

However, we observe that the current sharing factor and thus the power enhancement factor is higher at D = 0,1 at the eigen-frequency, than for T = 3,7, which is twice the eigen-frequency. This is not in accordance with the analytical results. Examining the experimental result in figure 4.27, we can clearly see an inductance effect immediately after the pulse. Hence, at small duty cycles and higher frequencies this effect may produce a reduced current sharing factor at the end of the pulse. As the duty cycle is increased, the current sharing factor is, as expected, higher for T = 3,7 s compared to the lower frequencies.

Based on the measurements conducted it is not possible to compare the power losses in the PHS with the BAS, since the initial voltages for each measurement is not the same and since it was not possible to accurately estimate the internal and additional resistances of the system. Additionally, because of the limited possible load amplitude, it was not possible to compare the passive hybrid system run-time with the battery alone system.

Overall, the conducted experiments have to a certain degree confirmed what we found analytically. We have clearly seen the importance of reducing parasitic resistances and inductances in the system, in order to optimalize the system performance. This is especially important for the supercapacitor branch, since

the load sharing between the supercapacitor and the battery is dependent on the sum of the impedances of the two branches. The smaller the impedance of the supercapacitor branch relative to the battery branch, the higher the share of the load current is covered by the supercapacitor.

5 DC/DC-Converter

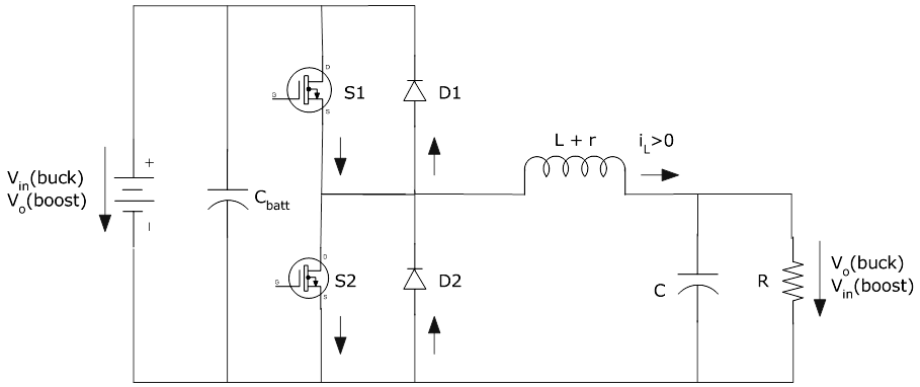

Figure 5.1: The half-bridge bi-directional dc-dc converter

The semi-active hybrid topology could be realized using a bi-directional DC/DC-converter between the supercapacitor and the DC-bus, the battery being directly connected with the common DC-bus and hence directly connected to the load. In this section we will examine the bi-directional DC/DC-converter in detail. Firstly, the design and operation of the converter is examined, followed by a brief discussion of converter losses and efficiency. Secondly, the low-pass filter of the converter is optimized according to the operation conditions of the converter in the topology of interest. Thirdly, the control techniques and proposed control design of the converter is examined in detail, together with a formulation of a converter model that can be implemented in the simulations in Matlab/Simulink. Here our goal is to theoretically demonstrate the basic functioning of the converter. Hence, in order to simplify, the optimazation, control design and modeling of the converter is conducted assuming an ideal converter without any form of power losses. In practical design it is essential that the power losses and efficiency aspects are taken into account.

5.1 Design, operation and converter efficiency

The two-quadrant switch converter, seen i figure 5.1, can be considered as a combination of a step-down buck converter and a step-up boost converter. It consists of two bi-positional switches realized using the transistors $S1/S2$ and the diodes $D1/D2$ in a half bridge configuration. When active power is transferred from the input side, V_{in}, to the load side, V_o, the average load current is positive, $I_o > 0$. When active power is transferred in the opposite direction from the load side to the input side, the average load current is negative $I_o < 0$. It works in a step-down buck mode when $I_o > 0$, and in a step-up boost mode when $I_o < 0$.

5.1.1 Buck mode

When the half-bridge bi-directional converter is operating in buck mode, power is transferred from the battery/dc-bus to the supercapacitor. The average inductor current is positive, $I_L > 0$. The supercapacitor voltage is defined as V_o and the battery/dc-bus voltage as V_{in}.

The fundamental characteristics in the buck mode is as follows[26].

The input voltage is larger then the output voltage, $V_{in} > V_o$. The transistor S_1 opens and closes with a given switching frequency $T_s = t_{on} + t_{off}$. When the switch is closed during t_{on}, the inductor L induces an emf equal to $v_L = V_{in} - V_o$. The diode D_2 is reversed biased and can not conduct. The inductor accumulates volt-seconds and the resulting current increases at a constant rate as a function of time $i_L = \frac{(V_{in} - V_o) \cdot t}{L}$.

After a time, the current is equal to $i_{L,peak} = \frac{(V_{in} - V_o) \cdot t_{on}}{L}$. A magnetic energy corresponding to $W = \frac{1}{2} \cdot L \cdot i_{L,peak}^2$ is now stored in the inductor. When the switch opens, the inductor induces an emf equally in magnitude, but opposite in polarity to V_o, according to Faraday's law. The diode becomes forward biased and the current begins to fall off with a constant rate given by $i_L = i_{L,peak} - \frac{V_o t}{L}$ and reaches its minimum value after the time t_{off}. In steady state, this current is equal to the current value at the beginning of the switching period. The inductor has now transferred all of the accumulated volt-seconds and thereby its stored energy to the load. Plots of the central electrical states can be seen in figure 5.2.

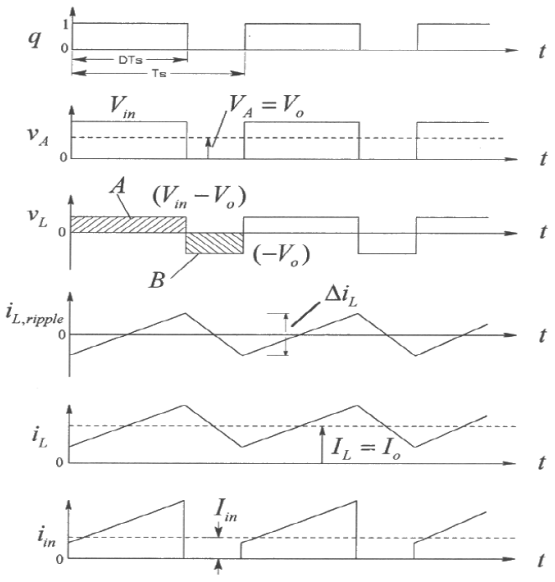

Figure 5.2: Graphical representation of the central electrical states in buck mode. q is the switch value($on = 1$, $off = 0$). v_A is the voltage across the diode D2[36]

The volt-seconds accumulated during t_{on}, is equal to area A in the v_L plot.

[26]The following is based on [34][35][36].

The volt-seconds released during the discharge interval, t_{off}, is equal to area B. The areas are equal in size. This leads to:

$$AreaA = AreaB$$

$$(V_{in} - V_o) \cdot t_{on} = V_o \cdot t_{off}$$

$$\frac{V_o}{V_{in}} = \frac{t_{on}}{t_{on} + t_{off}} = \frac{t_{on}}{T_s} = D \tag{5.1}$$

D is called the duty ratio. The filter capacitor C is large to achieve an output voltage nearly dc $v_o \cong V_o$. The ripple-frequency component of the inductor current, $i_{L,ripple}$, experiences a much smaller impedance through the capacitor than through the load resistance. It follows that $i_C \backsimeq i_{L,ripple}$ [36].

The relationship between the average currents can be found assuming that the input power P_{in} equals the output power P_o(neglecting losses associated with the circuit elements)[35]:

$$P_{in} = P_o$$

$$V_{in} \cdot I_{in} = V_o \cdot I_o \tag{5.2}$$

$$I_{in} = \frac{V_o}{V_{in}} \cdot I_o = D \cdot I_o \tag{5.3}$$

5.1.2 Boost mode

When the half-bridge bi-directional converter is operating in boost mode, power is transferred from the supercapacitor(load-side) to the battery/DC-bus. The average inductor current is therefore negative, $I_L < 0$. The supercapacitor voltage is defined as V_{in} and the battery/dc-bus voltage as V_o. Now it is the transistor $S2$ and diode $D1$ that is active in the energy transferring process. Across the output a filter capacitor, C_{batt}, could be placed. The capacitor forms the voltage port and minimizes the output voltage ripple to the battery. The inductor voltage fluctuates between V_{in} and $-(V_o - V_{in})$. Plots of the central electrical states can be seen in figure 5.3.

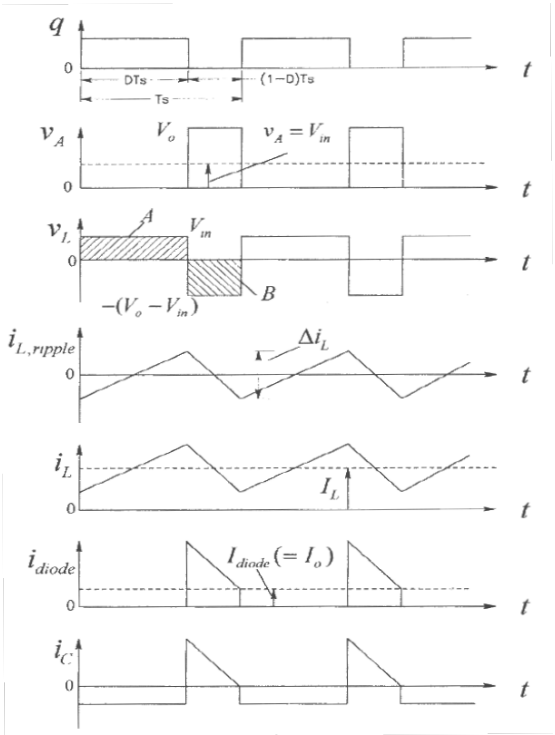

Figure 5.3: Graphical representation of the central electrical states in boost mode[36]

The average inductor voltage is zero during the sub-intervals, so the volt-second areas are equal in magnitude[35]:

$$AreaA = AreaB$$

$$V_{in} \cdot t_{on} = -(V_{in} - V_o) \cdot t_{off}$$

$$\frac{V_o}{V_{in}} = \frac{t_{on} + t_{off}}{t_{off}} = \frac{T_s}{t_{off}} = \frac{1}{1 - D} \tag{5.4}$$

The average diode current I_{diode} equals the output current I_o. To the ripple-frequency component in the diode, the path through the capacitor C_{batt} offers

a much smaller impedance than through the load resistance. The capacitor current can therefore be expressed as $i_c(t) = i_{diode,ripple}(t) = i_{diode} - I_o$ [36]. Equating the input power with the output power gives the following relationship for the average currents:

$$\frac{I_o}{I_{in}} = (1 - D) \tag{5.5}$$

5.1.3 The MOSFET-switch and diodes

In the physical design of the converter, the selection of adequate semiconductor switches, such as power diodes and power transistors, is important. The selection is based on system characteristics such as voltage rating, current rating, switching speeds and on-state voltage[36].

The *diode* is a passive semiconductor switch, in that it is not possible to actively control its on and off conduction state. When the diode is forward biased, it begins to conduct with only a small voltage across it(in the order of 1 V). When reversed biased, the diode acts like an open circuit and only a negligible small leakage current flows through it. If the reversed voltage becomes high and reaches a certain level called the breakdown voltage, the diode will start to conduct. This could damage the diode and should be avoided[35]. In power electronic applications, the diode could be considered as an ideal switch when turned on, as it conducts rapidly compared to the transients in the power circuit. At turn-off, it takes a time, called the reverse recovery time, before the current drops to zero. This could lead to overvoltages in inductive circuits. Therefore, in high-frequency power circuits, one apply special designed *fast-recovery diodes* with low recovery time ratings[35].

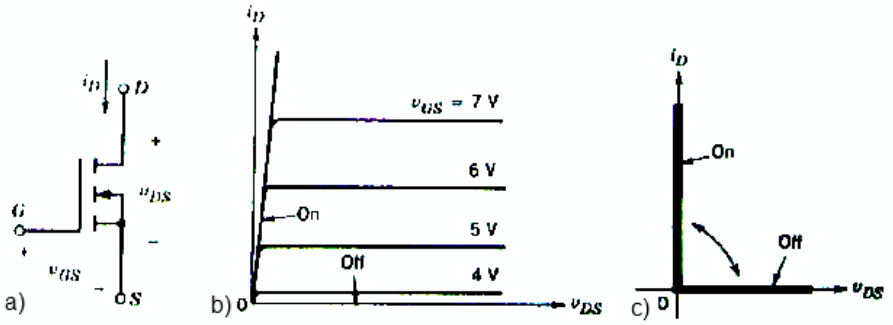

Figure 5.4: a) Symbol of N-channel MOSFET; b) Real i-v characteristics c) Idealized i-v characteristics. v_{GS} is the gate-source voltage [35].

For voltage ratings below a few hundreds volts and current ratings up to 100 A, the power-MOSFET [27] is a preferred choice. Compared to other power transistors, such IGBT and GTO, the MOSFET can handle higher switching frequencies in the excess of 100 kHz. As we saw above, the higher the switching frequency f_s, the smaller the dimension of the low-passfilter and the lower the costs. The power-MOSFET consists of three terminals, the source(cathode), the

[27] Metaloxidesemiconductor field-effect transistor.

drain(anode) and the gate. By controlling the gate-source voltage, the electric field created between p- and n-material components within the transistor can be adjusted, which makes it possible to control the on and off state of the transistor[28]. The MOSFET responds very fast to an applied gate signal, typically the switching times are in the range of ten to a few hundred nanoseconds[35]. In figure 5.4, the real and ideal i-v characteristics of the MOSFET can be seen.

5.1.4 Power losses and efficiency

The efficiency of the converter is defined on terms of its output power, P_0, and the power losses, P_{loss}, within the converter[36]:

$$\eta_{con} = \frac{P_0}{P_0 + P_{loss}} \tag{5.6}$$

The power losses in a converter is associated with the inductor, the filter capacitor, semiconducting switches and diodes.

All semiconductor switches have losses that affect their temperatur and switching efficiency. The transistor losses are primarly due to the fact, that it takes a time before the transistor goes from block mode to conduction mode, and vice versa. In figure 5.5 we see a typical switching characteristic of a real transistor.

[28]P-type materials is basically silicon doped with trivalent atoms, which results in a valence band hole in the material. N-type materials are silicon doped with pentavalent atoms which results in excess of covalent-bond electrons in the materials.

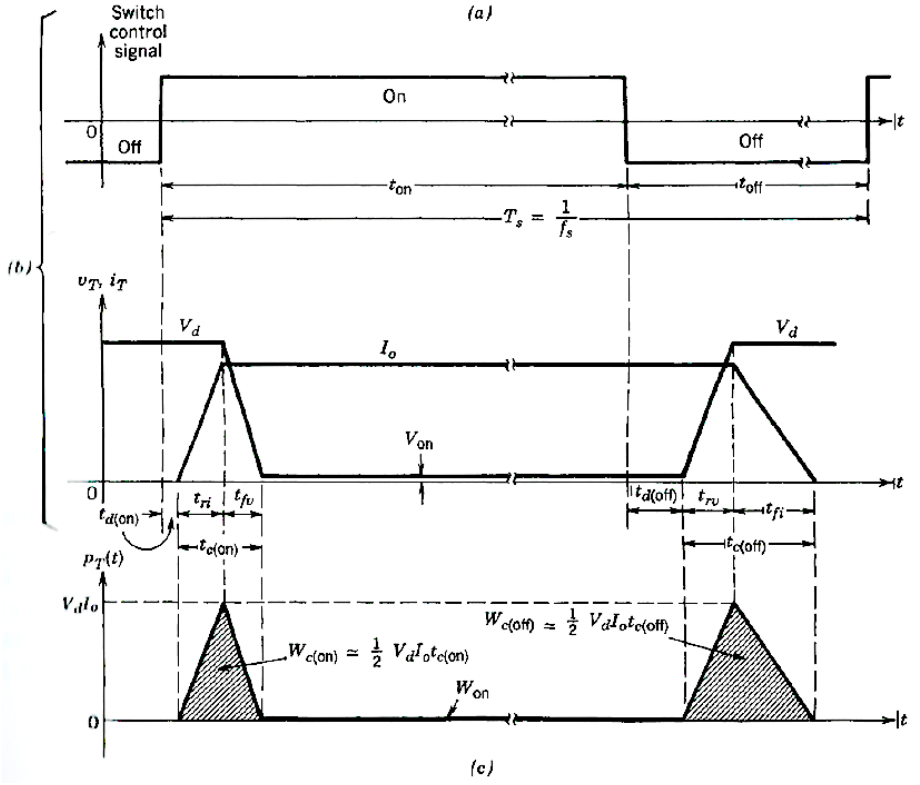

Figure 5.5: Switching characteristics of a real transistor[35].

When the step control signal becomes positive, it takes a time, t_{ri}, before the current I_o rises to the desired level. Likewise, it takes a time, t_{fv}, before the voltage, V_d, across the transistor decreases to zero. During the total turn-on interval, $t_{c(on)} = t_{ri} + t_{fv}$, energy is dissipated in the transistor equal to $W_{c(on)} = 1/2 V_d I_o t_{c(on)}$, which is equal to the shaded area under the power-curve. The same is the case when the control signal becomes negative and the transistor starts blocking the current: energy corresponding to $W_{c(off)} = 1/2 V_d I_o t_{c(off)}$ is dissipated. From this, the average switching loss power, P_s can be approximated with[35]:

$$P_s = \frac{1}{2} V_d I_o f_s (t_{c(on)} + t_{c(off)}) \tag{5.7}$$

where f_s is the switching frequency. We see that the losses increases linearly with increasing f_s. There is therefore a trade-off between switching power losses and the dimensions of the low-pass filter. The higher the switching frequency, the smaller the size of the low-pass filter, but the higher the power losses. Therefore, having a relatively small turn-on and turn-off time, the MOSFET can operate with adequate efficiency at higher switching frequencies than other power transistors available.

Having a small on-state resistance, R_{ds}, there is also a power loss when the transistor conducts. This loss can be approximated by[36]:

V_{in}	48 V
V_o	24 - 48 V
f_s	20 kHz
$P_{o,nominal}$	2 kW
Range of P_o	$(5\% - 100\%)P_{o,nominal}$
$\frac{\Delta V_o}{V_o}$(ouput ripple)	5 %

Table 5.1: Predefined conditions for low-pass filter optimization.

$$P_{cond} = D \cdot R_{ds} I_o^2 \tag{5.8}$$

where D is the duty ratio.

5.2 Optimization of the low-pass filter

5.2.1 Buck mode

In the semi-active topology the operation conditions are predefined according to those found in table 5.1.

Given a constant input voltage, V_{in}, a varying output voltage, $v_o \cong V_o$, a constant switching frequency, f_s, and a preferred minimum output power, P_o, the optimal values for the LC-filter can be calculated. The values should be minimized in order to reduce converter costs. In the following we will assume an ideal converter with ideal switches and diodes, thereby neglecting all forms of power losses within the converter.

Optimizing the inductor L_{min} is the smallest inductance value required to keep the converter operation at the boundary of buck mode under all conditions with the predefined electrical parameters and states[29].

The likelihood that the inductor current will fall to zero, is increased by lowering the duty ratio and thus increasing the off time. The critical boundary value for the inductor current is defined as[35]:

$$I_{LB} = \frac{1}{2} \cdot i_{L,peak} = \frac{t_{on}}{2L}(V_{in} - V_o) = \frac{DT_s}{2L}(V_{in} - V_o) \tag{5.9}$$

Reformulating equation (5.9) gives:

$$L_{min} = \frac{D}{2 \cdot I_{LB} \cdot f_s}(V_{in} - V_o) \tag{5.10}$$

[29]In conventinal one-quadrant buck- or boost-converters this boundary is recognized as the boundary of discontinuous conduction mode(DCM). When the converter enters DCM, I_L is not able to reverse through the diode, resulting in a zero inductor current for a finite time interval. In the bi-directional half-bridge converter this boundary is not discontinuous, since it is the boundary at which the current changes direction.

whereby $L_{min} = f(D, I_{LB}, V_o)$ holding f_s and V_{in} constant. However, the average boundary load current and average boundary inductor current is a function of P_o and V_o:

$$I_{LB} = I_{oB} = \frac{P_o}{V_o} \tag{5.11}$$

and the duty ratio is a function of V_o. Equation (5.10) becomes:

$$L_{min} = \frac{D}{2 \cdot I_{LB} \cdot f_s}(V_{in} - V_o) = \frac{V_o}{V_{in}} \cdot \frac{1}{\frac{2 \cdot P_o}{V_o} f_s} \cdot (V_{in} - V_o) = \frac{V_o^2 V_{in} - V_o^3}{2 \cdot V_{in} P_o f_s} \tag{5.12}$$

Figure 5.6 shows L_{min} as a function of P_o and V_o.

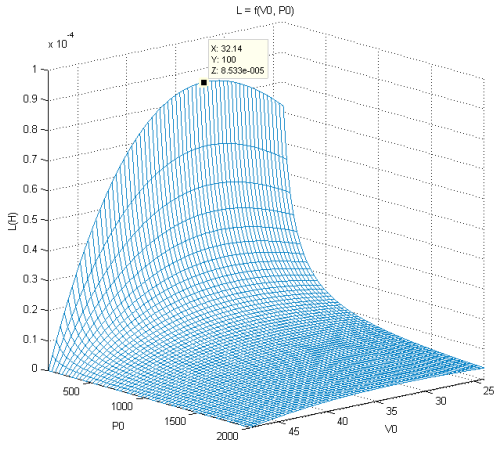

Figure 5.6: Graphical 3-D-representation of $L_{min} = f(P_o, V_o)$

Choosing the lowest predefined value of $P_o = P_{o,nominal}5\%$ and differentiating (5.12) with respect to V_o, gives eventually the value of V_o at which L_{min} has it's maximum value:

$$V_o = \tfrac{2}{3} \cdot V_{in} = 32V$$

$$L_{min} = \frac{(32V)^2 \cdot 48V - (32V)^3}{2 \cdot 48V \cdot 100W \cdot 20kHz} = 85\mu H \tag{5.13}$$

Simulation with the calculated value under the optimal electrical conditions in Matlab/Simulink using the Simpower blockset, gives the result shown in figure 5.7.

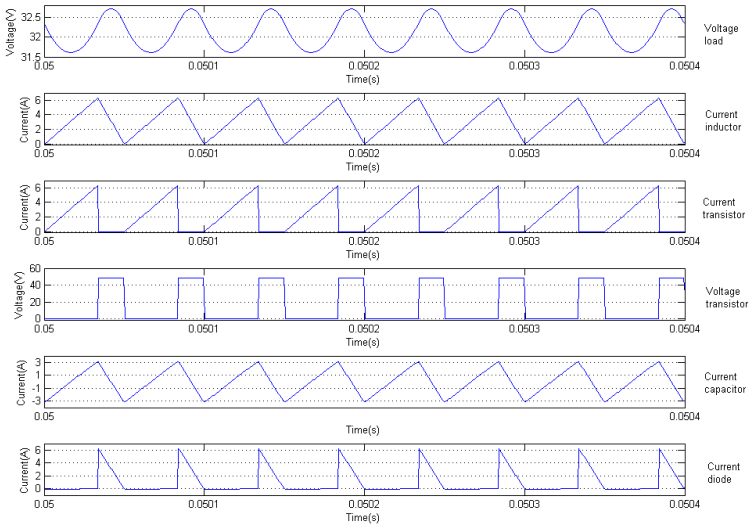

Figure 5.7: Results of simulations in buck mode with $L_{min} = 85\mu H$, $P_o = 100W$, $V_o = 32V$ and $V_{in} = 48V$.

Studying the inductor current in figure 5.7, it is clear that the converter operates on the boundary between buck and boost mode. Decreasing the value of L, will lead the converter into boost mode under the same operating conditions. The calculated inductance is multiplied with ten, in order to secure a sufficiently reduced ripple current. This gives $L_{min} = 850\,\mu H$.

Optimizing the filter-capacitor When calculating the optimal capacitance value, one can assume that the entire ripple component in i_L flows through the capacitor $i_c(t) \simeq i_{L,ripple}$. Its average component $I_L = I_o$ flows through the load, whereby the peak to peak voltage ripple at the output ΔV_o is given by[35]:

$$\Delta V_o = \frac{\Delta Q}{C} = \frac{1}{C}\frac{1}{2}\frac{\Delta i_L}{2}\frac{T_s}{2} \tag{5.14}$$

The peak to peak current ripple is defined by:

$$\Delta i_L = \frac{1}{L}(V_{in} - V_o) \cdot DT_s = \frac{1}{L} \cdot V_o \cdot (1 - D)T_s \tag{5.15}$$

Substituting into (5.14) gives:

$$\Delta V_o = \frac{T_s}{8C}\frac{V_o}{L} \cdot (1 - D)T_s \tag{5.16}$$

The fractional ripple of total output voltage output can then be written as:

$$\frac{\Delta V_o}{V_o} = \frac{1}{8}\frac{T_s^2(1 - D)}{LC} = \frac{\pi^2}{2}(1 - D) \cdot (\frac{f_c}{f_s})^2 \tag{5.17}$$

where f_c is the corner frequency of the low-pass LC-filter defined as:

$$f_c = \frac{1}{2\pi\sqrt{LC}} \tag{5.18}$$

This shows that the voltage ripple can be minimized by selecting f_c such that $f_c \ll f_s$. Reformulating (5.16) with respect to the capacitance C gives:

$$C = \frac{T_s}{8L}\frac{V_o}{\Delta V_o} \cdot (1-D)T_s \tag{5.19}$$

The capacitance is inverse proportional to L and proportional to the negative of D.

Using (5.19) with the calculated value for $L_{min} = 85\,\mu H$, we see that the capacitance has a maximum when the duty ratio D is at a minimum, which is $D = 0.5$ in the buck mode, that is when V_o is 24 V. This leads to:

$$C = \frac{1}{{f_s}^2 \cdot 8L_{min}}\frac{V_o}{\Delta V_o} \cdot (1-D) = \frac{1}{(20kHz)^2 \cdot 8 \cdot 85\mu H \cdot 0,05} \cdot (1-0,5) = 36\mu F \tag{5.20}$$

Calcultaing the corner frequency with the derived values gives $f_c \approx 2800Hz$, that is about 14% of the switching frequency f_s. Using the calculated values for the LC-filter in a simulated model in the buck mode under these conditions gives the results shown in figure 5.8.

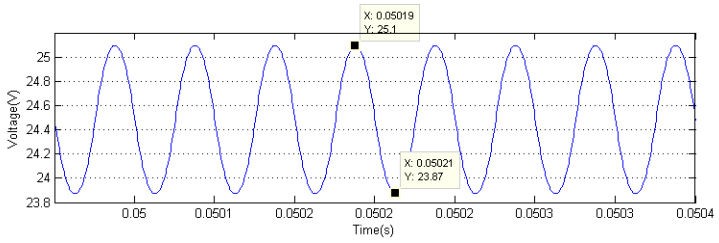

Figure 5.8: Plot of V_o using $C = 36\mu F$, $L = 85\mu H$ and $P_o = 100W$.

As can be seen in figure 5.8, the fractional voltage ripple is $\frac{\Delta V_o}{V_o} = \frac{25,10V-23,87V}{24,5V} = 0.0502$, which is in accordance with the calculations. Increasing the power and/or the duty cycle, will reduce the voltage ripple from this maximum level. Using the up-scaled inductance value $L_{min} = 850\mu H$ leads eventually to $C = 3,6\mu F$.

5.2.2 Boost mode

In the semi-active topology the operation conditions are predefined according to those found in table 5.2.

The critical boundary value for the current on the battery side(load) is defined as:

$$I_{oB} = \frac{T_s V_o}{2L} \cdot D(1-D)^2 \tag{5.21}$$

The minimal inductance required is then given by:

$$L_{min} = \frac{T_s V_o}{2 \cdot I_{oB}} \cdot D(1-D)^2 \tag{5.22}$$

V_o	48 V
V_{in}	24 - 48 V
f_s	20 kHz
$P_{o,nominal}$	2 kW
Range of P_o	$(5\% - 100\%)P_{o,nominal}$
$\frac{\Delta V_o}{V_o}$(ouput ripple)	5 %

Table 5.2: Predefined conditions for low-pass filter optimization.

The independent variables are now P_o and V_{in} and the average load boundary current can be expressed as $I_{oB} = \frac{P_o}{V_o}$. Expressing D in terms of V_o and V_{in} in (5.22), with $(1-D)^2 = (V_{in}/V_o)^2$, and substituting for I_{oB} gives:

$$L_{min} = \frac{V_o^2 \cdot (\frac{V_o - V_{in}}{V_o})(\frac{V_{in}}{V_o})^2}{2 \cdot P_o \cdot f_s} = \frac{(\frac{V_o - V_{in}}{V_o})(V_{in})^2}{2 \cdot P_o \cdot f_s} \tag{5.23}$$

One sees that L_{min} has a maximum when P_o is at it's minimum, and differentiating (5.23) with respect to V_{in} gives a maximum when $V_{in} = \frac{2}{3}V_o$. Using the minimum value $P_o = P_{o,nominal} \cdot 5\%$ results in:

$$L_{min} = \frac{(\frac{48V - 32V}{48V})(32V)^2}{2 \cdot 100W \cdot 20kHz} = 85\mu H \tag{5.24}$$

This is the same minimum value that was derived above for the buck mode. A simulation in Matlab/Simulink, using the calculated value under the optimal electrical conditions, gives the result shown in figure 5.9.

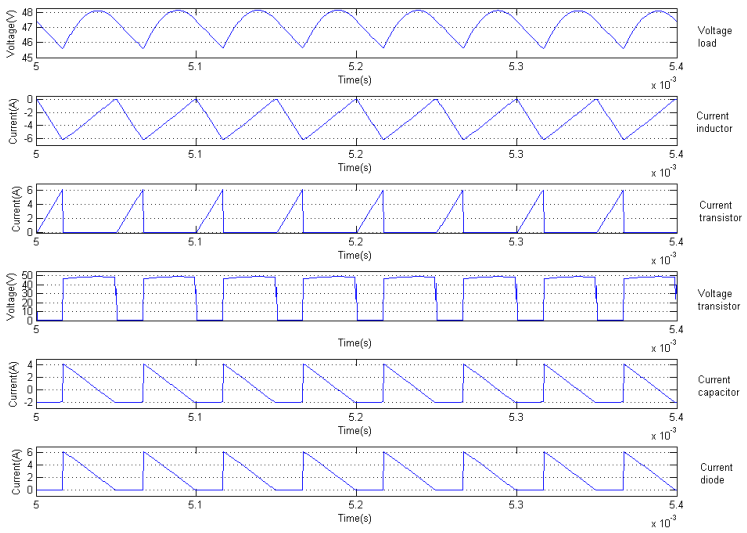

Figure 5.9: Results of simulations in boost mode with $L_{min} = 85,33\mu H$, $P_o = 100W$, $V_{in} = 32V$ and $V_o = 48V$.

One can see from the inductor current plot in figure 5.9, that the converter is at the boundary between CCM and DCM. Decreasing the value of L further, will results in DCM.

The capacitance at the battery side should absorb all the ripple of the current that flows through the diode. The peak to peak voltage ripple can then be expressed as:

$$\Delta V_o = \frac{\Delta Q}{C_{batt}} = \frac{I_o \cdot D \cdot T_s}{C_{batt}} \tag{5.25}$$

Reformulating (5.25) and expressing it in terms of V_{in} and P_o gives:

$$C_{batt} = \frac{I_o \cdot D \cdot T_s}{V_o} \cdot \frac{V_o}{\Delta V_o} = \frac{P_o(V_o - V_{in})}{V_o^3 \cdot f_s \cdot 0.05} \tag{5.26}$$

One sees that C_{batt} is independent of the inductance value and has it's maximum value when V_{in} is at it's minimum and P_o is at it's maximum. This leads to:

$$C_{batt} = \frac{2kW(48V - 24V)}{(48V)^3 \cdot 20kHz \cdot 0.05} = 0,43mF \tag{5.27}$$

Simulating in Simpower with the $P_o = 2kW$, $V_o = 24V$ and the calculated capacitance and inductance values given, gives the result shown in figure 5.10.

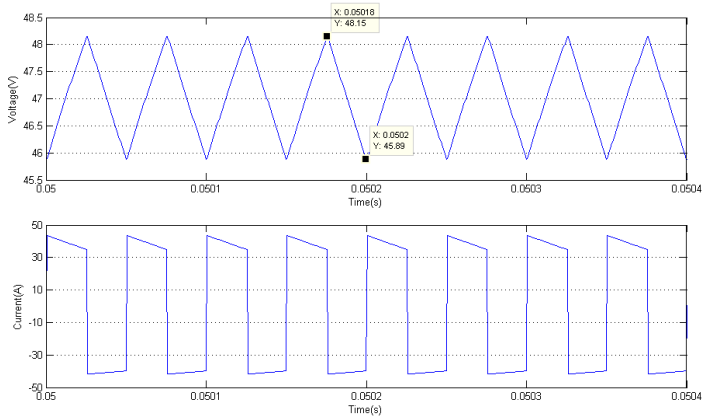

Figure 5.10: Results of simulations in boost mode with $L_{min} = 85\mu H$, $C_{batt} = 0,43mF$, $P_o = 2kW$, $V_{in} = 24V$ and $V_0 = 48V$. The uppermost figure shows the output voltage V_o, while the lowest figure shows the current going through the capacitor.

Studying figure 5.10 one finds $\frac{\Delta V_o}{V_o} = \frac{48.15V - 45,89V}{47,00V} = 0.0481$. This is adequately close to the maximum ripple fraction on which the calculations are based. Increasing the input voltage or reducing the output power will eventually reduce the ripple from the maximum ripple level shown in figure 5.10. As above, we multiply the minimal values with ten in order to secure a low current ripple. This leads to $C_{batt} = 4,3mF$. In order to simplify the modeling in the following, we will only use a filter capacitor on the supercapacitor side and not implement the filter capacitor on the battery side.

5.3 Control and modeling

5.3.1 PWM Control of dc-dc converters

With a given input voltage, the average output voltage is controlled by controlling the switching of the semiconducting transistors. The mostly used method for controlling the gate signal to the transistor, is the Pulse Width Modulation technique(PWM). It is based upon a switch mode at constant frequency f_s. The switch control signal, $q(t)$, which controls the state (on or off) of the transistor, has typically a value 1 when the transistor is on(short circuit) and the value 0 when the transistor is off(open circuit). It is generated by comparing a control voltage v_c with a repetitive waveform voltage v_r with a frequency equal to f_s. When v_c is higher than v_r, the comparator produces the switch control signal, q(t), that is sent to the transistor gate, turning it on. When v_c is lower than v_r, the comparator produces an output signal $q(t) = 0$. Example of comperator signals with a sawtooth/ramp voltage v_r compared with the control input v_c can be seen in figure 5.11. In terms of v_c and the peak of the sawtooth waveform V_r, the duty ratio D can be expressed as[35]:

$$D = \frac{t_{on}}{T_s} = \frac{v_c}{\hat{V}_r} \tag{5.28}$$

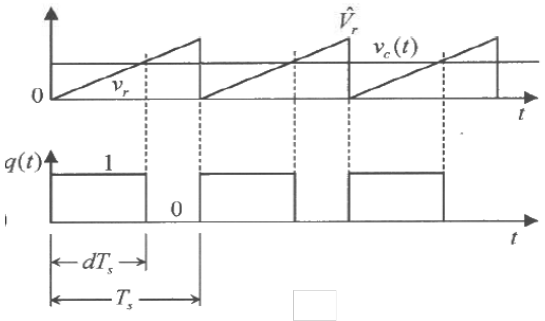

Figure 5.11: Pulse width modulation. Example of comperator signals $v_c(t)$ compared with v_r producing the output q(t)[35].

5.3.2 The dynamic average model of the DC/DC-converter

To be able to capture the converter performance under a dynamic regime, i.e. changing input voltage and/or output load, it is beneficial to represent the converter circuit as an average model. Under a dynamic condition, the converter duty-ratio and the average values of voltages and currents vary with time[30]. In the following we will assume an ideal converter and thereby ignore power losses in switches and diodes.

In the average representation of the switching power pole, all the switching information is removed. This facilitates the simulation of the converter, making simulation going faster then by using the standard circuit design. It results in a linear model of the plant, linearized around the steady state dc operating

[30]The following is based on [36][35][1].

point, assuming small signal ac perturbations. The average quantities can be expressed as the sum of its steady state dc value and this small-signal perturbation.

$$\bar{i}_L = I_L + \tilde{i}_L \tag{5.29}$$

$$\bar{v}_{in}(t) = V_{in} + \tilde{v}_{in}(t) \tag{5.30}$$

$$\bar{d}(t) = D + \tilde{d}(t) \tag{5.31}$$

The letters with a bar '$\bar{}$' represent the average dynamic values, the upper case letters are the steady state average values, and the letters with '~' represent the small signal perturbation.

The voltage input v_{in} can be assumed as pure dc whereby $\tilde{v}_{in}(t) = 0$.

For a buck converter in switch mode, the average voltage and current relationships in dc-steady state are as follows:

$$V_o = DV_{in}$$

$$I_{in} = DI_o = DI_L$$

Under dynamic conditions, the average switch mode model can be transformed into a dynamic average model where the switches are substituted with variable current and voltage sources. This results in the following:

$$\bar{v}_o(t) = d(t)\bar{v}_{in}(t) \tag{5.32}$$

$$\bar{i}_{in}(t) = d(t)\bar{i}_L(t) \tag{5.33}$$

A new averaged equivalent circuit can thereby be formulated, which is shown in figure 5.12.

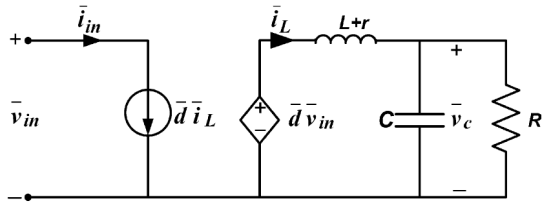

Figure 5.12: Average dynamic model of the half-bridge converter[1].

The inductor is represented with a small internal ohmic resistance, r, and the voltage across the filter capacitor is $\bar{v}_c = V_c + \tilde{v}_c$. Using Faraday's law results in:

$$-\bar{v}_{in} - \bar{d}\bar{v}_{in} + \bar{i}_L \cdot r + \bar{v}_c = -L\frac{d\bar{i}_L}{dt}$$

Applying Kirchoff's node rule gives:

$$\bar{i}_L = C\frac{d\bar{v}_c}{dt} + \frac{\bar{v}_c}{R}$$

The focus of attention is the small signal perturbation, so when the average dynamic quantities are substituted according to equations presented above, all

the steady state variables are set equal to zero, as well as the products of two small signal perturbations. For example $\tilde{d} \cdot \tilde{v}_c \approx 0$.

Substituting and expressing both equations in terms of the differentials leads to:

$$\frac{d\tilde{i}_L}{dt} = -\frac{r}{L}\tilde{i}_L - \frac{1}{L}\tilde{v}_c + \frac{V_{in}}{L}\tilde{d} \tag{5.34}$$

$$\frac{d\tilde{v}_c}{dt} = \frac{1}{C}\tilde{i}_L - \frac{1}{RC}\tilde{v}_c \tag{5.35}$$

The task is to find the transfer function, $G_p(s)$, of the small signal average model, i.e. the fractional relationship between the output variable, $\tilde{i}_L$, and the input variable, $\tilde{d}$. Transforming equation (5.34) and (5.35) into the Laplace domain results in:

$$s\tilde{i} = -\frac{r}{L}\tilde{i}_L - \frac{1}{L}\tilde{v}_c + \frac{V_{in}}{L}\tilde{d}$$

$$s\tilde{v}_c = \frac{1}{C}\tilde{i}_L - \frac{1}{RC}\tilde{v}_c$$

Substituting with the intermediate dynamical variable $\tilde{v}_c$, leads eventually to the plant transfer function:

$$G_p(s) = \frac{\tilde{i}_L}{\tilde{d}} = \frac{\frac{V_{in}}{L}(s + \frac{1}{RC})}{s^2 + \frac{(RCr+L)}{LRC} \cdot s + \frac{r+R}{LRC}} \tag{5.36}$$

5.3.3 PI-controller

A common method of compensation is cascade compensation, that is, the compensator is placed in cascade with the plant[31]. One type of compensators is the proportional-integral(PI) compensator, which feeds the error(proportional) plus the integral of the error forward to the plant. Since the PI-compensator can ensure zero steady-state error when tracking dc-quantites, it is commonly used in DC/DC-converters and hence also our choice. The block representation of this cascade compensation can be seen in figure 5.13.

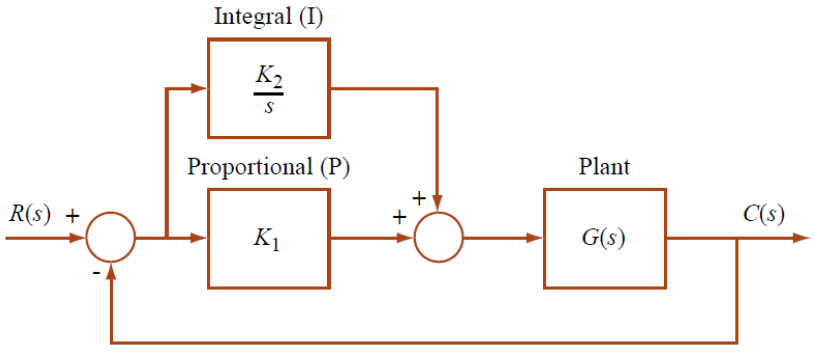

Figure 5.13: PI-compensator in cascade with the plant[37].

[31] For more background on control theory, see Appendix A.1.

The compensator transfer function is given as:

$$G_c(s) = K_p + \frac{K_i}{s} = \frac{K_p s + K_i}{s} = \frac{K_i/K_p + s}{s} \cdot K_p \tag{5.37}$$

One can see from equation (5.37) that the PI-compensator places an open-loop pole at the origin, which increases the system type by one order. [32] It also places a zero, $z = -\frac{K_i}{K_p}$, on the negative real axis, but close to the integrator's pole at the origin. Therefore, the two cancels out. The net effect is a fixed steady-state error without effecting the transient response. Without this zero and only integral action, the response would have been slowed down, i.e. higher rise time[38].

In modern control technique the PI-controller is usually digitalized. However, for a better understanding of it's properties, it can be advantageous to study the analog PI-controller build around an operational amplifier(op-amp) seen in figure 5.14.

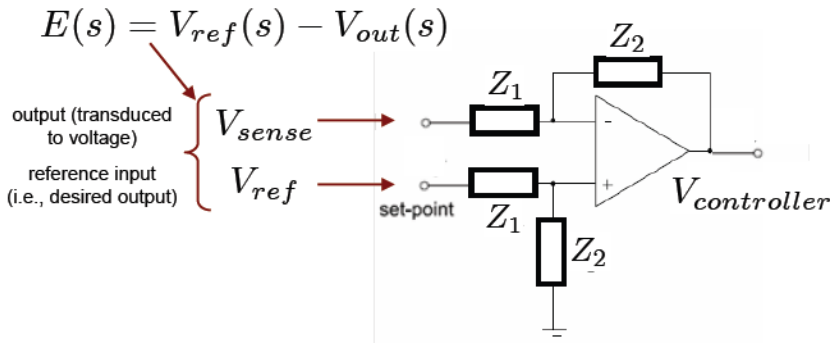

Figure 5.14: Analog PI-controller build around an operational amplifier[37].

The impedance, Z_1, consists of an ohmic resistance, $Z_1 = R_1$, whereas the impedance Z_2 is a series connection of an ohmic resistance and a capacitor $Z_2 = R_2 + 1/Cs$. Due to the op-amp's virtual ground the controller transfer function becomes[37]:

$$G_s(s) = \frac{V_{controller}}{V_{sense} - V_{ref}} = \frac{Z_2(s)}{Z_1(s)} = \frac{R_2 + 1/(Cs)}{R_1} = \frac{R_2}{R_1}(1 + \frac{1}{R_2 C}) = K_p + \frac{K_i}{s} \tag{5.38}$$

where $K_p = \frac{R_2}{R_1}$ and $K_i = \frac{1}{R_1 C}$.

In the modeling approach the controller will not be modeled as the analog compensator described above. We simply formulate a signal model in Simulink based on the mathematical properties of the controller, shown in figure 5.15.

[32] For example, a Type 0 system transforms into a Type 1 system. In responds to a step input, the system should now respond with zero steady-state error.

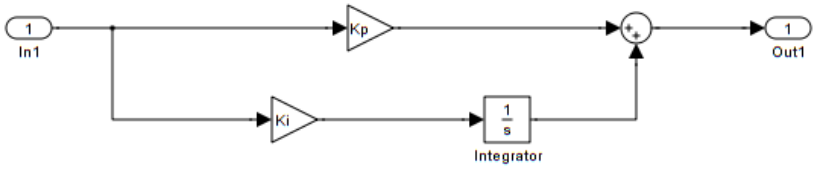

Figure 5.15: PI-controller formulated in Simulink.

5.3.4 Control requirements

Our objective is to design a feedback controller for the DC/DC-converter which enables us to control the inductor current, i_L, flowing to and from the supercapacitor. In the feedback control system, the inductor current, i_L, is measured and compared with a reference value, $i_{L,ref}$. The error between the two acts on the PI-controller which produces the control voltage, $v_c(t)$. The control voltage acts as the input of the PWM to produce a switching signal, $q(t)$, which is sent to the control gate of the MOSFET-transistors. The average value of this signal is the duty cycle $d(t)$.

The overall open-loop transfer function here becomes:

$$G_{OL}(s) = G_p(s) \cdot G_c(s) \cdot H(s) \tag{5.39}$$

where $G_c(s)$ is the transfer function of the PI-compensator, $G_p(s)$ is the plant transfer function and $H(s)$ is the transducer transfer function. The PWM block transfer function is here assumed as unity and does therefore not appear in (5.39).

In order to simplify the modeling and simulations of the converter and the feedback control, the dynamic average representation, described above, is implemented. The inductor current i_L is measured and compared with a reference value, $i_{L,ref}$. The error between the two acts on the PI-controller which now directly produces the duty cycle, $d(t)$. $d(t)$ is multiplied with the instantaneous inductor current, $i_L(t)$, generating the control signal to the controlled current source; accordingly, $d(t)$ is multiplied with the input voltage, $v_{in}(t)$ (battery side of the converter), generating the control signal to the controlled voltage source. The only difference between the real switch mode model and the dynamic average model, is that the PWM transfer function is assumed as unity and is included in the PI-controller.

The feedback controller to regulate the average current must be designed with the following characteristics[36]:

1. zero steady state error
2. fast response to changes in the input voltage and the output load
3. low overshoot
4. low noise susceptibility

For a given $G_p(s)$ and a fixed $H(s)$, the task is to properly tailor $G_c(s)$ so that $G_{OL}(s)$ meets the performance requirements listed above. In the control

analysis the most important characteristics of the open-loop transfer function are[36]:

1. The gain at low frequencies should be high to minimize the steady-state error, e_{ss}, in the output.

2. The crossover frequency is the frequency at which the gain of $G_{OL}(s)$ falls to unity(0 dB). This crossover frequency, ω_c, should be as large as possible, since the rise time, T_r, of the closed loop response is approximately equal to $T_r \approx \frac{1}{\omega_c}$, but approximately an order of magnitude below the switching frequency, f_s, allowing the load to respond quickly to the transients, such as sudden changes of load.

3. The phase margin is defined as: $PM = \phi_{OL} + 180°$, where ϕ_{OL} is the phase angle of $G_{OL}(s)$ at the crossover frequency. PM should be a positive quantity. It determines the transient response of the output in response to sudden changes in the load. A PM in a range of 45°- 60°is desirable.

5.3.5 Control design

We can now turn to a more detailed analysis of the proposed control design, resulting in an adequate controller that satisfy the above mentioned requirements. The design objectives and the system's performance revolve around the transient response, the steady-state error and the stability of the system.

In the following we use the following parameters:

- $L = 850\mu H$
- $C = 3,6\mu F$
- $V_{in} = 48V$
- $r = 0,05\Omega$[33]
- $P_o = 2kW$
- $V_o = 24V$
- $R = (V_0)^2/P_0 = 0,288\Omega$

The parameters is thus set equal to a situation with nominal loading and a supercapacitor voltage, V_o, at the lower limit of its operation range, which gives the minimal value that R can take.

In order to formulate a control design, a prerequisite criterion for the system is that it must be *stable*. According to the definition in Appendix A.1, a linear, time-invariant system is stable, if the natural response approaches zero as time approaches infinity.

Imposing an impulse test input function, $\delta(t)$, to the plant, $G_p(s)$, from equation (5.36), results in the response shown in figure 5.16. One can see that the natural response decays to zero as the time approaches infinity, so the system is stable.

[33]Taken from [1].

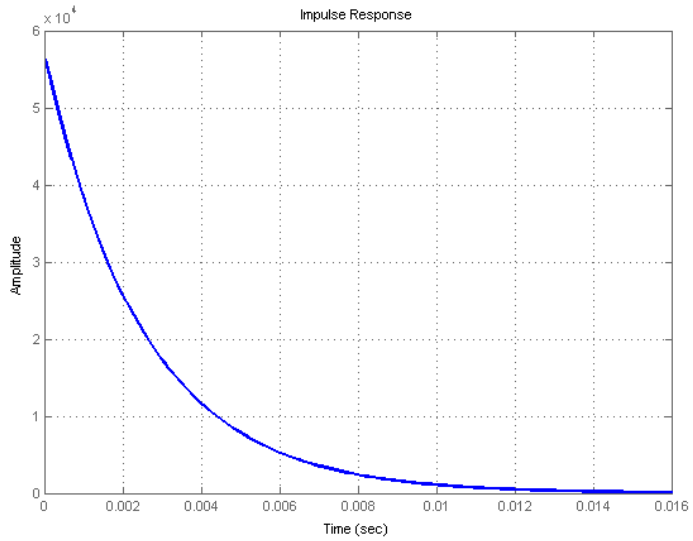

Figure 5.16: Natural response of the plant when applying an impulse input using the Control System Toolbox in Matlab.

The roots of the denominator of $G_p(s)$ gives two dominant poles:

$$s_{1,2} = -\frac{(RCr + L)}{2LRC} \pm \frac{1}{2LRC} \cdot \sqrt{(RCr + L)^2 - 4(r + 4)LRC} \tag{5.40}$$

Using the predefined parameter values, equation (5.40), produces two real negative poles, $s_1 = -948 \cdot 10^3$ and $s_2 = -396$. If one applies partial fraction expansion, where $p_1 = -s_1$ and $p_2 = -s_2$, it leads to:

$$\begin{aligned} \frac{\frac{V_{in}}{L}(s + \frac{1}{RC})}{(s + p_1)(s + p_2)} &= \frac{A}{s + p_1} + \frac{B}{s + p_2} \\ A &= \frac{\frac{V_{in}}{L}(-p_1 + \frac{1}{RC})}{-p_1 + p_2} = -20,1 \\ B &= \frac{\frac{V_{in}}{L}(-p_2 + \frac{1}{RC})}{-p_2 + p_1} = 56 \cdot 10^3 \end{aligned} \tag{5.41}$$

With two negative real poles and one zero, this is a second order *overdamped* system which natural response has the form: $Ae^{s_1 t} + Be^{s_2 t}$, in the time domain. Thus, the time domain solution of the natural response is given as:

$$f_n(t) = 56 \cdot 10^3 \cdot e^{-396t} - 20,1 \cdot e^{-948 \cdot 10^3 t}$$

One can easily see that $f_n(t)$ decays to zero as time reaches infinity. Furthermore, the time constants of the exponential decay is the reciprocal of the poles, $\tau_i = 1/s_i$. When comparing the amplitudes of the terms of $f_n(t)$, it is obvious that the first positive term is the dominant. The second negative term

has a small time constant compared with the first term, which result in a fast decay from the relative low amplitude value [34].

Of interest is also the boundary between the overdamped and the underdamped system. From (5.40) one can observe that the poles become equal when $\sqrt{(RCr+L)^2-4(r+4)LRC}=0$. The variable parameter in the system is the load R. Solving the boundary equation with respect to R, leads to two solutions, whereby $R=8,2\,\Omega$ is the physical realizable one. That is, the system becomes critically damped when $R=8,2\,\Omega$, and moves into an underdamped response if the load is higher then this value, i.e. the poles becomes complex conjugates. This is equivalent to a load ranging from $P_0=280\,W$[35] when the output voltage of the converter is $V_0=48\,V$, and $P_0=70\,W$ when $V_0=24\,V$. The nominal power rating of the converter is $P_{nom}=2\,kW$, so the boundary load values are at the outer operation region of the system. A test of the system response with $R=10\,\Omega$ applying a step input gives the result shown in figure 5.17. We see that the the response has an overshoot, characteristic of an underdamped response.

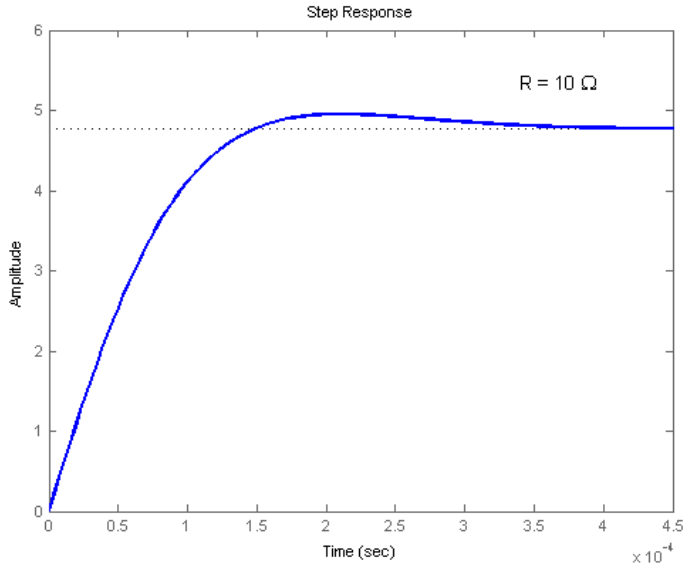

Figure 5.17: Underdamped response with $R=10\,\Omega$ when applying a step input, using CST in Matlab.

When formulating the control design for the system, the *steady state error*, as defined in (A.18), should be as small as possible. The real transducer used in the lab is $H(s)=0,01\,V/A$. That is, when the input is current(A), the transducer transforms the signal into a voltage, which can be interpreted by the PI-controller. Therefore, applying a unity step input to the system, means that the input to the transducer must be $100\,A$. When the steady state error is zero,

[34] Therefore, it is possible to approximate $f_n(t)$ as $f_n(t)\approx 56\cdot 10^3\cdot e^{-396t}$.
[35] $P_0=V_0^2/R$

the output equals the input, thus the response must reach a steady-state value of 100 A. Computing the closed loop response in the Laplace domain to a step input $R(s) = 1/s$ without any control [36] ,results in the response shown in figure 5.18.

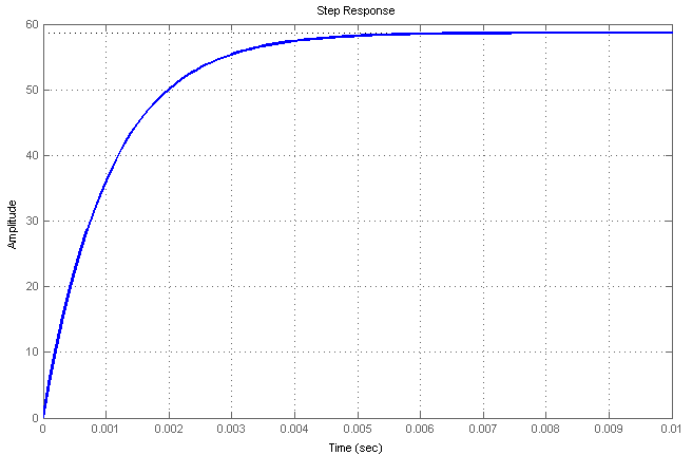

Figure 5.18: Simulated output of the system without control when applying a step input using CTS in Matlab.

From the plot in figure 5.18 we observe that the output reaches a steady state value at around $60A$. Hence, the steady state error is about 40 %.

The task is now to remove the steady state error by cascade PI-compensation. By using a PI-controller, the steady-state error can be removed without noteworthy effecting the transient response of the system. This is obvious when studying the error of the new closed loop system with the PI-controller. The transfer function for the controller is given by equation (5.37). Simplifying with $G_p(s) = \frac{N_p(s)}{D_p(s)}$ gives:

$$E(s) = \frac{R(s)}{1 + G_p(s)G_c(s)H(s)} = \frac{(1/s) \cdot D_p(s) \cdot s}{s \cdot D_p(s) + N_p(s)(K_i/K_p + s)K_pH(s)}$$

$$e(\infty) = \lim_{s \to 0} sE(s) = 0 \tag{5.42}$$

The pole at the origin in $G_c(s)$ has effectively removed the steady state error.

When picking the adequate values of K_i and K_p, the use of *frequency response analysis* of the open loop transfer function is advantageous. The open loop transfer function is given as: $G_{ol}(s) = G_c(s)G_p(s)H(s)$. A requirement for the system to be stable, is that the *phase margin* must be less than 180°, and the cross-over frequency, ω_c, should be in the order of a magnitude smaller than the switching frequency, $f_s = 20kHz$[37]. ω_c of the open loop system is a

[36] A step input represents a constant command, typically of the same form as the output. The step input test function capture both the transient response as well as the steady-state response[38].

[37] For a more detailed background, see Appendix A.1.

good indicator of the bandwidth, ω_{BW}, of the closed loop feedback system. The bandwidth determines the speed of the dynamic response of the control system to various disturbances. The higher the bandwidth, the shorter is the rise time and the settling time.

There exists now definitive formula for finding the adequate control parameters; it is based on a qualitatively analysis of the frequency response given the predefined requirements. After some testing, the following parameters was found to produce the desired response:

$$K_i = 600 \tag{5.43}$$

$$K_p = 10.2 \tag{5.44}$$

The bode-plot of the open loop response with these parameters can be seen in figure 5.19

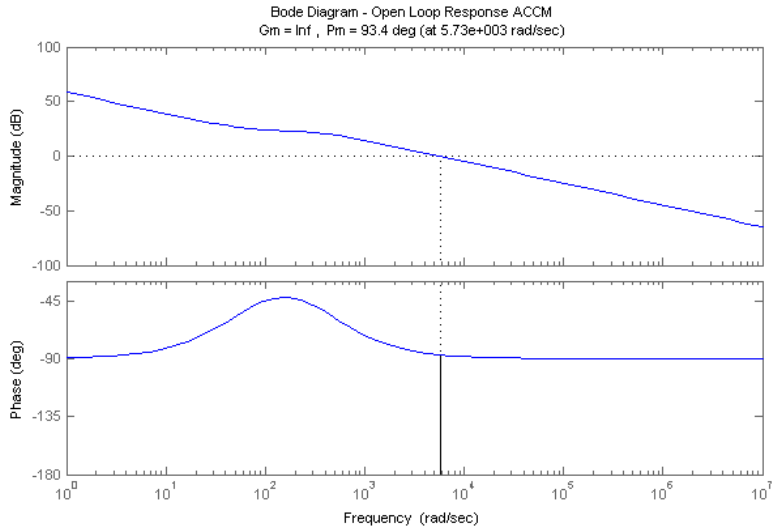

Figure 5.19: Frequency response: Bode-plot for $G_{ol}(s) = G_c(s)G_p(s)H(s)$ with $K_i = 600$ and $K_p = 10.2$.

The open loop frequency response results in a phase margin of $\phi_{PM} = 93,4°$and a cross-over frequency $\omega_c = 5,73 \cdot 10^3 rad/s = 912Hz$. Hence, the switching frequency, f_s, is approximately 20 times higher than ω_c, which is in accordance with the predefined requirements. Looking at the new step response of the closed-loop system gives the result shown in figure 5.20.

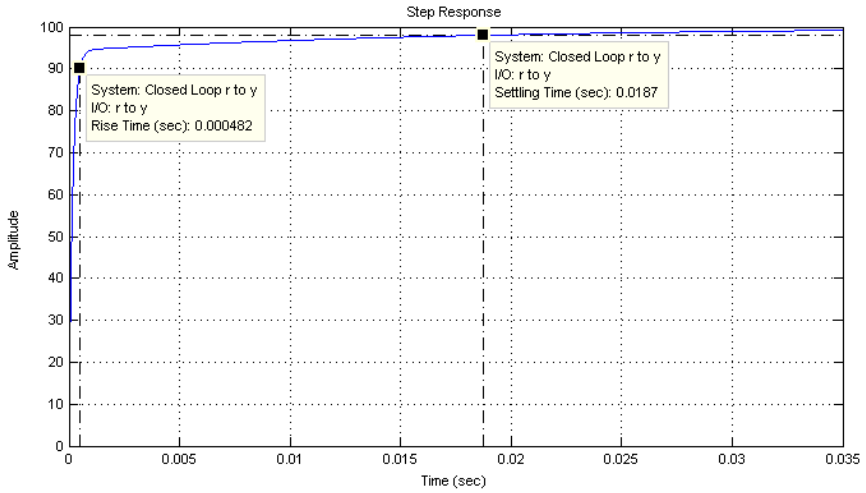

Figure 5.20: Step response for the closed loop $K_i = 600$ and $K_p = 10.2$.

The rise time is $T_r = 0,482ms$ and the settling time is $T_s = 18,7ms$. Thus, placing the PI-controller in cascade with the plant, has effectively eliminated the steady-state error and gives a satisfying transient response.

5.3.6 Modeling in Simulink

Based on the dynamic average model, the converter is formulated in Matlab/Simulink using the Simpower GUI. The model seen in figure A.13 in Appendix A.4, is build around a variable current source dependent on the calculated product of the duty cycle, d(t), and the inductor current, $i_L(t)$, and a variable voltage source dependent on the calculated product of the duty cycle, d(t), and the input voltage, $v_{in}(t)$.

6 Semi-Active Hybrid System

In the follwing the formulated control design is implemented in the semi-active topology shown in figure 2.3. The formulated topology formulated in Matlab/Simulink can be seen in figure A.12 in Appendix A.4. A simple control strategy based on power smoothing with moving average technique and over/under voltage protection is discussed and applied. Using Matlab/Simuling, the control strategy is simulated and compared with the PHS-topology. It is important to notice that the supercapacitor model used in this section is the former model, BMOD00165 from Maxwell Tech., because the converter was designed according to this model. Thus the simulations conducted here are not directly comparable to the simulations conducted in section 4.

6.1 Control strategies

6.1.1 Moving average

Moving average is an effective power smoothing control strategy that could remove fast transients in battery current and voltage. If P_{load} is the instantaneous power demanded by the load, then the moving averaged power, P_m, is defined as:

$$P_m = \frac{1}{T_m} \int_t^{t-T_m} P_{load}\, dt \tag{6.1}$$

Here is T_m the moving time window, that should be defined according to the frequency of the applied loading. P_m then represents the desired power profile of the battery. The current reference is then generated the following way. First, the calculated moving average power P_m is subtracted from the actual load power P_{load}, which defines the amount of power left that should be covered by the supercapacitor:

$$P_{sc,ref} = P_{load} - P_m \tag{6.2}$$

Second, the $P_{sc,ref}$ is divided by the measured instantaneous supercapacitor voltage V_{sc} to produce the current reference going to the controller:

$$I_{ref} = \frac{P_{sc,ref}}{V_{sc}} \tag{6.3}$$

I_{ref} is then sent to the controller where the measured inductor current I_L is subtracted, producing an error signal which is sent to the PI-controller. The formulated current reference generator in Matlab/Simulink can be seen in figure A.15 in Appendix A.4.

6.1.2 Over and under-voltage protection

The DC-bus/battery voltage could exceed the defined rated voltage of 48 V. If the state of charge of the supercapacitor is close to 100 %, this could lead to a supercapacitor terminal voltage above its rated voltage. This may eventually damage the supercapacitor. Therefore, there is a need to protect the supercapacitor from exceeding the rated voltage. It also necessary with an undervoltage protection at around half the rated voltage, since continuous discharging below

this boundary could degrade the supercapacitor performance over time.

One way to implement a control strategy for voltage protection in the Simulink-model, is to formalize a logic block that takes the state of charge of the supercapacitor, SoC_{sc}, and the load current, I_{load} as inputs, producing a dimensionless value, M, between zero and one, based on a set of rules. M can then be multiplied with current reference, I_{ref}, which leads the supercapacitor into different modes of operation depending on its state of charge and the type of loading present. The modified current reference is then:

$$I'_{ref} = M \cdot I_{ref} \tag{6.4}$$

The set of rules could be formulated as follows[7]:

$$M = \begin{cases} 0 & \text{if } I_{load} < 0 \text{ and } SoC_{sc} \geq 100\% \\ -20 \cdot SoC_{sc} + 20 & \text{if } I_{load} < 0 \text{ and } SoC_{sc} > 95\% \\ 1 & \text{if } 95\% < SoC_{sc} < 30\% \\ 20 \cdot SoC_{sc} - 5 & \text{if } I_{load} > 0 \text{ and } SoC_{sc} < 30\% \\ 0 & \text{if } I_{load} > 0 \text{ and } SoC_{sc} \leq 25\% \end{cases}$$

The set of rules is based on five operation regions. The first rule defines a hard upper limit, where M = 0 when $SoC_{sc} = 100\%$. The modified current reference becomes zero, preventing the supercapacitor to become overcharged. The second rule defines an upper transition region, where M smoothly decays to zero as SoC_{sc} goes from 95% towards 100 %. The values of the slope and the constant, here 20, gives the rate at which M changes in this region. The third rule defines the normal operation region where $M = 1$ and where $I'_{ref} = I_{ref}$. The fourth rule defines a lower transition region, according to the same principle as the upper transition region, while the fifth rule produces M = 0, when $SoC_{sc} < 25\%$.

However, it is not wanted that M = 0 at the lower limit, when the load is negative(netto energy transfer to the system). Regardless of SoC_{sc}, we want to use the supplied energy coming from the load to charge the supercapacitor. Therefore, when $I_{load} < 0$ and $SoC_{sc} < 25\%$, the logic block goes into rule three, producing $M = 1$.

In the same way, when the load is positive(netto energy transfer out of the system), we want the supercapacitor to discharge in order to assist the battery. Therefore, when $I_{load} > 0$ and $SoC_{sc} = 100\%$, the logic block goes into rule three, producing $M = 1$.

In figure A.16 in Appendix A.4 the formulation of the rule in Simulink can be seen.

6.2 Simulations

6.2.1 Results

In order to see the effect of the control strategy, the SAHS is simulated with a randomly changing load over a time window of 10 minutes. The moving average window is first set to $T_m = 60s$. The result of the simulation can be seen in figure 6.1.

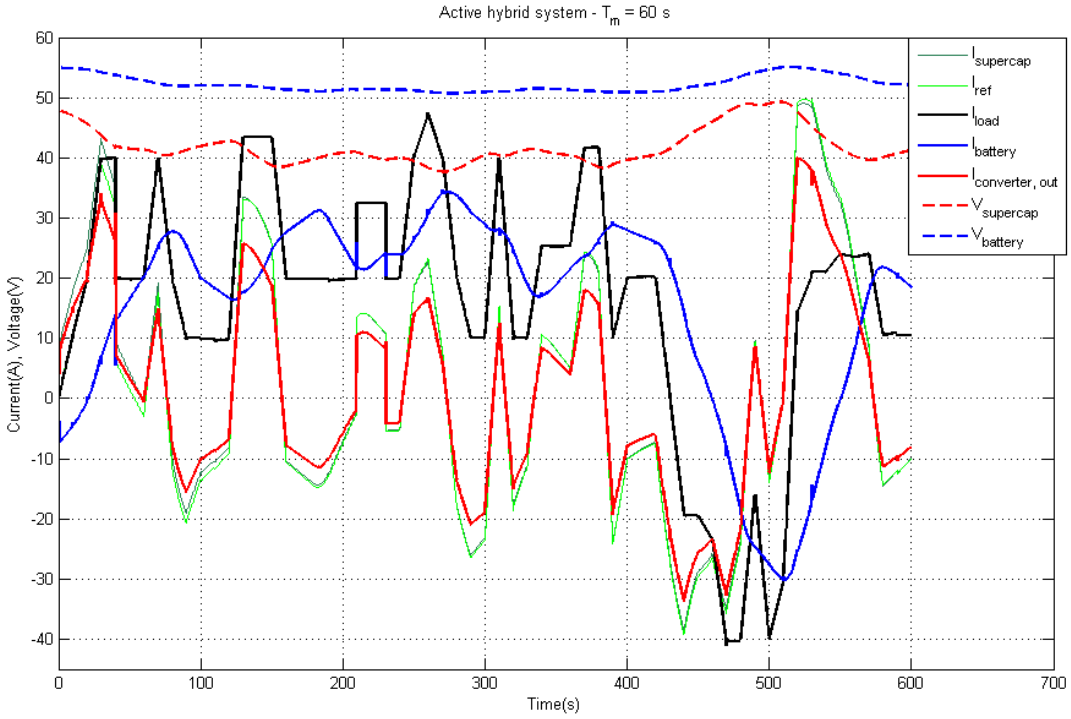

Figure 6.1: Simulation of the SAHS with fluctuating load. System currents and voltages as a function of time. $T_m = 60s$.

When $I_{load} > 0$, there is a net power demand and energy is transferred from the system to the load. When $I_{load} < 0$, net power is supplied from the load to the system. The current coming from the converter output on the battery side, $I_{converter,out}$, is added to the battery current, $I_{battery}$, represented by the solid blue line.

When adjusting the moving average time to $T_m = 120s$, gives the result shown in figure 6.2.

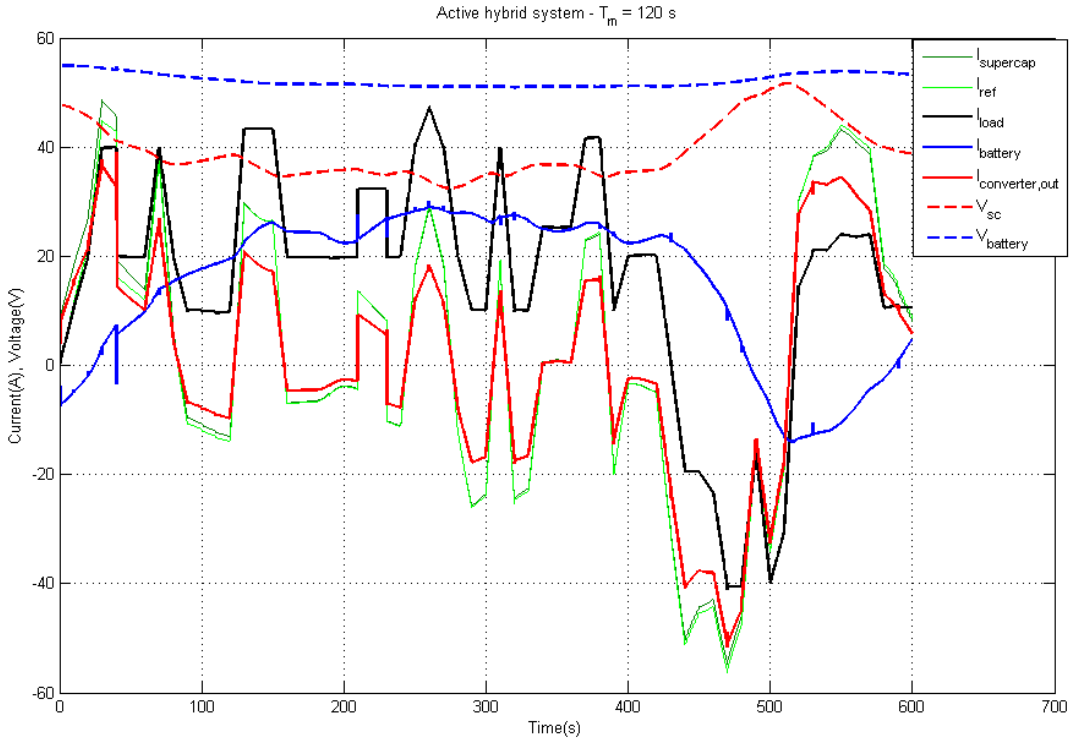

Figure 6.2: Simulation of the SAHS with fluctuating load. System currents and voltages as a function of time. $T_m = 120s$.

Exposing the passive hybrid system to the same load profile, gives the result presented in figure 6.3.

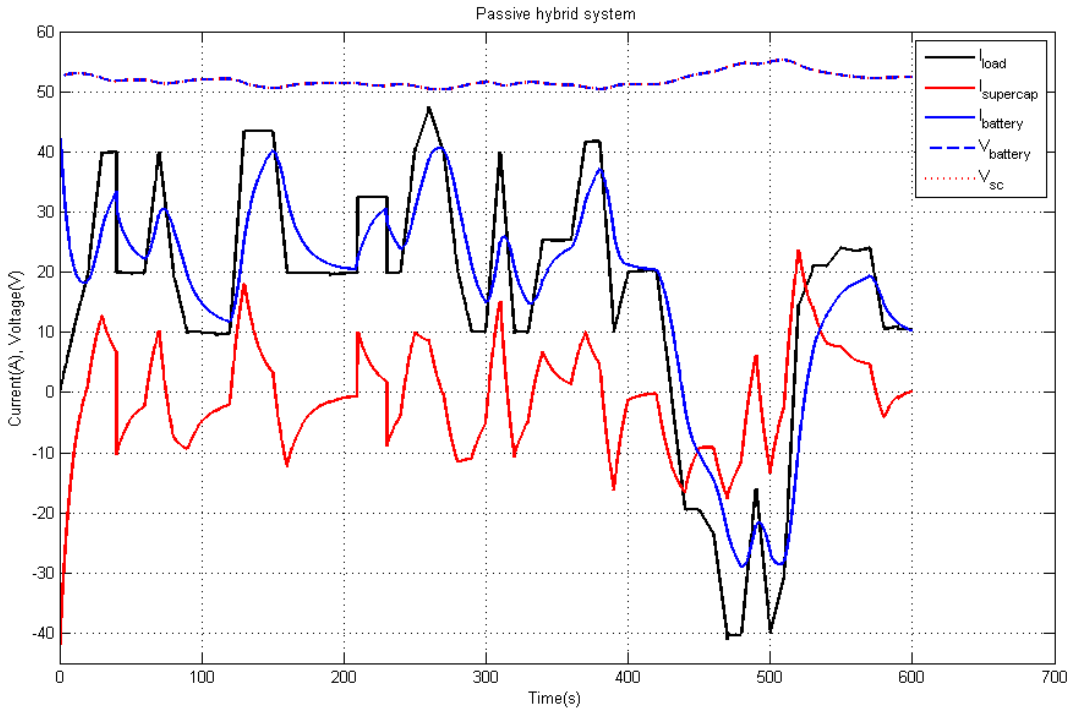

Figure 6.3: Simulation of the PHS with fluctuating load. System currents and voltages as a function of time

One way to compare the level of utilization of the supercapacitor in the PHS and the SAHS, is to compute the absolute value of the accumulated ampere-hours(amount of charge) going to and from the supercapacitor, in the semi-active and passive system respectively[38]. In order to observe the level of utilization of the battery, computing the accumulated ampere-hours directly, without taking the absolute value, gives the level of discharge of the battery in the given time window. The ampere-hours are calculated by integrating the currents, $I_{battery}$ and I_{sc}, over time. The accumulated ampere-hours as a function of time can be seen in figure 6.4.

[38]The absolute value is used, because the accumulated ampere-hours of the supercapacitor would be close to zero if SoC_{sc} is approximately unchanged in the given time window.

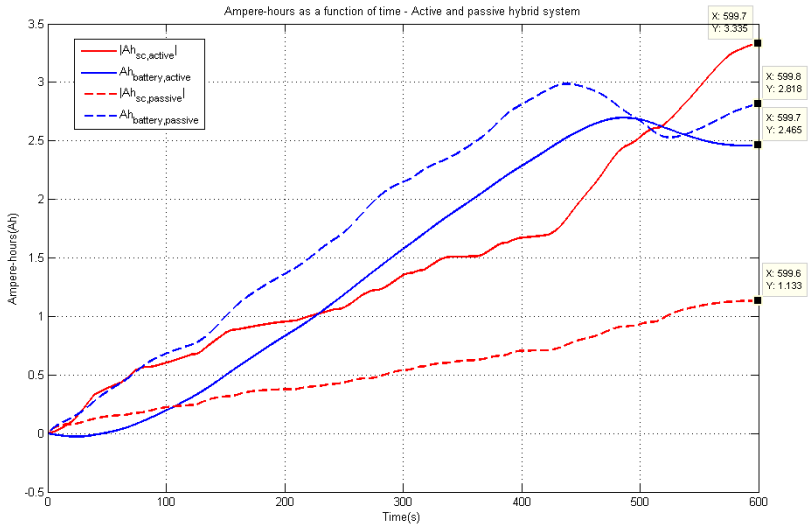

Figure 6.4: Accumulated ampere-hours as a function of time, for the SAHS and the PHS respectively. Calculated from simulation over 10 minutes modified simulation time with fluctuating load. Active system with $T_m = 120s$.

Exposing the SAHS to the same pulse train load that was used in the analysis of the passive hybrid system, we obtain the result seen in figure 6.5. The pulse period is T = 7,3 seconds and the duty cycle is D = 0,1. A moving average equal to the pulse period, $T_m = 7,3\,seconds$, is applied.

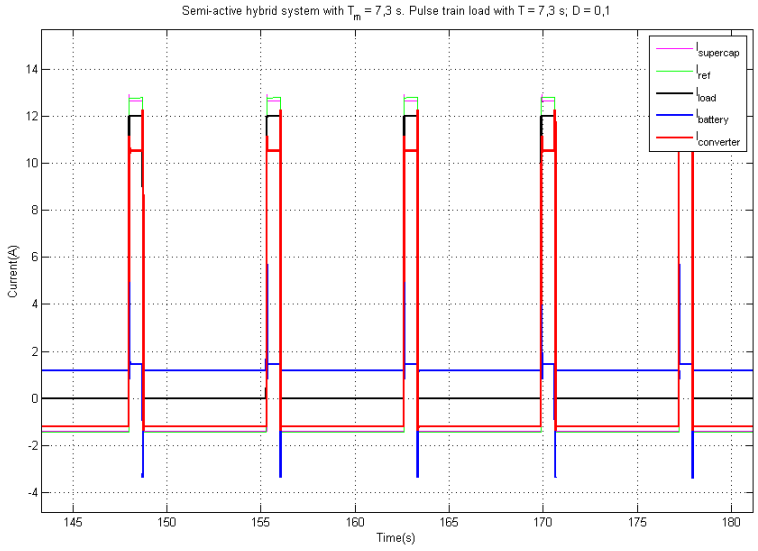

Figure 6.5: Exposing the SAHS to a pulse train load with T = 7,3 s and D = 0,1. Steady state operation. The moving average is set to $T_m = 7,3\,s$.

Given the same loading, the result of reducing the moving average to $T_m = 2\,seconds$ can be seen in figure 6.6.

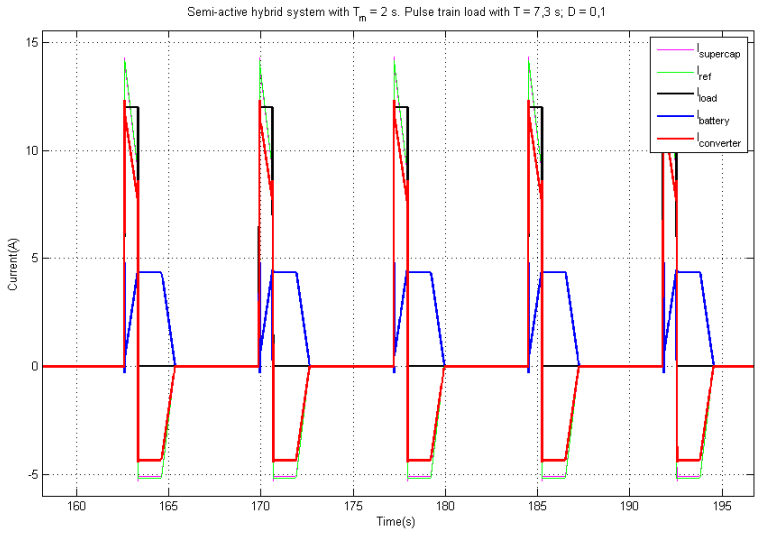

Figure 6.6: Exposing the SAHS to a pulse train load with T = 7,3 s and D = 0,1. Steady state operation. The moving average is set to $T_m = 2\,s$.

6.2.2 Discussion

The result of the simulation with $T_m = 60\,seconds$ in figure 6.1, shows that the converter output current, $I_{converter,out}$, and the battery current, $I_{battery}$, at all times during the simulation time are adding up to satisfy the demanded current from the load. The current flowing on the supercapacitor side of the converter, I_{sc}, is dictated by the generated current reference, I_{ref}. They follow the same trajectory in an adequate manner in the time window, except for a small deviation in the initial minute, because the system has not reached a steady state operation mode at this point. When $I_{converter,out}$ and I_{sc} is positive, the supercapacitor is discharging and the converter is in buck operation mode.

We observe that $I_{battery}$ initially is negative and that $I_{converter,out}$ is larger than I_{load}, so that at this stage the battery is being charged by the supercapacitor. After 60 seconds the moving average is catching up with the load, and $I_{battery}$ stabilizes around the moving average of the load. When $I_{battery}$ becomes larger than I_{load}, due to the 60 second delay in the moving average, $I_{converter,out}$ and I_{sc} becomes negative: the converter enters boost operation mode and the supercapacitor is thus being charged by the battery. The terminal voltage, $V_{battery}$, is kept stable with little ripple in the time window, while the supercapacitor terminal voltage, V_{sc}, fluctuates more.

When I_{load} becomes negative after 430 seconds, net power is transferred to the system, and both the supercapacitor and the battery are being charged. We observe that $V_{battery}$ and V_{sc} increases at this stage, hence, the state of charge of both the battery and the supercapacitor is increasing. The state of charge of the supercapacitor is at its minimum around 270 seconds, when $V_{sc} = 37,7V$, that is $SoC_{sc} = 63\%$. Hence, at no time in the time window is the supercapacitor being utilized to its fullest potential, i.e. utilizing up to 75% of its stored energy by discharging it close to $SoC_{sc} = 50\%$. This shows that the control strategy could be optimized more in order to utilize more of the supercapacitor's operation range.

As expected, using the same load profile and increasing the moving average to $T_m = 120\,seconds$, results in an increased utilization of the supercapacitor and an even more smoothed battery current, as can be seen in figure 6.2.

When the time intervals between the transients becomes shorter, the moving average time can be reduced.

When examining the simulation result from exposing the same load profile to the PHS in figure 6.3, we see that the battery immediately respond to the changes in the loading. However, because its internal resistance is relatively much larger than that of the supercapacitor, the supercapacitor respond faster, covering the instantaneous power demand. Hence, $I_{battery}$ is smoothed by the presence of the supercapacitor and the battery is protected from step changes in voltage and current.

In figure 6.4 the SAHS with $T_m = 120s$ and the PHS is compared by plotting the transferred ampere-hours to an from the supercapacitor and the discharged ampere-hours from the battery. As can be observed, the supercapacitor is obviously utilized to a greater extent in the SAHS, while the supercapacitor in the PHS is bounded by the system voltage, limiting its operation range.

We clearly see the effect of the control strategy. The supercapacitor in the SAHS charges and discharges $3,335\,Ah$ combined in the given time window, while the supercapacitor in the PHS charges and discharges only $1,133\,Ah$,

in the same time window. Hence, the supercapacitor in the active system is 2,5 times more utilized than supercapacitor in the PHS. We also see that the battery is more extensively utilized in the PHS. The amount of charge taken from the battery is slightly higher for the passive system, but this is due to the fact that SoC_{sc} at the end is lower in the SAHS. At all times the amount of charge removed from or transferred to the system must be equal to the charge demanded or supplied by the load.

When exposing the SAHS to the same pulse train load that was used in the analysis of the PHS, we observe that by using a moving average equal or longer than the pulse frequency, the ripple in the battery current is almoust reduced to zero. The battery is covering the average load over one pulse period, while the supercapacitor is covering the pulse load with a current sharing factor of almost 0,90. Such a high current sharing factor is difficult to achieve with the PHS that was analyzed in section 4. That would have required an unrealistic small internal supercapacitor resistance compared to that of the battery. However, because we apply a step change in the load and because of the delay in the controller reaction due to the settling time of 18,7 ms, we can observe that the battery experience a current transient in a short time interval as the load is applied or removed.

In figure 6.6 we observe the effect of reducing the moving average below the pulse frequency. The battery current ripple is significantly increased and the current sharing factor is reduced. Hence, this simple example shows that when applying a control strategy with moving average power smoothing technique, the moving average time window should be equal to or longer than the period of the applied load.

7 Conclusion

In this thesis we have seen that the supercapacitor possesses unique properties that can complement other energy storage technologies, such as batteries. Due to its fast charge and discharge capability, highly reversible process functionality, high power density, high recycleability and relatively small internal resistance it is an attractive alternative in hybrid electric energy systems.

An equivalent supercapacitor model was formalized based on electric characterization, which was used in simulations of both the passive hybrid system and the semi-active hybrid system. When characterizing the supercapacitor, a capacitance voltage dependency was detected, which is important to take into account, since it effects the eigen-frequency and time constant of the passive hybrid system. When conducting simulations of the passive hybrid system, it was found that the model probably should be simplified in order to adequately capture the system's short-term behavior under transient loading.

We have verified that the hybridization of batteries and supercapacitors is an effective solution for solving several optimization problems. The passive hybridization leads to the following system improvements:

- Reduced ripple of the battery voltage and current which mitigates transient charging and discharging. On a long-term basis this could prolong the battery lifetime
- Power enhancement: the power rating of the system is increased
- Power saving and higher system efficiency: the power losses in the system decreases due to the relative much smaller internal resistance of the supercapacitor
- Run time increase: the total run time of the hybrid system could be increased compared to a battery-alone system, especially at high peak power demand

Conducting experiments with the passive hybrid system in the REHYS-laboratory confirmed to a certain degree what was found in the analysis of the ideal system. Because the system performance is determined by the relative resistance between the supercapacitor branch and the battery branch, it is essential to minimize the parasitic resistances and inductances for optimal system performance.

The experiments showed that with a pulse load train with a frequency equal to the nominal eigen-frequency of the system, the voltage ripple could be reduced by approximately 60 % compared with the battery-alone system over all duty cycles. Still, this could be further improved by minimizing the parasitic impedances of the system set-up. The simulations showed that ideally the ripple could be reduced by up to 80 % given the same load conditions.

Regarding power enhancement, we found that when the pulse width of the applied load transient became very narrow, the passive hybrid system could in theory meet a pulse load amplitude up to nine times as large as the rated power of the battery. The experiments confirmed that the power rating of the system can be increased by hybridization, and when applying a pulse train with a frequency equal to the nominal eigen-frequency of the system with 10 % pulse

width, the system power rating increased 2,6 times in steady state operation. The power enhancement factor decreased with decreasing pulse frequency and increasing duty ratio.

It was found that when the system experiences randomly distributed transient peak power demand in time intervals longer then five time constants, the supercapacitor is fully recharged between each power transient and is able to cover a significant larger share of the demand than it can manage under a constant pulse train load in steady state. Overall, the higher the frequency of the pulse load train and the smaller the pulse width, the more the supercapacitor is utilized, relieving the battery of large voltage fluctuations and reducing the maximum battery current.

One drawback of the passive hybrid topology is the limited control possibilities, since the load current is shared between the battery and the supercapacitor in a nearly uncontrolled manner, determined predominantly by the internal impedances of the system. In the passive hybrid system the capacitance of the supercapacitor must be sufficiently large, since the system time constant is an important performance parameter. The time constant is directly proportional to capacitance and is determining for the peak power performance time of the supercapacitor. Because it is only possible to use a fraction of the stored energy of the supercapacitor, the supercapacitor is actually over-dimensioned in order to achieve the wanted system performance.

Applying a half-bridge DC/DC-converter between the supercapacitor and the battery/load-side in the semi-active hybrid topology, enabled us to control the current going to and from the supercapacitor. When modeling the converter, it was beneficial to represent the converter circuit as an average model in order to capture the converter performance under a dynamic regime. In the average representation of the converter, all the switching information is removed, which facilitates the simulation of the converter, making simulation going faster than by using the switch circuit design.

The semi-active topology opens up a range of additional possibilities and advantages:

- Expanding the operation range of the supercapacitor: voltage matching between the capacitor and the battery is no longer required which imply that it is possible to utilize a greater share of the energy stored in the supercapacitor
- Further enhancement of the power performance of the system
- The converter opens up for a range of control and management strategies that can be implemented in order to secure system stability.
- The performance and size of the supercapacitor can be optimized in order to reduce costs

Using a simple moving average power smoothing control strategy, it was confirmed through simulations that the operation range of the supercapacitor was expanded compared with the passive hybrid system. However, when applying a step change in the load, the simulation revealed a fast and relatively large current transient. The transient was caused by the delay in the controller reaction and this may also become a challenge when implementing the converter in the real system.

Although not examined in this thesis, an obvious drawback of the semi-hybrid topology is the additional costs associated with the converter, such as investment, service and maintainance costs. Also neglected in this thesis, is the additional converter power losses that also must be taken into account. Another drawback is the increased system complexity which could increase the chances of failure and system down-time. Combined, all these factors constitutes an essential optimization problem that eventually would be determining when choosing between a passive or an active system topology.

f(t)	**F(s)**	
$\Phi(t)$	$\frac{1}{s}$	unit step
$\Phi(t-\tau)$	$\frac{e^{\tau s}}{s}$	delayed unit step
$t \cdot \Phi(t)$	$\frac{1}{s^2}$	ramp
t^n	$\frac{n!}{s^{n+1}}$	$n \geq 0$
$e^{-at} \cdot \Phi(t)$	$\frac{1}{s+a}$	exponential decay
$cos(\omega t)$	$\frac{s}{s^2+\omega^2}$	
$sin(\omega t)$	$\frac{\omega}{s^2+\omega^2}$	

Table A.1: Laplace transforms of some frequently used functions.

A Appendices

A.1 Control design: fundamentals and definitions

A.1.1 Properties of the Laplace transform

The Laplace transform is a useful mathematical tool in solving differantial and integral equations. In physics and engineering it utilized in the analysis of linear time-invariant systems such as electrical circuits, harmonic oscillators, optical devices and mechanical systems. The Laplace transform is often interpreted as a transformation from the time-domain, in which inputs and outputs are functions of time, to the frequency-domain, where the same inputs and outputs are functions of complex angular frequency. The Laplace transform is defined as[38]:

$$F(s) = \mathscr{L}\{f(t)\} = \int_0^\infty e^{-st} f(t) dt \tag{A.1}$$

where F(s) a function in the frequency domain and the Laplace transform of the function f(t) in the time domain. The parameter s is a complex number that can be expressed as:

$$s = \sigma + i\omega \tag{A.2}$$

In table A.1 some of the frequently used Laplace transforms are presented.

Two important theorems concerning Laplace transform is the final value theorem:

$$f(\infty) = lim_{s \to 0} sF(s) \tag{A.3}$$

and the initial value theorem:

$$f(0+) = lim_{s \to \infty} sF(s) \tag{A.4}$$

A.1.2 Transfer function

In an engineering perspective it is possible to formulate mathematical models that describe the relationship between input, r(t), and output, c(t), of dynamic physical systems. One such model, that is frequently used, is the linear, time invariant differential equation[38]:

$$a_n \frac{d^n c(t)}{dt^n} + a_{n-1} \frac{d^{n-1} c(t)}{dt^{n-1}} + ... + a_0 c(t) = b_m \frac{d^m r(t)}{dt^m} + b_{m-1} \frac{d^{m-1} r(t)}{dt^{m-1}} + ... + b_0 r(t) \tag{A.5}$$

where the coefficients a_i and b_i and the form of the equation represent the dynamic system of interest. Taking the Laplace transform of equation (A.5), leads to an purely algebraic expression[38]:

$$\begin{aligned} a_n s^n C(s) \quad + \quad a_{n-1} s^{n-1} C(s) \quad + \quad ... \quad + \quad a_0 C(s) \quad + \quad \text{intitial cond.} \\ = b_m s^m R(s) + b_{m-1} s^{m-1} R(s) + ... + b_0 R(s) + \text{initial cond.} \end{aligned} \tag{A.6}$$

If we assume that *all initial conditions are zero* and express equation (A.6) as the ratio between the output, C(s), and input the output, R(s), we obtain[38]:

$$\frac{C(s)}{R(s)} = G(s) = \frac{a_n s^n + a_{n-1} s^{n-1} + ... + a_0}{b_m s^m + b_{m-1} s^{m-1} + ... + b_0} \tag{A.7}$$

This ratio, G(s), is defined as the *transfer function* of the dynamic system. It can be represented in a signal flow block diagram, shown in figure A.1.

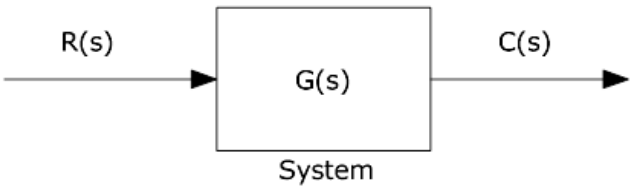

Figure A.1: Block diagram of the transfer function.

A.1.3 Zeros and poles

The *poles* of a transfer function are the values of the Laplace transform variable, s, that cause the transfer function to become infinite. The *zeros* of a transfer function are the values of the Laplace transform variable, s, that cause the transfer function to become zero[38].

A pole in the input function generates the form of the forced response. For example, a pole at the origin generates a step function at the output. A pole in the transfer function generates the form of the natural response. A pole on the real axis generates an exponential response of the form $e^{-\alpha t}$, where $-\alpha$ is the pole location on the real axis. This means that the further to the left a pole is on the negative real axis, the faster the exponential transient response(natural) will decay to zero. The zeros and poles generate the amplitudes for both the forced and natural responses.

A.1.4 Second order system

The transfer function of a general 2^{nd}-order system with unit steady state response, can be written as follows[38]:

$$G(s) = \frac{\omega_n^2}{s^2 + 2\zeta\omega_n s + \omega_n^2} \tag{A.8}$$

The poles of the system can be formulated as: $s_{1,2} = -\zeta\omega_n \pm \omega_n\sqrt{\zeta^2 - 1}$. In the s-plane the poles can be located in the s-plane as shown in figure A.2.

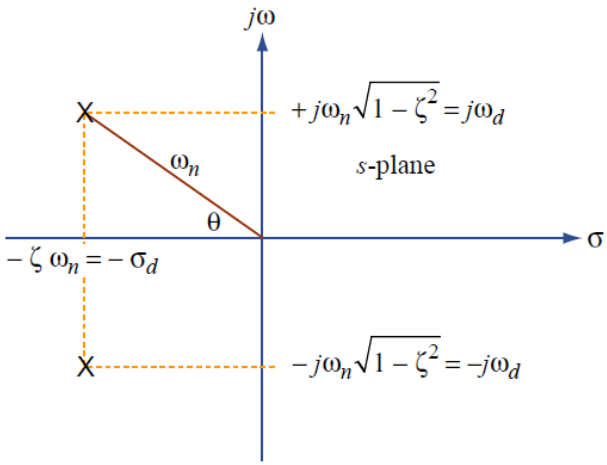

Figure A.2: Pole location in the s-plane[37].

Using the Pythagorean theorem, one can see from figure A.2 that the radial distance from the origin to the pole is equal to the natural frequency ω_n and that $cos\theta = \zeta$. $\omega_d = \omega_n\sqrt{\zeta^2 - 1}$ is called the damped frequency of oscillation, and the real pole σ_d is the exponential damping frequency. The natural frequency, ω_n, indicates the oscillation frequency of the undamped("natural ") system, i.e. the system with energy storage elements only and without any dissipative elements. The damping ratio ζ denotes the relative contribution to the system dynamics by energy storage elements and dissipative elements. The quantity ζ compares the exponential decay frequency to the natural frequency and is defined as[38]:

$$\zeta = \frac{\text{Exponential decay frequency}}{\text{Natural frequency(rad/sec)}} = \frac{|\sigma|}{\omega_n} \tag{A.9}$$

If $\zeta^2 < 1$, the pole becomes a complex conjugates on the form $s = \sigma_d \pm j\omega_d$. If $\zeta = 0$, the pole becomes purely imaginary. From the type of poles present in the transfer function denominator, the system's response to a step input can be categorized into[38][37]:

- overdamped if the poles are on the negative real axis, $s = -\sigma_1, -\sigma_2, \zeta > 1$
- underdamped if the poles are complex conjugate, $s = -\sigma_d \pm j\omega_d, 0 < \zeta < 1$

- undamped if the poles are purely imaginary, $s = \pm j\omega_1$, $\zeta = 0$,
- critically damped if the poles are multiple, $s = -\sigma_1$, $\zeta = 1$

An overdamped system absorbs a large amount of energy(damping/resistors), which inhibits the transient response from overshooting and oscillating about the steady state value for a step input. If the energy absorption is reduced, the system will eventually become underdamped[38]. Critically damped responses are the fastest possible without the overshoot that is characteristic of the underdamped response.

The types of responses in the time domain of a general 2^{nd}-order system can be seen in figure A.3.

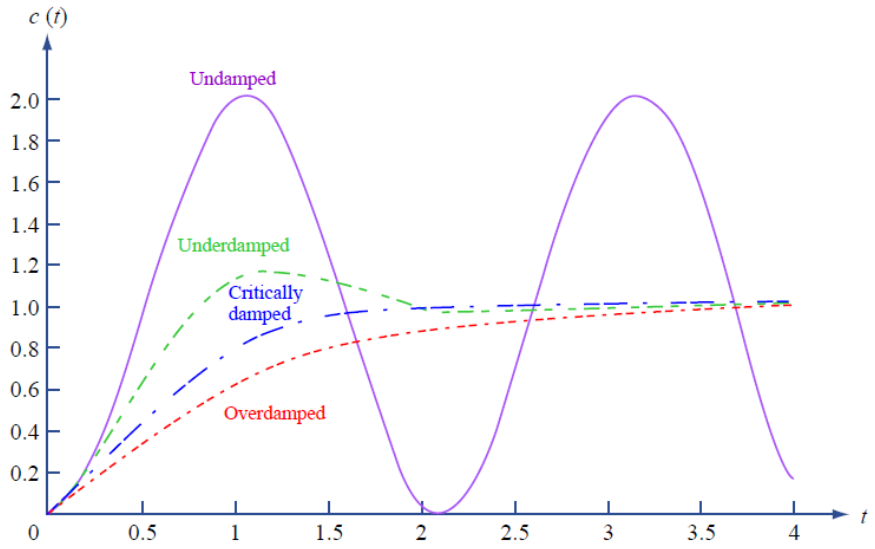

Figure A.3: Types of responses in a general 2^{nd}-order system [37].

The transients in an underdamped 2^{nd}-order system can be defined according to the peak time, T_p, the percent overshoot, $\%OS$, and the settling time, T_s. The peak time is defined as the time it takes before the response reaches is first maximum:

$$T_p = \frac{\pi}{\omega_n\sqrt{1-\zeta^2}} = \frac{\pi}{\omega_d} \tag{A.10}$$

The percent overshoot is the amount the response overshoots the steady-state value at the peak time. It is defined as:

$$\%OS = exp(-\frac{\zeta\pi}{\sqrt{1-\zeta^2}}) \times 100\% \tag{A.11}$$

Settling time is defined as the time required for the transient's oscillations to reach and stay within $\pm 2\%$ of the steady-state value:

$$T_s = -\frac{ln(0.02\sqrt{1-\zeta^2})}{\zeta\omega_n} \approx \frac{4}{\zeta\omega_n} = \frac{\pi}{\sigma_d} \tag{A.12}$$

where the approximation is valid for $0 < \zeta < 0,9$. It makes sense that the settling time T_s is inversely proportional to the real part of the pole,$sigma_d$, which is equal to the inverse of the time constant of the envelope decaying exponential, and that the peak time is inversely proportional to the imaginary part of the pole, which is equal to the oscillation frequency of the sinusoidal produced by the underdamped response[38].

The *rise time*, T_r, is defined as the time required for the response to go from 10% of it's steady-state value to 90% of it's steady-state value. A precise analytical relationship between rise time and damping ratio cannot be derived[38].

System response with zeros The zeros of a response affect the amplitude of a response component, but do not affect the nature of the response, i.e. if it is exponential, damped sinusoid and so on. The closer the zero is to the dominant poles, the greater is its effect on the transient response. As the zero moves away form the dominant poles, the response approaches that of the two-pole system.

A.1.5 Block diagrams

Block diagram algebra An individual, linear, time invariant system with its inherent transfer function, $G(s)$, may be represented as a block with an output signal $C(s)$ and an input signal $R(s)$, as seen in figure A.4b). Many systems are composed of multiple subsystems. Interconnection of these subsystems gives rise to *summing junctions* and *pickoff points*. The *summing junction* seen in figure A.4c) transmit an output signal, $C(s)$, which is the algebraic sum of the input signals $R_1(s)$, $R_2(s)$ and $R_3(s)$. A *pickoff point* seen in figure A.4d), distributes the input signal $R(s)$, undiminished, to several output points.

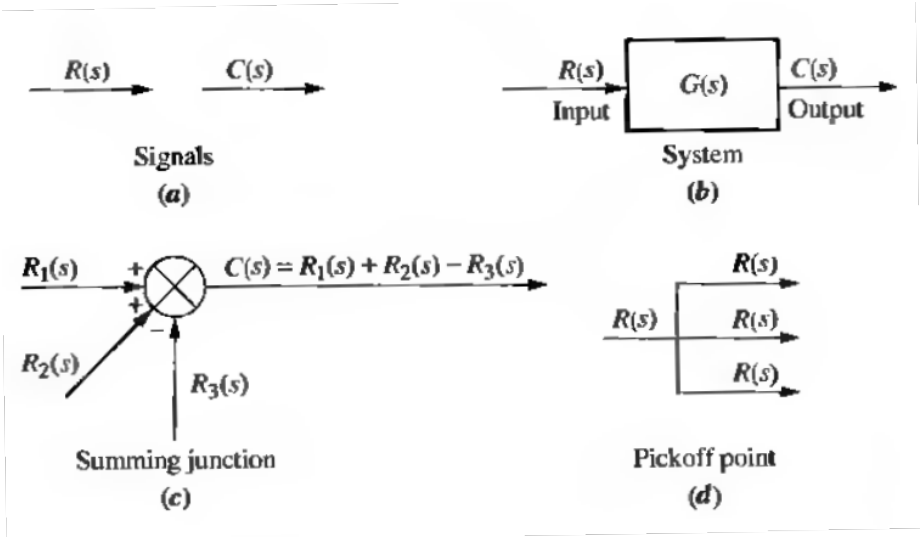

Figure A.4: Components of a block diagram for a linear, time-invariant system[38].

Subsystems may be connected in series or cascade form, where each signal is derived from the product of the input times the transfer function. This configuration can be seen in figure A.5. The equivalent transfer function, $G_e(s)$, is simply the output Laplace transform divided by the input Laplace transform:

$$G_e(s) = G_3(s)G_2(s)G_1(s) \tag{A.13}$$

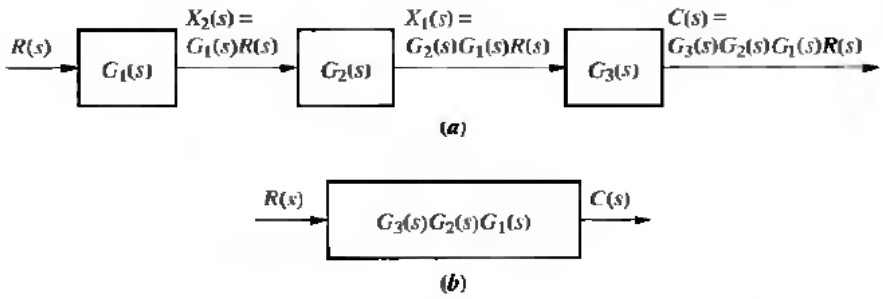

Figure A.5: a) Cascaded subsystems b) The equivalent transfer function as a multiple of the individual transfer functions[37].

If subsystems are connected in parallel form, they have a common input and an output formed by the algebraic sum of the outputs from all the subsystems. Then the equivalent transfer function, $G_e(s)$, becomes:

$$G_e(s) = \pm G_3(s) \pm G_2(s) \pm G_1(s) \tag{A.14}$$

Open loop and closed loop systems The two main configurations of control systems is the *open loop system* and the *closed loop system*. Generally the configurations consists of a *plant*, which is the system that is to be controlled, a *controller*, which is the apparatus that produces the input to the plant, and *transducers* that convert the signals so that it can be interpreted by the controller[39].

An *open loop system*, seen in figure A.6, consists typically of an input transducer that transforms the input signal, often referred to as the *reference*. The converted input is sent to the controller which drives the *plant*. The resulting plant output is referred to as the *controlled variable*. The system can be subjected to external disturbances that are added to the original signal flow. The distinguishing characteristic of the open loop system is therefore that it cannot compensate for the disturbances that add to the controller signal. This means that an open loop system can not correct for the disturbances and the actual output may deviate a great deal from the desired output when subjected to external disturbances[40].

[39]Transducers could for example be potentiometers converting an input position into a voltage, a thermistor that converts a temperature into a voltage, a tachometer that converts a velocity into a voltage. The transducer could also be a simple gain that boosts up or bucks down the signal going to the controller[37][38].

[40]Typical open loop systems are washing machines, audio speakers, or simple mechanical systems such as mass-spring-damper systems.

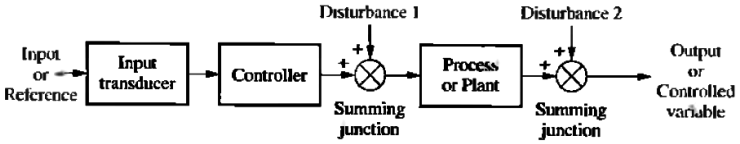

Figure A.6: Open loop system[38].

The *closed loop system*, shown in figure A.7, mitigate the problem of sensitivity to disturbances by a *feedback path* going from the output back to the input through a summing junction. In the summing junction the output signal is normally subtracted from the input reference signal producing an error signal which is the difference between the input and the output signals. When the error is nonzero, the control system drives the plant to make a correction. When the error is zero, the control system does not drive the plant since the response already is the desired response, namely the reference input. The closed loop system compensates thereby for the external disturbances and effectively stabilizes the system performance.

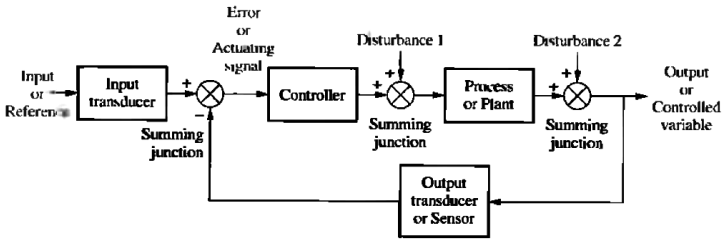

Figure A.7: Closed loop system[38].

Expressing the closed loop system with negative feedback in terms of transfer functions and signals in the Laplace domain, results in a block diagram shown in figure A.8.

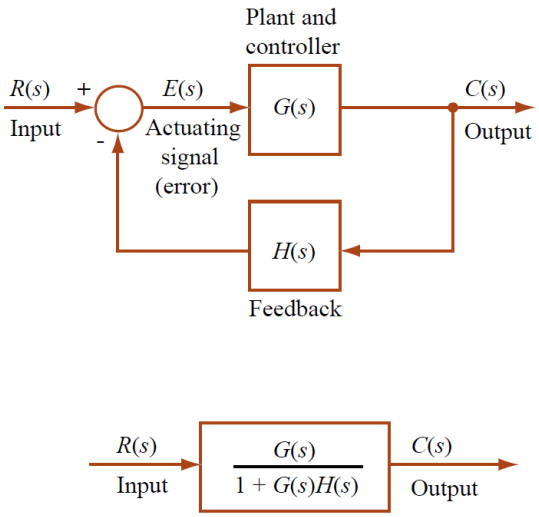

Figure A.8: Above: Block diagram showing feedback topology in the Laplace domain. Below: Equivalent block diagram for closed loop transfer function [37].

Using the block diagram algebra, the error signal can be expressed as:

$$E(s) = R(s) - H(s)C(s)$$

The output signal is given by:

$$C(s) = E(s)G(s)$$

The closed loop transfer function is then defined as:

$$G_{closedloop}(s) = \frac{C(s)}{R(s)} = \frac{G(s)}{1 + G(s)H(s)} \tag{A.15}$$

The open loop transfer function, or the loop gain without feedback path, is defined as:

$$G_{openloop}(s) = G(s)H(s) \tag{A.16}$$

A.1.6 Stability

> *Definition*: A linear, time-invariant system is stable if the natural response approaches zero as time approaches infinity(poles on negative real axis)[38].

Stability is the most important system specification. A system is unstable if the natural response grows without bound as time approaches infinity(poles on positive real axis). Likewise, a system is marginally stable if the natural response neither decays or grows, but remains constant or oscillate as time approaches infinity. An alternative definition of an unstable system is: A system is unstable if any bounded input yields an unbounded output.

A.1.7 Steady state error

The *steady state error*, $e(\infty) = e_{ss}$, is defined as the difference between the input and the output for a prescribed test input as time reaches infinity[38]. That is, the difference between output and input after the transients have effectively disappeared. Applying the final value theorem (A.3) gives:

$$e(\infty) = lim_{t\to\infty}[r(t) - c(t)] = lim_{s\to 0}s[R(s) - C(s)] = lim_{s\to 0}sE(s) \quad \text{(A.17)}$$

Hence, the concept of steady state error is only meaningful when the system is stable, i.e. the natural response of the system decays to zero as time reaches infinity[41].

From the diagram shown in figure A.8 one can see that $C(s) = G(s)E(s)$. Using this relationship together with the closed loop transfer function, (A.15), with feedback gain $H(s)$, gives:

$$E(s) = \frac{R(s)}{1 + G(s)H(s)}$$

Applying the final value theorem (A.3) leads to:

$$e(\infty) = lim_{s\to 0}sE(s) = lim_{s\to 0}\frac{sR(s)}{1 + G(s)H(s)} \quad \text{(A.18)}$$

Given a unity feedback gain $H(s) = 1$ and given a stable system, applying a step input test function $R(s) = 1/s$ results in:

$$e(\infty) = lim_{s\to 0}\frac{s(1/s)}{1 + G(s)} = \frac{1}{1 + \frac{lim}{s\to 0}G(s)} \quad \text{(A.19)}$$

The term $\frac{lim}{s\to 0}G(s)$ is called the *dc-gain* of the forward transfer function, since s, the frequency variable, approaches zero. One sees from (A.19) that in order to have a zero steady-state error, the dc-gain must approach infinity. This means that the denominator in $G(s)$ must approach zero as s goes to zero, i.e. at least one pole of $G(s)$ must be at the origin[38]. A pole at the origin in the Laplace frequency domain, is the same as an integration in the time domain. If $\frac{lim}{s\to 0}G(s)$ is finite, then there will be a non-zero steady-state error when applying a step input. From this, a classification of different *system types* can be formulated based on the number of pure integrations(poles at the origin) in the forward path transfer function:

- *Type 0* systems has no poles at the origin.
- *Type 1* systems has one pole at the origin
- *Type 2* systems has two poles at the origin

[41] i.e. All poles of the transfer function are in the second quadrant of the s-plane or at the origin.

A.1.8 Frequency response

The *frequency response* is a representation of the system's response to sinusoidal input test function at varying frequencies[38]. Although these responses are of the same frequency as the input, they differ in amplitude and phase angle from the input. These differences are functions of frequency. The frequency response analysis techniques are in general mathematical representations of physical *delays* in system, due to the configuration of the plant, the control and the feedback path. These delays can lead to system instability, when the system response becomes unbounded when applying a bounded input.

Sinusoids with amplitude M_i, angular frequency ω_i and phase angle ϕ_i can be represented in the complex plane as a phasor:

$$M_i \cdot sin(\omega_i t + \phi_i) \rightarrow M \cdot e^{j(\omega_i t + \phi_i)} \rightarrow M_i \cdot e^{j\phi_i} \rightarrow M_i \angle \phi_i \tag{A.20}$$

where the phasor rotates with a constant angular frequency in the complex plane around origo. Given an input sinusoid $R = M_i(\omega)\angle\phi_i(\omega)$ and a system represented with the transfer function $G = M(\omega)\phi(\omega)$, the output can be formulated as:

$$M_o(\omega)\angle\phi_o(\omega) = M_i(\omega)M(\omega)\angle[\phi_i(\omega) + \phi(\omega)] \tag{A.21}$$

The *magnitude frequency response* is then given by:

$$M(\omega) = \frac{M_o(\omega)}{M_i(\omega)} \tag{A.22}$$

and the *phase frequency response* is:

$$\phi(\omega) = \phi_o(\omega) - \phi_i(\omega) \tag{A.23}$$

The overall frequency response of a system with transfer function $G(s)$ can then be expressed as:

$$G(j\omega) = M_G(\omega)\angle\phi_G(\omega) \tag{A.24}$$

The frequency response can be represented graphically in several ways. In the *Bode-plot* the magnitude response and the phase angle response are plotted separately. The magnitude is plotted in decibels(dB) versus the logarithm of the frequency. The magnitude in decibels is defined as:

$$dB = 20 \cdot log_{10}(M) \tag{A.25}$$

Likewise, the phase angle response is plotted versus the logarithm of the frequency[42].

The *crossover frequency* f_c is defined as the frequency at which the gain equals unity, that is when the magnitude of the loop transfer function $|G_L(s)| = 0\,dB$. f_c is a good indicator of the bandwidth, ω_{BW}, of the closed-loop feedback

[42]For example, if the transfer function for a system is $G(s) = \frac{1}{s+2}$, then the frequency response is given as $G(j\omega) = \frac{1}{(j\omega+2)} = \frac{(2-j\omega)}{\omega^2+4}$. The magnitude of the frequency response is $|G(j\omega)| = M(\omega) = \frac{1}{\sqrt{(\omega^2+4)}}$. The phase angle response is given by $\phi(\omega) = \frac{Im(G(j\omega))}{Re(G(j\omega))} = -arctan(\omega/2)$

system, which determines the speed of the dynamic response of the control system to various disturbances[**?**]. ω_{BW} is defined as the frequency at which the magnitude response curve is $3\,dB$ down from its value at zero frequency, and is related to the settling time T_s by the equation:

$$\omega_{BW} = \frac{4}{T_s} f(\zeta) \tag{A.26}$$

That is, given a given a constant damping ratio ζ, the bandwidth is inversely proportional to the settling time: the larger the bandwidth, the smaller the settling time and the faster the response.

The stability of a system can be formulated based on the so-called *Nyquist-criterion*[38]. From the Nyquist-criterion the *phase margin* is defined as the change in open loop shift required to make the system unstable. It is given as the difference in degrees between $-180°$ and the phase angle of $\angle G_L(s)$ at the crossover frequency f_c[**?**]:

$$\phi_{PM} = \angle G_L(s)|_{f_c} - (-180°) = \angle G_L(s)|_{f_c} + 180° \tag{A.27}$$

The *gain margin* is defined as the change in open loop gain required to make the system unstable, and is usually given as the difference in gain between the gain at which $\angle G_L(s) = -180°$ and 0 dB[43]. If the phase angle crosses $-180°$, the gain margin should generally be in excess of 10 dB in order to keep the system response from becoming oscillatory due to parameter changes and other variations. Figure A.9 shows a typical bode plot consisting of magnitude and phase angle, with the definitions of gain margin and phase margin pointed out.

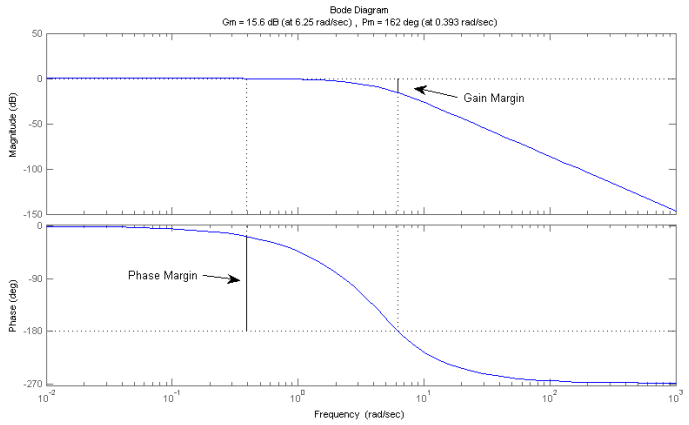

Figure A.9: Example of a typical Bode-plot with the phase margin and gain margin indicated.

Feedback controllers should in general be designed to yield a phase margin of approximately 60°. Smaller values results in high overshoots and long settling times(oscillatory).

A system is stable if both the phase margin and the gain margin is positive.

[43]This is not always the case, and hence not a definition.

A.2 Passive Hybrid System: Derivation of internal voltage drop

In section 4.1.1 we want to transform the internal voltage drop $V_i(s)$ back into the time domain. The internal voltage drop $V_i(s)$ with the given load form I_0 is given by:

$$V_i(s) = Z_{Th} I_0(s)$$

$$= \frac{R_c R_b}{R_b + R_c} \frac{s+\alpha}{s+\beta} I_0 \sum_{k=0}^{N-1} [\frac{e^{-kT\cdot s}}{s} - \frac{e^{-(k+D)T\cdot s}}{s}]$$

$$= \frac{R_c R_b}{R_b + R_c} I_0 \sum_{k=0}^{N-1} [\frac{e^{-kT\cdot s}}{(s+\beta)} + \frac{\alpha e^{-kT\cdot s}}{(s+\beta)s} - \frac{e^{-(k+D)T\cdot s}}{(s+\beta)} - \frac{\alpha e^{-(k+D)T\cdot s}}{s(s+\beta)s}] \quad \text{(A.28)}$$

Taking the Laplace inverse of each term inside the brackets of (A.28) yields[44]:

$$\frac{e^{-kT\cdot s}}{(s+\beta)} \rightarrow e^{-\beta(t-kT)}\Phi(t-kT)$$

$$\frac{\alpha e^{-kT\cdot s}}{(s+\beta)s} \rightarrow \frac{\alpha}{\beta} - \frac{\alpha}{\beta} e^{-\beta(t-kT)}\Phi(t-kT)$$

$$\frac{e^{-(k+D)T\cdot s}}{(s+\beta)} \rightarrow e^{-\beta(t-(k+D)T)}\Phi(t-(k+D)T)$$

$$\frac{\alpha e^{-(k+D)T\cdot s}}{(s+\beta)s} \rightarrow \frac{\alpha}{\beta} - \frac{\alpha}{\beta} e^{-\beta(t-(k+D)T)}\Phi(t-(k+D)T)$$

The internal voltage drop is then given by:

$$v_i(t) = \frac{R_c R_b}{R_b + R_c} I_0 \sum_{k=0}^{N-1} [(e^{-\beta(t-kT)} + \frac{\alpha}{\beta} - \frac{\alpha}{\beta} e^{-\beta(t-kT)}) \cdot \Phi(t-kT)$$

$$-(e^{-\beta(t-(k+D)T)} + \frac{\alpha}{\beta} - \frac{\alpha}{\beta} e^{-\beta(t-(k+D)T)}) \cdot \Phi(t-(k+D)T)]$$

which simplifies to:

$$v_i(t) = R_b I_0 \sum_{k=0}^{N-1} \{(1 - \frac{R_b}{R_b + R_c}(e^{-\beta(t-kT)}) \cdot \Phi(t-kT)$$

$$-(1 - \frac{R_b}{R_b + R_c} e^{-\beta(t-(k+D)T)}) \cdot \Phi(t-(k+D)T)\} \quad \text{(A.29)}$$

[44]The exponential terms in the Laplace domain indicate a time delay in the time domain. That means that a exponential in a term, becomes a delayed unit step function that has to be multiplied by the fundamental expression derived for the time domain. This can be expressed on the general form: $\frac{e^{-\tau s}}{(s+\alpha)^{n+1}} \rightarrow \frac{(t-\tau)^n}{n!} e^{-\alpha(t-\tau)} \cdot \Phi(t-\tau)$, where τ is the time delay.

A.3 Variable capacitance for BMOD0130

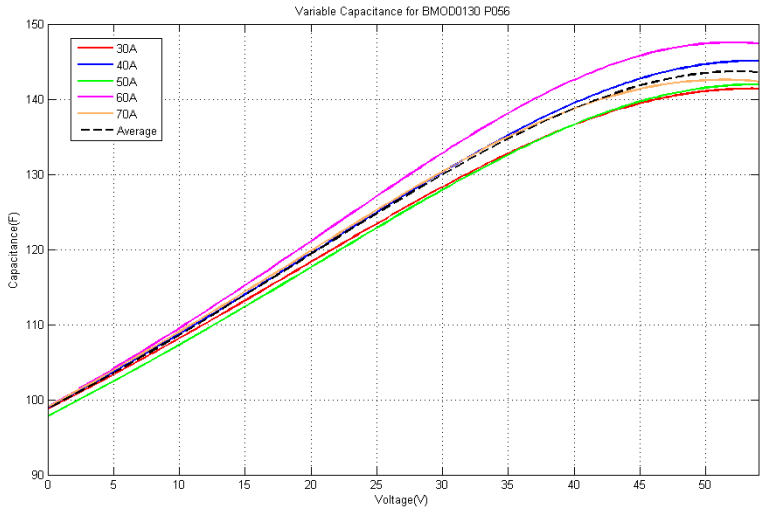

Figure A.10: Calculated voltage dependent capacitances at different currents for BMOD0130. The dashed black curve is the average.

A.4 Matlab/Simulink - models

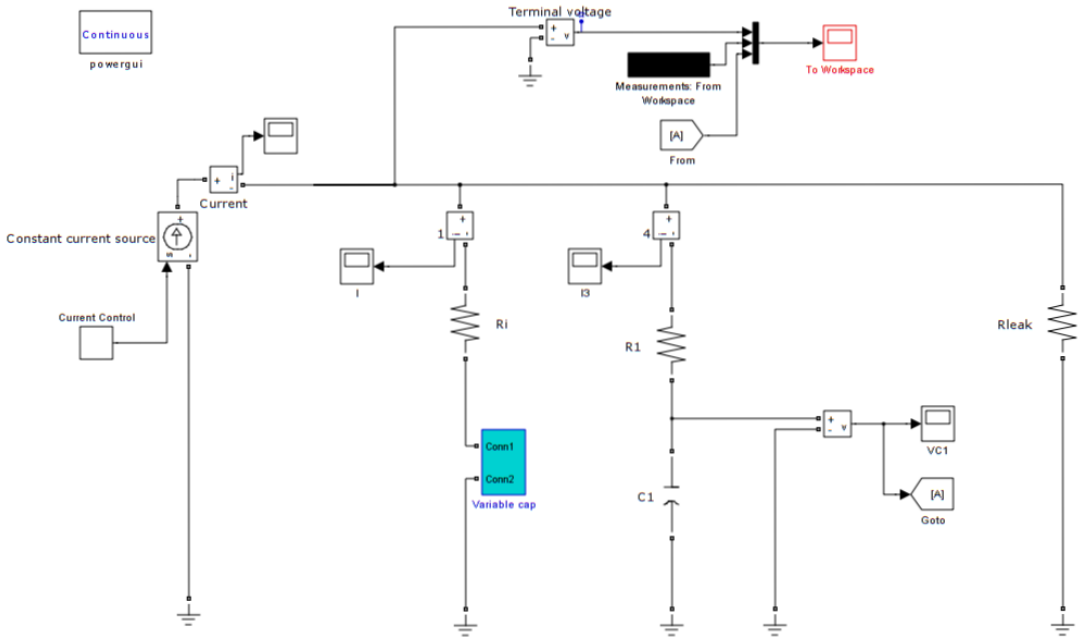

Figure A.11: The Faranda-model formulated in Simpower

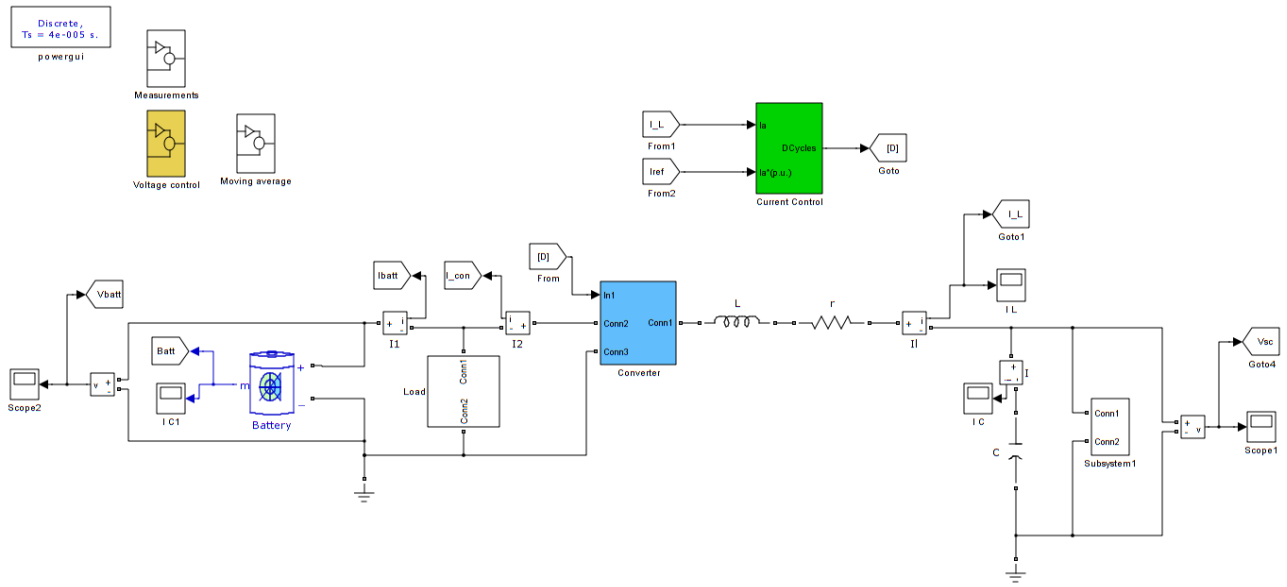

Figure A.12: Semi-active hybrid system model formulated in Simulink with dynamic average repesentation of the converter.

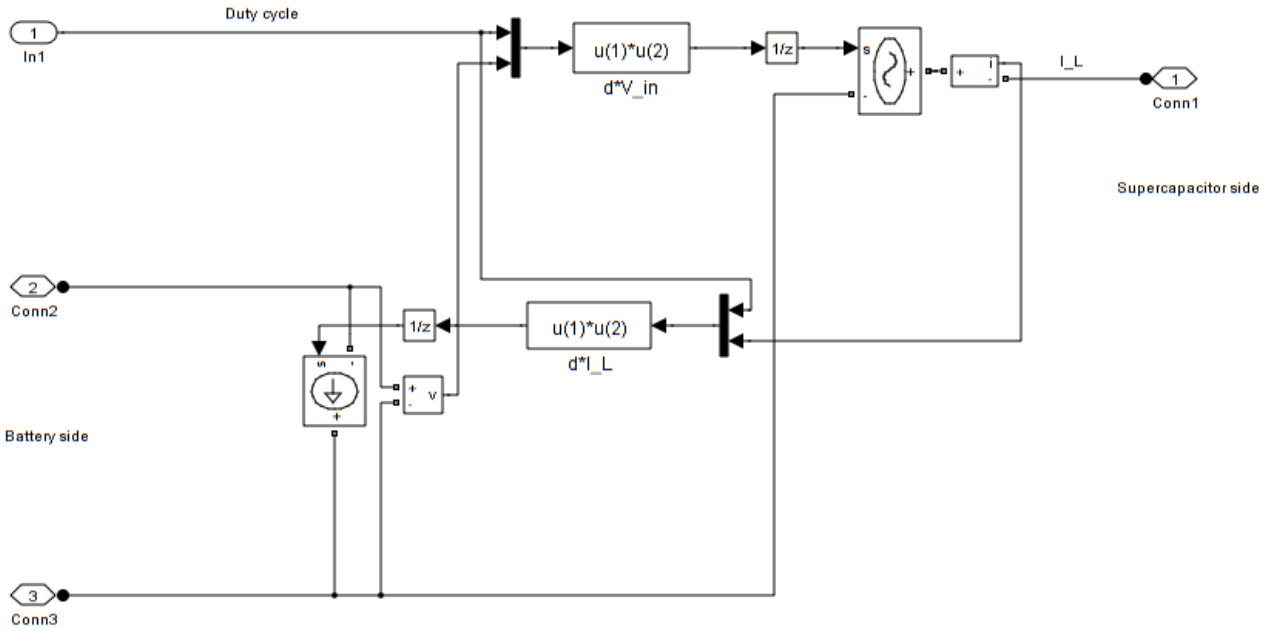

Figure A.13: Dynamic average model formulated in Simulink.

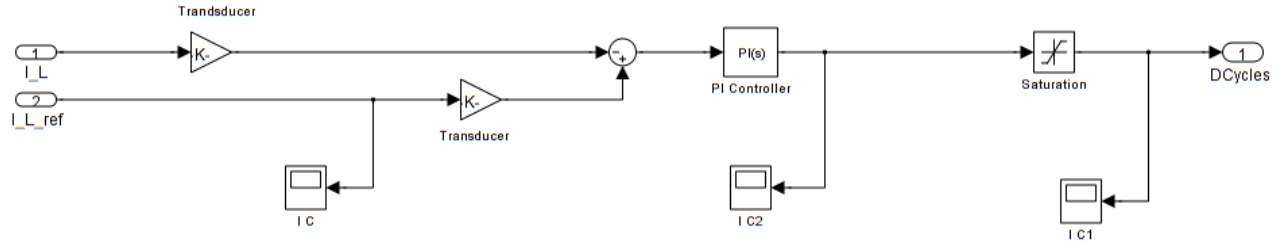

Figure A.14: The PI-controller formulated in Simulink.

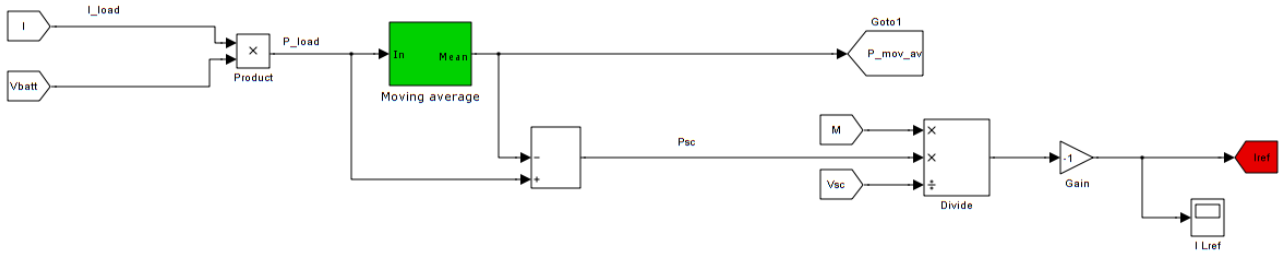

Figure A.15: Current reference generator with moving average in Simulink.

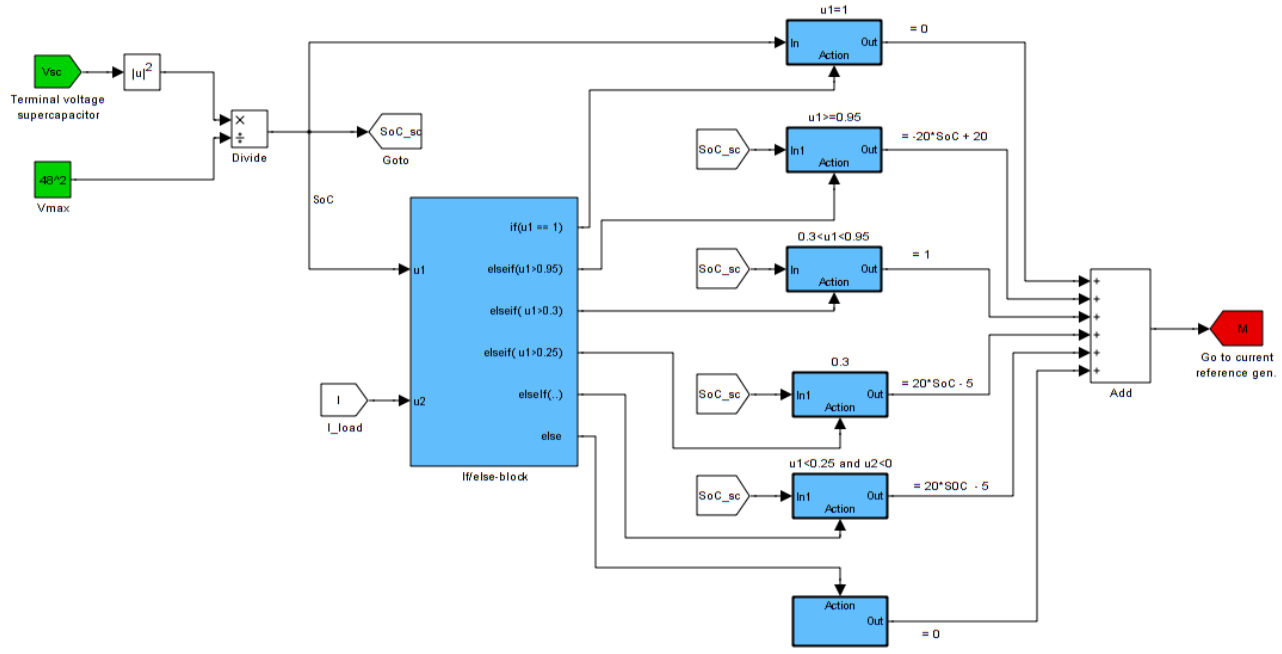

Figure A.16: Voltage protection control block formalized in Simulink.

References

[1] S. Tesfahunegn et. al., "Optimal shifting of photovoltaic and load fluctuations from fuel cell and electrolyzer to lead acid battery in a photovoltaic/hydrogen standalone power system for improved performance and life time," *J. Power Sources*, 2011.

[2] S. Gebre T. et.al., "Optimal load sharing strategy in a hybrid power system based on pv/fuel cell/battery/supercapacitor," IEEE Conferences, 2009.

[3] "Product guide, Bootscap Ultracapacitors," Tech. Rep. Doc.No.1014627.1, Maxwell Technologies, 2009.

[4] H. Herzog et.al., *Lecture notes in Ringvorlesung Energiespeichertechnik.* TU Munich, Spring 2010.

[5] G. Prophet, "Supercaps for supercaches," *Design Feature*, vol. 91, January 9 2003.

[6] S. Pay, "Effectiveness of battery-supercapacitor combination in electric vehicles," IEEE PowerTech Conference, June 2003.

[7] M. Hadartz and M. Julander, "Battery-supercapacitor energy storage," master of science thesis in electrical engineering, Chalmers University of Technology, Gothenburg, Sweden,, 2008.

[8] D. Linden and T. Reddy, *Handbook of batteries.* McGraw-Hill, 3 ed., 2002.

[9] A. Kuperman et.al., "Battery-ultracapacitor hybrids for pulsed current loads: A review," *J. Power Sources*, vol. 162, pp. 981–992, 2011.

[10] J. Schiffer et.al., "Model prediction for ranking lead-acid batteries according to expected lifetime in renewable energy systems and autonomous power-supply systems," *J. Power Sources*, vol. 168, pp. 66–78, 2007.

[11] M. Glavin et. al., "Ultracapacitor/battery hybrid for solar energy storage," IEEE/UPEC Conference, 2007.

[12] S. Atcitty, "Electrochemical capacitor characterization for electric utility applications," phd dissertation, Virginia Polytechnic Institute and State University, Virgina, U.S.A., 2006.

[13] M. Harper and J. Ellenbogen, *Supercapacitors: A Brief Overview.* Mitre Nanosystems Group, Mclean, Virgina, 2006.

[14] Y. Diab, P. Venet, H. Gualous, and G. Rojat, "Self-discharge characterization and modeling of electrochemical capacitor used for power electronics applications," *IEEE*, vol. 24, pp. 510–517, 2009.

[15] P. Tipler and G. Mosca, *Physics for Scientists and Engineers.* W. H. Freeman, 6 ed., 2007.

[16] I. Frackowiak et.al, "Carbon materials for the electrochemical storage of energy in capacitors," *J. Carbon*, vol. 39, pp. 937–950, 2001.

[17] H. Yang and Y. Zhang, "Self-discharge analysis and characterization of supercapacitor for environmentally powered wireless sensor network applications," *J. Power Sources*, vol. 196, pp. 8866–8873, 2011.

[18] F. Rafik et.al, "Frequency, thermal and voltage supercapacitor characterization and modeling," *J. Science Direct*, vol. 165, pp. 928–934, 2007.

[19] N. Bertrand, J. Sabatier, O. Briat, and J.-M. Vinassa, "Embedded fractional nonlinear supercapacitor model and its parametric estimation method," *IEEE*, vol. 57, pp. 3991–4000, 2010.

[20] "Datasheet, Bootscap Ultracapacitors," Tech. Rep. Doc.No 1009364 Rev.3, Maxwell Technologies, 2009.

[21] L. Zubieta and R. Bonert, "Characterization of double-layer capacitors for power electronics applications," IEEE Conferences, 1998.

[22] R. Faranda, M. Gallina, and D. Son, "A new simplified model of double-layer capacitors," *IEEE Conference ICCEP*, pp. 706–710, 2007.

[23] B. Ricketts and C. Ton-That, "Self-discharge of carbon-based supercapacitors with organic electrolyte," *J. Power Sources*, vol. 89, pp. 64–69, 2000.

[24] M. Kaus, J. Kowal, and D. Sauer, "Modeling the effects of charge redistribution during self-discharge of supercapacitors," *J. Power Sources*, vol. 55, pp. 7516–7523, 2010.

[25] Y. Yao, D. Zhang, and D. Xu, "A study of supercapacitor parameters and characteristics," IEEE Conferences, 2006.

[26] "Product information sheet for BCAP and BMOD," Tech. Rep. Doc.No 1009364 Rev.3, Maxwell Technologies, 2009.

[27] J. Larminie, "Current interrupt teqniques for circuit modelling," IEEE Conferences, 1994.

[28] P. Johansson and A. Andersson, "Comparison of simulation programs for supercapacitor modelling," master's thesis in electrical engineering, Chalmers University of Technology, Gothenburg, Sweden,, 2008.

[29] "User Manual Boostcap 56 V UPS Energy Storage Modules," Tech. Rep. Doc.No. 1017025, Maxwell Technologies, 2010.

[30] "Datasheet 56 V Module BMOD0130," Tech. Rep. Doc.No. 1017119.1, Maxwell Technologies, 2011.

[31] R. Dougal et.al., "Power and life extension of battery-ultracapacitor hybrids," *IEEE*, vol. 25, pp. 120 – 131, 2002.

[32] G. Sikha et.al., "A mathematical model for a lithium-ion battery/electrochemical capacitor hybrid system," *J. The Electrochemical Society*, vol. 152, pp. A1682 – A1693, 2005.

[33] G. Sikha et. al., "Performance optimization of a battery-capacitor hybrid system," *J. Power Sources*, vol. 134, pp. 130–138, 2004.

[34] T. Wildi, *Electrical Machines, Drives, and Power Systems.* Pearson Education, 6 ed., 2006.

[35] N. Mohan, T. Undeland, and W. Robbins, *Power Electronics: Converters, Applications and Design.* John Wiley Sons, Inc, 3 ed., 2003.

[36] N. Mohan, *Power Electronics and Drives.* MNPERE Minneapolis, 2003.

[37] *Lecture Notes in 2.004 Dynamics and Control II.* Massachusetts's Institute of Technology, Fall 2007.

[38] N. Nise, *Control Systems Engineering.* John Wiley and Sons, Inc., 6 ed., 2006.